Netherlands Centre for Coastal Research

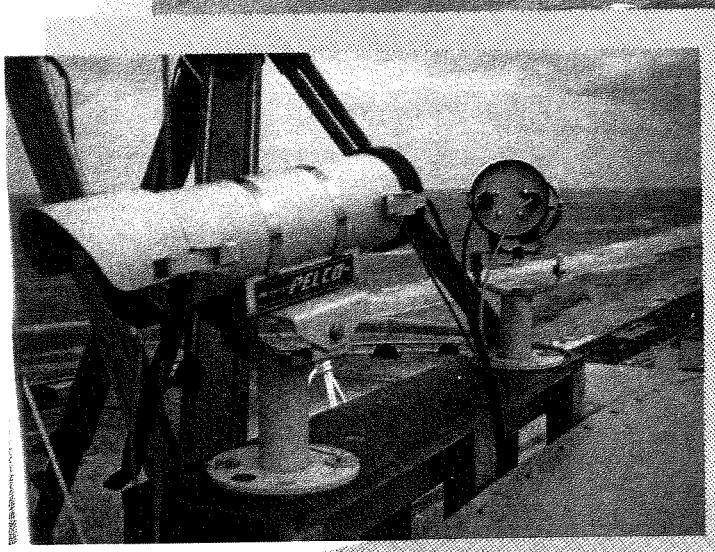

Quantification of bar bathymetry from video observations

S.G.J. Aarninkhof

H 2443

delft hydraulics

May 1996

Quantification of bar bathymetry from video observations

Stefan Aarninkhof
April 1996

M.Sc Thesis

Delft University of Technology
Faculty of Civil Engineering
Hydraulic and Geotechnical Engineering Division

Supervision

Prof.dr.ir M.J.F. Stive
Prof.dr.ir. J.A. Battjes
Dr.ir. J.A. Roelvink

Abstract

Since 1992, coastal morphology and hydrodynamics of the nearshore zone have been studied from video observations, within the framework of the so-called ARGUS research program. Image data are collected every day-light hour, at seven beach locations worldwide. Time-averaged images show bright, longshore bands of intensities, clearly indicating the locations where waves preferably break.

In the nearshore zone waves generally break due to depth limitation. Because of this, locally observed light intensities can be assumed to be related to local bathymetry. This relationship has already been indicated qualitatively by *Lippmann and Holman* [1989].

In this thesis, the relationship between image intensities and bathymetry is quantified. A model called MONIMORPH ('MONItoring MORPHology') has been developed, which estimates the bottom elevation z_b from observed image intensities. This is performed by relating intensity values along a cross-shore transect to a wave parameter, and modelling this wave parameter inversely. For the time being, considerations are one-dimensional and concentrate on the actual region of wave breaking.

From both statistical and physical considerations it was concluded that it might be useful to relate image intensities to the roller energy density E_r divided by the squared phase speed c^2. In order to obtain a quantitative match between intensity profile and E_r/c^2 curve, the raw intensity data are scaled by means of a three parameter model (I_{base}, r, SF). The background intensity parameter I_{base} and the trend removal parameter r are derived from raw image intensities, while the upscaling factor SF is related to the ratio H_{sig}/H_{max} at the seaward boundary of the computational region.

The MONIMORPH wave model comprises the inverted UNIBEST-TC equations, UNIBEST-TC being a cross-shore morphodynamic model developed at DELFT HYDRAULICS. Based on boundary conditions for (H_{rms}, h, θ and η) and a cross-shore distribution of E_r/c^2, it computes the corresponding bottom elevation. Estimates obtained from single images are combined by means of a data assimilation technique. From a sensitivity analysis, a favourable mechanism, damping both initial disturbances in the boundary conditions and noise in the input intensity signal, was found to exist. It makes MONIMORPH suitable to deal with relevant initial deviations of the order of 5%.

The inverse model has been calibrated against data obtained from the field campaign at Duck, October 1994, yielding a scaling relation for SF. Based on this relation MONIMORPH has been tested for 27 different situations. It was concluded that for situations within the range of calibrated wave conditions (the so-called calibration window), reliable estimates of bar bathymetry are produced: deviations at the top of the bar amount 10 to 20 cm, while the mean difference across the bar is 30 to 40 cm. The bar crest is systematically predicted too far shoreward, though the differences of 10 to 20 m are small considering the mild slope of the bar. Situations not matching the wave window have to be excluded from analysis, for the time being.

Application of MONIMORPH to the Noordwijk site confirmed the statement that the model is not yet suitable to be applied outside the range of calibrated wave conditions. Furthermore, it is showed that the scaling parameters are related to a ratio H_{sig}/H_{max} which is depth dependent. Further investigation should provide an answer to the question, whether the Duck scaling parameters can be applied to an arbitrary ARGUS site.

Contents

Contents (continued)

Contents (continued)

1 Introduction

The coastal environment is probably the most dynamic of any ocean domain. The endless sequence of storms and calms causes beach changes that vary from severe erosion with expensive property loss to the accretion of acres of new beach front. With increasing population pressure on the coasts and themes like 'building with nature' being very topical within the field of civil engineering, the development of a fundamental understanding of the dynamic behaviour of the coastal system is imperative.

For the achievement of this objective it is crucial to be able to monitor the dynamics of the coastal system. Previously, much of our present day knowledge has been obtained from field experiments, typically lasting for periods in the order of weeks. Though of great value, all of these field experiments can be characterized as being extremely money consuming, and limited by their finite duration. Second, in the Netherlands, the survey of cross-shore bathymetry is performed once per year, by Rijkswaterstaat. As this sample interval is longer than many of the morphological time scales, characteristics of the shorter-term beach dynamics can not be derived from them. Third, for reasons of safety and accuracy, it is impossible to perform a useful field survey under extreme wave conditions. A new, video based, monitoring technique seems to be able to cope with these fundamental limitations of the conventional methods.

Since 1992 coastal morphology and hydrodynamics in the nearshore zone are studied from video observations. This optical technique has been developed at the Coastal Imaging Lab, Oregon State University (USA) under the guidance of professor R.A. Holman. Nowadays so-called ARGUS cameras are installed at seven beach locations worldwide, amongst which at Noordwijk, The Netherlands. Image data are collected every hour, hence developing an extensive dataset, at relatively low costs.

Time averaged images show bright, longshore bands of intensities, clearly indicating the locations where waves preferably break. As the process of wave breaking is related to local water depths (in the nearshore zone at least), the observed intensity bands are expected to be related to local bathymetry. This relationship has already been noticed qualitatively by *Lippmann and Holman* [1989].

The aim of the present study is to develop a model that quantifies the relationship between observed image intensities and underlying beach topography. In order to do this, three sub-objectives can be specified:

1. To identify a physical parameter, associated to the process of wave breaking, that correlates well with the observed image intensities;
2. To model the physical parameter inversely, such that the bottom elevation z_b can be derived;
3. To calibrate and verify the developed model based on field data comprising surveyed bathymetries.

As this study concerns a first effort to quantify bathymetry from video observations, some restrictions have been taken into account:

- Considerations are restricted to the one-dimensional, cross-shore case;
- Considerations concentrate on those regions of the beach profile, where the process of wave breaking actually takes place. Hence, only estimates of bar bathymetry are pursued;
- To model physical processes over the bar bathymetry an existing wave decay model was adopted. The model has been applied with standard settings. No calibration of the model parameters has been performed within the scope of this study.

The lay-out of the report is as follows. First, the basic techniques necessary to develop the inverse model are treated: photogrammetry, data-collection in the field and wave decay modelling in the surfzone. Chapter 2 discusses the ARGUS way of video imaging, as well as the methods to derive cross-shore intensity profiles from the images. Chapter 3 treats the results obtained from field experiments at Noordwijk and Duck respectively, while Chapter 4 gives an overview of models describing the dissipation of random waves on a arbitrarily shaped beach profile.

Next, the development of the inverse model is treated. Chapter 5 deals with the choice of the intensity related wave parameter, while in Chapter 6 the set up of an inverse model is discussed. This model is called 'MONIMORPH', which stands for 'MONItoring MORPHology'.

In the following chapters, the application of MONIMORPH is presented for two different ARGUS sites. In Chapter 7, the calibration and verification of the model in case of Duck is described. Afterwards, in Chapter 8, a first attempt to apply the hence calibrated model to another site (viz. Noordwijk) is reported. Finally, conclusions and recommendations are given in Chapter 9.

2 ARGUS related video image processing

Much of the present day knowledge of beach morphodynamics has been obtained from relatively few, comprehensive field experiments. Though their results have been of great value, all of these campaigns can be characterized by a finite duration and a severe load on the available research budget. Recent monitoring techniques, based on video observations of the nearshore zone, seem to be able to cope with these fundamental limitations of the conventional field experiments.

One of the best developed systems is "ARGUS", named after the Argus of Greek mythology who was a giant with hundred eyes, ordered by Hera to watch Io. The system has been developed under the guidance of professor R.A. Holman of the Coastal Imaging Lab, Oregon State University. This ARGUS system is the subject of the first section, as well as the adjoining research programme. Afterwards, in Section 2.2, photogrammetric aspects related to working with ARGUS images are treated. Chapter 2 ends with the application of these aspects to the Noordwijk ARGUS site.

2.1 Introduction to ARGUS video imaging

2.1.1 The ARGUS programme

Since 1987 video image processing has been applied in order to study hydro- and morphodynamics of the nearshore zone. The first generation of techniques was 'hand driven' and data were stored on video tapes. However, since 1992, cameras have been installed whose data collection has been automized and recorded images are stored on the hard disk of a computer. Together with the introduction of this new technique of data handling, the ARGUS program was started. Nowadays, seven fully autonomous, unmanned ARGUS stations are present at selected beach locations all around the world. They read in chronological order:

Agata beach, north of Newport, OR, on the Pacific coast (1992)
Duck, NC, on the Outer Banks of North Carolina (1993)
Southern Lake Erie, Ohio, on the south bank of Lake Erie (1993)
La Jolla Shores Beach, San Diego, CA, at Scripps Institution (1994)
Waimea Bay, Hawaii, on the north shore of Oahu (1995)
Noordwijk, The Netherlands, on the North Sea (1995)
Palm Beach, Australia, north of Sydney (1996)

The key part of an ARGUS station is one or more video cameras viewing obliquely along a beach. The camera is connected to an image processing system contained in a small personal computer. Every (daylight) hour data are gathered, comprising one snap shot image (i.e. a 'normal' picture) and one time exposure image, which is an averaged image of 600 snap shots, recorded every second during a period of 10 minutes. This time scale of 10 minutes is chosen such that it averages sufficiently over the directionally and frequency spread wave field, while at the same time, steady wave conditions can be assumed. During the night, when phone rates are low, the data are downloaded to Oregon where they are added to the central ARGUS database at the server of the Coastal Imaging Lab. Support data from close-by tide gages and wave-measuring instruments are also incorporated into the

database. Data are accessible to anyone interested, via the World Wide Web (site http://cil-www.oce.orst.edu:8080) or by ftp'ing to the central server (ftp ruby.oce.orst.edu).

Within the Netherlands, participants to the ARGUS program are the Utrecht University, Delft University of Technology, the Institute for Coastal and Marine Management and DELFT HYDRAULICS. 'Local father' of the video system at Noordwijk is dr. Aart Kroon, Department of Physical Geography, Utrecht University. Noordwijk data are stored on a computer at the Utrecht University, where they are processed from Oregon. The processed data are transferred to the central server at the Coastal Imaging Lab, Oregon State University. In the nearby future it is intended to add wave and tidal data, measured at the offshore platform 'Meetpost Noordwijk', as well as bathymetry data (JARKUS surveys) to the Dutch data base.

2.1.2 What information can be derived from ARGUS images and how can it be processed?

ARGUS images are applied to serve several goals of research interest, some of which are mentioned below. However, as this report is dedicated to the quantification of bar bathymetry from video observed wave breaking phenomena, descriptions in this section will concentrate on these processes. In this respect, this section can be considered as an introduction to the remaining chapters of this report.

A commonly observed phenomenon in the nearshore zone is the process of wave breaking, i.e. the deformation of waves due to decreasing water depth (in the nearshore area, at least). Depending on the ratio between bottom slope and deep water wave steepness two different types of breaking - in case of a relatively mild bottom slope - are distinguished, viz. 'spilling' and 'plunging'. Figure 2.1, obtained from *Van Rijn* [1994], visualizes these two types.

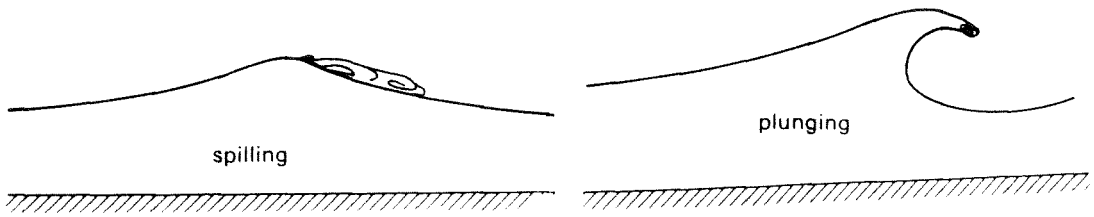

Figure 2.1 Wave breaking types

Spilling breaking occurs in case of relatively steep waves and/or a relatively flat bed. The water surface near the crest spills as the wave crest sharpens with the decrease in water depth. Spilling breaking is accompanied with the generation of a foamy roller at the wave front while the wave trough is not visibly disturbed. The second type, plunging breaking, occurs when the wave steepness is smaller or the bed slope steeper (though still quite mild). A curling jet is generated plunging in the wave trough ahead (causing air entrainment into the fluid body) accompanied by large turbulence production and a forward marching bore after breaking. The generated turbulent motion (so called 'eddies') expands at the backside of the wave crest, where the entrained air bubbles rise to the surface. Both types of breaking are quite common at the Noordwijk beach.

The crucial part of this description is the statement that both types of breaking can be observed at the water surface by means of relatively bright water (due to air bubbles) with regard to surrounding dark water in absence of wave breaking. As wave breaking (in the nearshore zone) is related to the ratio between local water depth and wave height, the observed brightness of the water surface is related to bathymetry.

At this point the considerations of the preceding paragraphs can be linked to the ARGUS video images. Because of the randomness of wind-generated waves, the occurrence of breaking at a fixed location is itself a random process. A snapshot image shows a dark sea with randomly distributed 'white spots' across the surfzone. However, the time exposure images cover a time span of several wave groups. Hence, regions with on the average the highest wave breaking action can be distinguished, which results in 'brightness intensity patterns' at the time exposure images. Remembering that wave breaking is related to decreasing water depth, it may be stated that the bright white bands seen on time exposure images like Figure 2.2, act as an indication of the underlying sand bar topography, although the relationship is quantitatively unknown.

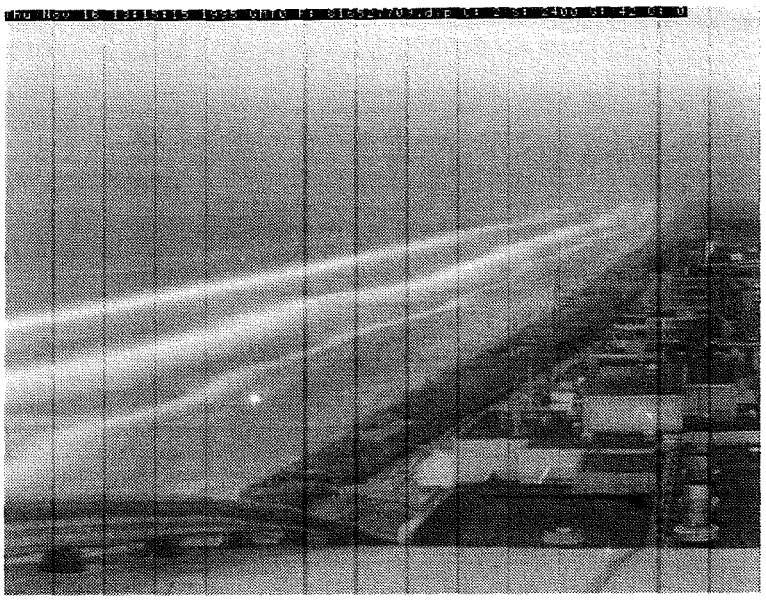

Figure 2.2 Oblique time exposure image Noordwijk, November 16, 1995, GMT 13:00

In order to establish a relationship between observed intensities and bathymetry (which is the subject of this report), four operations are necessary. Notice that this classification, in fact, is valid for any study based on video imaging:

1. Establish a relationship between screen (or image) coordinates (U,V) and field coordinates (x,y,z), and derive the information from those pixels one is actually interested in. In case of the present study, this information concerns the variation of pixel intensities along a cross-shore transect. This operation is described in Chapter 2.
2. Relate the obtained pixel intensities to a physical parameter, associated to the processes that are seen in the images. In Chapter 5 several wave breaking related properties are compared to pixel intensities while the actual relationship is treated in Section 6.1.

3. Transform the indirectly measured parameter in such a way that the desired output is obtained. In case of the quantification of bathymetry, an inverse model has been developed, which is described in Chapter 6.
4. Relate the model output results to field measurements of the parameter concerned, thus having a base to judge the quality of the indirect model. The chapters 7 and 8 describe this process for the present study.

Apart from the quantification of a static bathymetry from video observations, ARGUS images are applied in order to serve several other goals of research. Comparing different images shows a remarkable variation of the white bands, from which information with regard to the dynamical behaviour of the (multiple) bar system can be derived. Especially the opportunity to study long term changes, not limited by any finite period of survey, is attractive, as well as the opportunity to study extreme wave events. Mechanisms initiating the growing of an offshore bar or the transformation of a coastal system from one beach state into the other can be studied in this way. Another application concerns the extraction of beach contours. By investigating wave energy dissipation around the waterline from a time exposure image and relating this to a known tidal level, a momentary sample of the longshore beach bathymetry can be obtained. Doing so during a whole tidal cycle yields the possibility to compose a contour map of the beach. Finally, in regions of non breaking waves, the bathymetry can be estimated by following the position of the wave crest on successive snap shot images. Based on a thus (indirectly) measured phase speed the local water depth can be determined.

2.2 Photogrammetry

The successful use of video image processing for any study requires the understanding of three component problems (*Holman et all.*, [1993]), in increasing order of difficulty:

1. temporal aspects of video sampling;
2. spatial aspects and the transformation between image and real-world coordinates;
3. the relationship between image data and geophysical signals of interest.

The third problem will be the main subject of this report: relating the observed intensity profiles to theoretical dissipation curves and hence deducing the bottom topography. This section will deal with some aspects related to the second problem.

2.2.1 Transforming image coordinates to ground coordinates

The location of any object in the image is a function of the spatial orientation of the camera in relation to ground topography. However, when transforming image coordinates to ground coordinates, the equations are not fully defined, as ground coordinates are 3-dimensional, while image coordinates are 2-dimensional. This is overcome by adding some information to the problem, assuming one dimension to be known. For nearshore related problems it is reasonable to assume the vertical coordinate to be at sea level.

The process of deriving field coordinates from image coordinates is called 'rectification'. Before being analyzed physically every oblique image produced by the cameras at the Noordwijk beach has to be rectified, at least partly. The rectification consists of a large number of geometrical calculations, depending on the number of image points or 'pixels'.

The theoretical background (see *Lippmann/Holman* [1989]) will be explained using the following conventions:

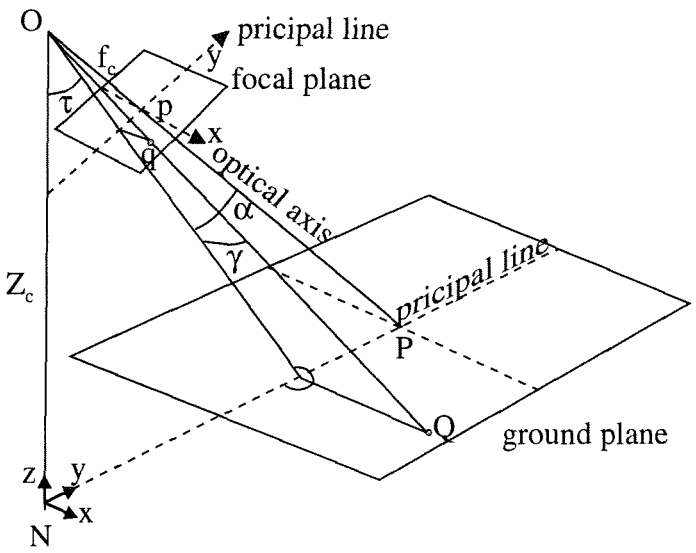

Figure 2.3 Geometrical conventions ARGUS photogrammetry

Image coordinates will be denoted with small letters (x,y); ground coordinates with capital letters (X,Y). The image points lie in the focal plane, separated from camera position O by the focal length f_c which depends on the type of camera lens. The angle τ between the optic axis and the vertical line through O is the camera tilt, and the nadir point N acts as the origin for the ground coordinate system. If necessary, the ground coordinate system can be transformed to a 'more natural', commonly used beach coordinate system with a longshore and a cross-shore axis.

In the oblique images recorded by the video cameras the image coordinates of all objects are known as defined by the pixel positions. Having assumed a vertical coordinate for the ground plane (i.e. having defined the distance Z_c) the ground coordinates can be derived directly from the image coordinates using the following relations:

$$X_Q = \frac{Z_C}{\cos(\tau+\alpha)}\tan(\gamma)$$
$$Y_Q = Z_C \tan(\tau+\alpha) \qquad (2.1)$$

The angles α and γ, which determine the actual position in the ground plane with regard to the optic axis, are defined as

$$\alpha = \arctan\left(\frac{y_q}{f_c}\right), \quad \gamma = \arctan\left(\frac{x_q}{\sqrt{y_q^2+f_c^2}}\right) \qquad (2.2)$$

where f_c denotes the focal length and q is a point in the focal plane, see Figure 2.3. Based on these relations the ground coordinates of all picture elements ('pixels') can be calculated, however, some complications arise while applying these expressions in case of field experiments.

First, the camera tilt τ and the focal length f_c cannot be determined exactly. Field measurements of tilt may be awkward and inaccurate and the focal length of a zoom lens may be hard to estimate. The last problem, f_c being unknown, is solved by counting pixels from the screen and relate them to the field of view of the camera. The expression for f_c reads (see Figure 2.3)

$$f_c = \frac{x_e}{\tan(\delta/2)} \tag{2.3}$$

in which x_e represents the measured distance from the principal point (Point p in Figure 1) to the right-hand edge of the image and δ the field of view of the camera. Unfortunately the field of view δ is another feature which cannot be measured accurately in the field.

Second, the direction of aim of the cameras up on the roof of Hotel Huis ter Duin is chosen in such a way to give the best view of the nearshore zone. As a result of that, the camera related ground coordinate system does not match the 'natural', beach related coordinate system. In particular the angle of rotation ϕ between these two coordinate systems, as well as the camera roll θ relative to the horizon, are hard to estimate in the field, hence further complicating the use of the equations (2.1) till (2.3). In summary, the application of photogrammetry in the field requires the accurate knowledge of four camera related parameters δ, τ, ϕ and θ which cannot, unfortunately, be measured accurately in the field.

The additional unknowns δ, τ, ϕ and θ can be determined quite accurately by making use of clearly defined objects within the field of view of the camera, whose locations are known in the oblique image as well as on the ground. These are the so-called Ground Control Points (GCP's). Each GCP yields two (inverse) relations, viz. the transformation of the x- and y-ground coordinate to image coordinates. So, to solve for four parameters δ, τ, ϕ and θ one needs two GCP's, thus yielding a unique solution. If three or more GCP's are used, the problem is overdetermined and the solution can be optimized by applying a least squares solution. According to Lippmann and Holman [1989] the use of this technique results into typical errors in the estimates of τ, ϕ and f_c less than 0.25°, 0.5° and 0.5%, values which satisfactorily compare to the errors of the order of 1° when measuring these properties in the field.

The process of establishing the relationship between screen and field coordinates is called the "determination of the geometry" or "doing the geometry". It has to be done for every different camera orientation before any image can be rectified. Once this basic image geometry has been determined, the design of spatial sampling arrays can be made at any subsequent time and can be modified whenever necessary. The fact that all investigations are based on one basic image geometry stresses the importance of a well determined geometry.

2.2.2 Rectification of an oblique image

Once the geometry has been determined ground coordinates can be computed for every screen location (U,V). Doing this an image called 'rectification' is created, i.e. the projection of the original oblique image onto a horizontal plane at a certain z-level. Starting from a known geometry the computations are executed for every single pixel, based on the Walton approach, an approach which works with similar triangles. Application of geometrical rules yields expressions, in which the image coordinates (U,V) are expressed as a function of the ground coordinates (x,y,z):

$$U = \frac{Ax + By + Cz + D}{Ex + Fy + Gz + 1} \quad , \quad V = \frac{Hx + Jy + Kz + L}{Ex + Fy + Gz + 1} \tag{2.4}$$

These expressions contain eleven parameters [A..L] which describe the geometry (capital I is not used for this purpose as within the framework of this study I represents 'intensity'). It would need six GCP's, each serving two relations between image and ground coordinates, to solve this system of eleven equations in eleven unknowns [A..L]. Instead of trying to find six suitable GCP's it is also possible to make use of the parameters δ, τ, ϕ and θ and the camera position (x,y,z). Combined with these seven relations, two GCP's would be enough to obtain eleven equations to solve for the eleven unknowns. If more GCP's are used, a least squares approach is possible to solve this linear system of equations.

Knowing the eleven parameters of the so called Walton vector m = [A..L] the ground coordinates (x,y,z) can be deduced from the inverted equations:

$$\begin{aligned} (EU - A)x + (FU' - B)y + (GU - C)z &= D - U \\ (EV - H)x + (FV - J)y + (GV - K)z &= L - V \\ z &= z_{tide} \end{aligned} \tag{2.5}$$

As stated in Section 2.2.1 the third equation has been added to create a system of three equations in three unknowns; it is quite common to use the tidal level as z-level in nearshore hydraulic problems. The result of the rectification process is a plan view image, 'ready for physical analysis'. An example of a rectified image is shown in Figure 2.4, where the numbers along the axis indicate local ARGUS coordinates, so the dry beach is located at the upper side of the image:

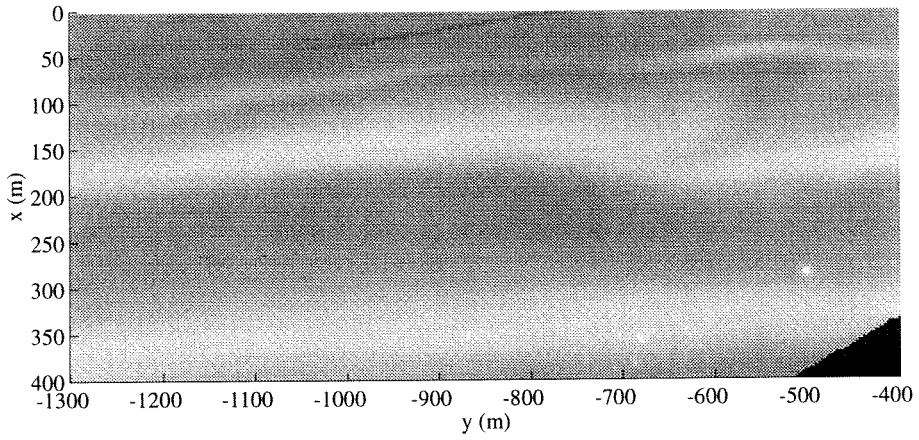

Figure 2.4 Rectified time exposure image Noordwijk, November 16, 1995, GMT 13:00

2.3 Video imaging at the Noordwijk ARGUS site

For each of the two cameras upon the roof of Grand Hotel Huis ter Duin a geometry has to be determined, however, as the camera pointing northward is the only one used for this study the method applied to obtain the 'northward' geometry will be explained in this section.

2.3.1 Determination of geometries for the Noordwijk site

As stated above, "doing the geometry" means the calculation of the parameters δ, τ, ϕ and θ using the locations of two (or more) GCP's. In order to support this process professor R.A. Holman, Oregon State University, Corvallis, developed some MATLAB routines, containing the relations mentioned in the paragraphs before. Running these requires the availability of MATLAB's Image Processing Toolbox, software that supports numeric computation and visualization. The input consists of a clear image of which the geometry is to be determined, a camera file containing the (x,y,z) coordinates of the camera location and two distortion parameters (Section 2.3.3) and a file containing the ground plane coordinates of a number of GCP's. During the Noordwijk field experiments of May 1995, organized by Department of Physical Geography, Utrecht University, the location of several more or less clearly visible objects within the field of view of the camera was surveyed. This field campaign will be treated in Chapter 3 and the results of the survey of (potential) GCP's are given in Table 3.1, however, they are applied here already.

Not all of the surveyed objects were well suited to be used as GCP. Detailed investigation of a carefully selected image, the time exposure image dd. July 24, 1995, GMT 8:00 hr, showed that the GCP's number 7, 2, 9, 8 and 6 could be identified in the picture. The five GCP's are mentioned with decreasing facility of detecting them. During nighttime the only objects that could be traced were the GCP's number 2 and 7. Based upon a selection from these 5 GCP's the following geometries have been determined.

Geometry Nr.	Applied GCP's	Day/Night
1	2,7	night
2	2,7	day
3	2,8	day
4	2,6,7	day
5	2,6,9	day
6	2,6,7,9	day

Table 2.1 Overview of generated geometries, Noordwijk

The MATLAB routine offered the possibility to judge a determined geometry in a qualitative sense, by comparing the computed locations of the unused GCP's to their measured locations and the calculated horizon to the horizon at the image. Since comparing the geometries in a quantitative sense was not really possible, it proved to be difficult to select the best attempt. A certain criterion had to be developed and this will be described in the next section.

2.3.2 Selection of the best geometry for the Noordwijk site

In the previous section six different geometries have been determined, while making uses of different GCP's. The selection of the best one has been performed by comparing the plan view images resulting after rectification. Criterion is the shape and position of a cross-shore intensity profile one can obtain from such an image. The intensity of a pixel has a value

between zero and one, zero indicating 'black' and one 'white'. An example of an intensity profile at transect y = -1000 m is given below.

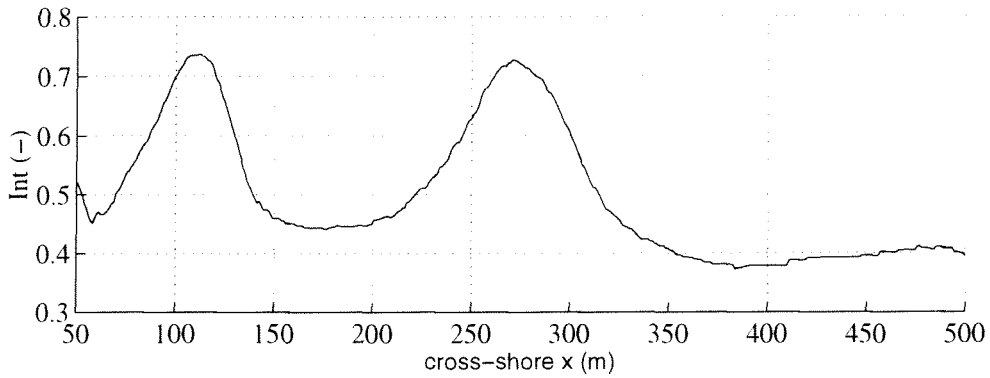

Figure 2.5 Intensity profile Noordwijk, y = -1000 m dd. November 16, 1995, GMT 13:00 hr

Generally, Noordwijk intensity profiles are double peaked, indicating the presence of (at least) two sand bars. A way to characterize these profiles is by reporting the maximum value I_m and associated position x_m of each of the two peaks. As every different geometry yields a (slightly) different rectified image, the resulting intensity profiles will differ slightly, and so will the four parameters ($I_{m,1}$, $x_{m,1}$, $I_{m,2}$ and $x_{m,2}$). Disposing six different geometries, six sets of parameters ($I_{m,i}$, $x_{m,i}$) ha have been generated. While comparing them to each other, immediately, the geometries 1 and 5 turned out to produce results very different from the other four, so they were judged as unreliable and cancelled from further analysis.

In order to select the best geometry it is assumed that all of the four remaining geometries are quite good: they all describe a situation close to, theoretically spoken, the correct solution. Accepting this assumption, then the best geometry would be the 'mean situation' of these four geometries. So by relating each of these four geometries to this mean situation we can select the one which is most close to this mean situation. In practice, for both peaks, the mean maximum value as well as the mean position have been calculated, based on four geometries. Next the values per geometry are related to the mean situation and the absolute differences are summed. The geometry yielding the smallest summed difference in both position and maximum intensity value is judged as being the best (number 6 in the present case), as this one represents the best approximation of the mean situation.

Next step is the question whether this solution is very 'sensitive' for redetermination of the geometry using the same GCP's. In order to check this the geometry has been redetermined four times and the resulting intensity profiles were compared in the same way as described above. The summed absolute differences turned out to be sufficiently small; the best geometry with a position difference of 1 pixel and a maximum value difference of 0.01 (both summed over 4 maxima!) has been selected to serve as definition of geometry for the continuation of this study.

Although the method described above works fine for selecting the best geometry one can think of different ways of doing this, which might be less time consuming at least. As 'doing the geometry' in fact implies the determination of values for the unknown δ, τ, ϕ and θ, one could for instance also compare the results per geometry to a mean value (for each angle). However, for the final result (i.e. the best geometry) this final statement is of minor importance.

2.3.3 Considerations with regard to image quantification and pixel resolution

For image quantification an image processing system is used which breaks the oblique image into a 640 x 480 array of pixels. Pixels are ordered according to a (U,V) pixel coordinate system, which has its origin in the upper left corner of the screen. Normal image resolution is the single pixel, where the location of a circular target is defined according to the nearest pixel. This resolution can be improved by using sub-pixel techniques, which means that the location of a target is determined from centre of mass considerations: U- and V-coordinate of the target are defined as the mean values of the U- respectively V-coordinates of the pixels inside the target. Comparing these improved coordinates to those obtained with normal image resolution yields an indication of the error within the digitized image. The observed differences are a function of the distance of a pixel to the centre of the screen. As such the image is said to be radially distorted. In order to correct for this, image coordinates are 'undistorted' first before being transformed into 'real world' coordinates. Again, a MATLAB routine written by professor Holman is used to do this.

Every pixel of a digitized image represents a small part $\Delta\delta$ of the overall camera field of view δ, which is approximately 30°. So following the method of breaking up images implies a fundamental limit on resolution. The basic spatial resolution or pixel resolution, i.e. the dimensions of the 'footprint' in ground coordinates resulting from one picture element, can be estimated from some simple geometrical computations. Essential is the angular field of view per pixel $\Delta\delta$, which is approximately 30°/640 = 0.047°/pixel for the Noordwijk site. From this value the dimensions of the 'footprint' can be approximated by

$$\Delta x \approx R \cdot \Delta\delta \quad , \quad \Delta y \approx \frac{R \cdot \Delta\delta}{\cos(\tau + \alpha)} \tag{2.6}$$

where R is the straight distance from ground location to camera. So, the pixel resolution strongly depends on the position on the screen (or, equivalent, on the position of an object in the ground plane). Around transect y = -1000 m, which is of interest for this study, R is of the order 1200 m and hence pixel resolutions in x- and y-direction are $\Delta x \sim 1$ m/pixel and $\Delta y \sim 19$ m/pixel.

Another way of obtaining an impression of pixel resolution is by following a numerical path. Once the geometry is known pixel coordinates can be computed for every location in the ground plane and vice versa, ground coordinates can be computed from screen coordinates after having assumed a 'rectification level'. Knowing this one can start from a location within the ground plane, compute its screen coordinates, move half a pixel in both positive and negative x- and y-direction and recompute the ground plane coordinates of the new 'moved' points. The latter two represent the corners of the 'footprint' of the original pixel on the ground plane. After a correction for the camera orientation the dimensions of this footprint in x- and y- direction can be calculated. The numerical estimation of pixel resolution yields results, which are very similar to the simplified estimates above. In Figure 2.6 iso resolution lines are plotted for the stretch of beach between y = -1500 and y = -500 m, up to 400 m. offshore.

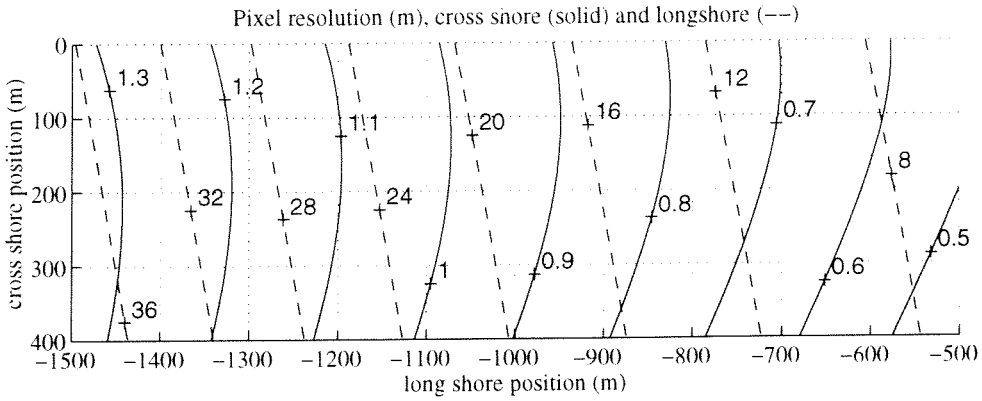

Figure 2.6 Pixel resolutions in x and y direction

The spatially varying pixel resolution plays a role when determining the sample interval for extracting intensity values from the oblique image: when choosing a cross-shore sample interval smaller than the pixel resolution in x-direction one can be sure to extract the maximum amount of information possible from the (smoothened) oblique image.

3 Data collection in the field

Developing a model based on video image data implies that field data are needed in order to calibrate the model and to validate its reliability. Within the framework of this study datasets originating from two different ARGUS sites have been used, namely Duck [1994] and Noordwijk [1995]. They will be described below. As the collection of field data in Noordwijk partly served an educational purpose, the Noordwijk field campaign will be described first, in more detail.

3.1 The Noordwijk'95 field experiments

An important part of the obligatory curriculum at the Faculty of Physical Geography, Utrecht University, is the student's participation to a field campaign once per year, during the first three years of their study. Those students who have decided to specialize within the field of beach morphodynamics fulfil their third year's practical works at the beach. Their task roughly consists of a literature study concerning a physical phenomenon around the shoreline or in the surfzone, the formulation of a research plan including a description of the desired properties to be measured, the actual field activities and the evaluation of the chosen phenomenon based on the collected data.

Because of the installation of two ARGUS cameras in March 1995 on the roof of Grand Hotel 'Huis ter Duin' the Noordwijk beach has been selected to act as research site for the 1995 field campaign. Primarily this campaign has been organized for educational reasons, as described above. However, apart from this, investigations related to the set up of the ARGUS system needed to be carried out and data, necessary for the calibration of the model this report deals with, had to be collected. The latter two subgoals will be treated in this chapter.

In order to do so, the considerations start with a description of the Noordwijk site and its general, physical characteristics. Afterwards the (intended) set of data to be collected will be mentioned, as well as the results, that are relevant with respect to this study. An overview of the equipment that has been used and its estimated accuracy is given in Appendix B, 'Measurement techniques of the Noordwijk'95 field experiments'.

3.1.1 The Noordwijk site

Noordwijk is situated along the coast of central Holland, approximately 25 kilometres from IJmuiden and 20 kilometres from Scheveningen. This Central Dutch Coast is a sandy, inlet-free, wave dominated coast (*Wijnberg* [1995]) which orientation is essentially NNE-SSW: around Noordwijk the shoreline orientation is approximately 28° relative to the north, positive angles counting clockwise. Appendix A shows a map of the Central Dutch Coast.

Along the coast a series of beach poles are present with an alongshore spacing of usually 250 meters, the so called Rijks Strandpalen Lijn or RSP reference line. The beach poles' number indicates its distance relative to Den Helder. The horizontal coordinates of all beach poles, within the axis system that covers all of the Netherlands (the so-called RD-coordinates), are accurately known, so the beach poles can serve as reference points while investigating the beach. The vertical coordinates of the nail, that is placed into the wooden pole, are accurately known relative to N.A.P., the Dutch ordnance level.

Morphology

The bathymetry of the Central Dutch Coast typically comprises 1 to 4 breaker bars, spacing 200 to 240 meters (southward of IJmuiden) and with an orientation obliquely to the shoreline at a small angle. The bathymetry is surveyed once per year by Rijkswaterstaat by echosounding cross-shore transects with a length of approximately 800 m and a spacing of 250 m. In this way the JARKUS database has been developed. The figure below gives a recent bathymetry (June 1995) at transect 81.00 km, showing a multiple bar system with a relatively steep inner bar at 300 m offshore and a second bar around 600 m offshore:

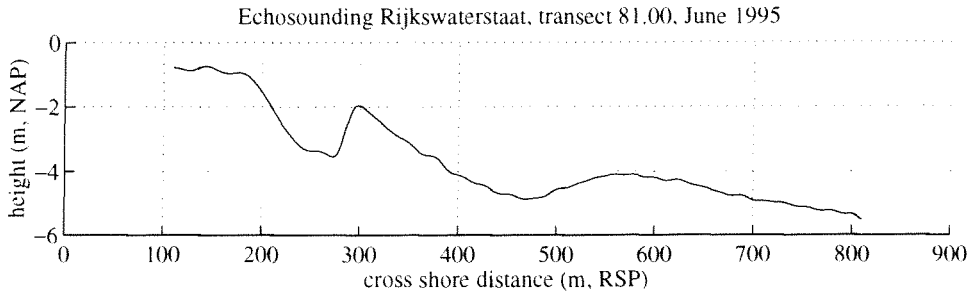

Figure 3.1 Bathymetry Noordwijk transect 81.00 km, June 1995, RWS

Wave climate

With regard to the wave climate distinction should be made between wind waves and swell. The wind waves are generated by local wind fields, hence they are strongly related to the wind climate. H_{sig} and T_{sig} (as well as wind speed and direction) are measured every 10 minutes at platform Meetpost Noordwijk, situated 6 km offshore at 18 m water depth. Wave direction and the spreading of the wave direction are measured at a location 25 km offshore of IJmuiden. Both stations are indicated at the map of Appendix A. Local times are expressed in Middle European Times, which can be transformed into Greenwich Mean Time by subtracting 1 hour. These measurements show average monthly mean wave heights of about 0.8 m during the calm summer months and up to 1.3 m during the winter months. It should be noted that because of the relatively short fetch due to the proximity of the land, these values might be somewhat larger for the fraction of waves incident from seaward direction.

The presence of swell (low frequency waves) mainly depends on the geometry of the Northsea basin, being nearly closed in the south and wide open to the Atlantic Ocean in the north. For this reason swell generated in the Atlantic Ocean or in the northern part of the Northsea will always reach the Dutch coast from northerly directions, although at Noordwijk the direction is more westerly orientated, probably due to refraction.

Tides

Near Noordwijk the mean tidal range is about 1.65 m. The tidal curve is asymmetrical, showing a relatively steep peak around H.W. and somewhat 'flattened' periods of L.W. The water levels are measured at Meetpost Noordwijk but as this is an offshore platform, effects due to wind- and wave set-up are not included. In order to correct for this it is also possible to make use of tidal data measured at the coastal stations of IJmuiden and Scheveningen (which have nearly equally shaped tidal curves) and interpolate between them in order to obtain the Noordwijk values.

Coordinate systems at the Noordwijk ARGUS site

As stated above the coordinates of the beach poles are known in so called RD-coordinates. This RD coordinate system has a positive x-axis pointing eastward, a positive y-axis pointing northward and an origin some distance SW of The Netherlands such, that all coordinates have positive values. For the ARGUS project a local coordinate system has been adopted, with an origin located at beach pole 82 (standing at the beach, a hundred meters northward of the Grand Hotel), a southward pointing, longshore y-axis crossing beach pole 81.25 and an x-axis pointing seaward, perpendicular to the y-as. All objects within the field of view of the cameras can be expressed in terms of these local ARGUS coordinates. Furthermore, transformation from the RD-coordinate system to the ARGUS system can easily be executed by means of a combined translation and rotation.

Especially for the field experiments, a third coordinate system has been applied within the region of the beach pole 81 transect. Within this transect two beach poles are present. While working with a water-level it turned out to be of practical use to determine one's position relative to this line. For this reason the BP81 coordinate system was adopted, having an origin at the 'duneside' beach pole of transect 81, an x-axis pointing seaward towards the 'seaside' beach pole of transect 81 and a y-axis, 90° rotated in counterclockwise direction, relative to the x-axis. The latter BP81 coordinate system is only used to express surveyed data. Figure 3.2 gives an overview of the Noordwijk site including the camera location, the beach poles and the applied coordinate systems:

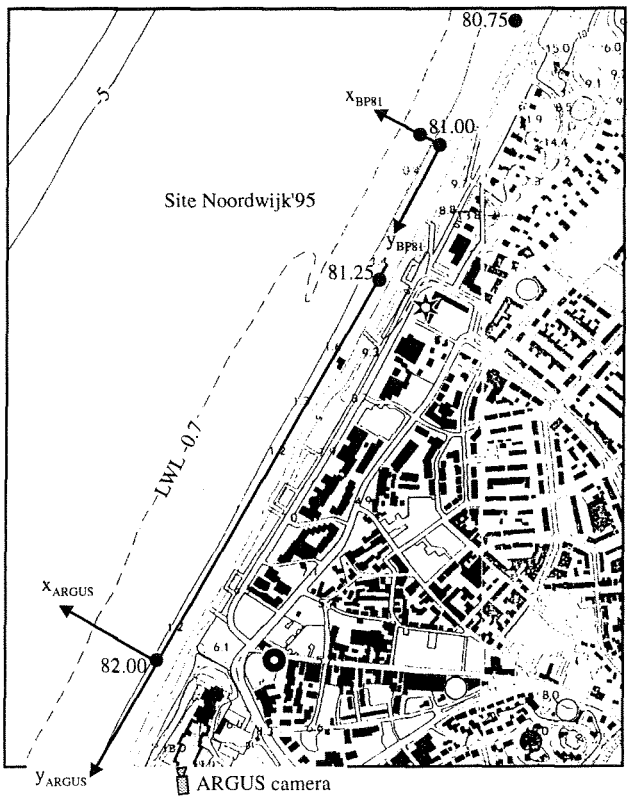

Figure 3.2 Map of Noordwijk beach

Noordwijk ARGUS camera data

The Noordwijk ARGUS cameras are equipped with 12 mm, auto-iris lenses. This implies that the focal length of a lens is 12 mm and that the incoming flux of light energy is kept constant by automatic adjustment of the aperture. The latter can be compared to the functioning of the human eye, of which the pupil is getting smaller in case of brighter light. Maximum and minimum setting of the iris control are determined holding polarizes in front of the camera lens, crossed polarizes indicating 'night' and equal polarizes indicating 'day'. The northward pointing camera, which is of primary interest for the present study, is located at (x,y,z) = (-159.86,160.69,62.23). The x- and y-coordinate are given in terms of the local ARGUS coordinate system, while the height z is defined relative to N.A.P. The camera field of view is approximately 30°.

3.1.2 Preparation: determination of data to be gathered

The Noordwijk field campaign consisted of two separated periods of two and three weeks respectively. The first one (May 8 - 20, 1995) can be seen as a first 'confrontation' with the site, the ARGUS system and the measurement techniques. It was meant as an 'introduction' to the second one (September 18 - October 6, 1995), during which all student participants should try to collect the necessary data for their own research topic. All activities were undertaken in good cooperation, but, from this point on, only the information, relevant to the subject of this report, will be treated.

One of the important goals of the spring field period was the gathering of data to get the ARGUS system operational. Therefore, clearly visible objects within the field of view of the camera had to be surveyed in order act as GCP - see Sections 2.2 and 2.3. Furthermore, the measurements were intended to get an impression of the dynamic behaviour of the beach. For this reason the beach has been surveyed daily using Global Positioning System (GPS) and the morphological activity across the swash bar has been observed.

Based on the experience of the first field period and the state of art of this ARGUS study at the beginning of september, the formulation of the demands for the autumn field period turned out to be possible in better detail. Three considerations proved to be important: In order to develop a model that quantifies bathymetry from observed image intensities it is necessary to simulate the surfzone hydrodynamics with a wave decay model like UNIBEST-TC. Running the latter requires wave data, tidal data and a known bathymetry. Furthermore some difficulties had arisen while trying to interpret the Noordwijk images, e.g. with respect to the determination of the shoreline and the detection of dry bars. Finally, it was decided to make use of the northward looking camera as the other one produced glancing images during part of the day, due to the position of the sun. Knowing this the following demands were formulated:

a. survey of 'wet' bathymetries of at least four different transects, as far offshore as possible given the limitations of the survey method in use. Considering the width of the camera field of view, transects around beach pole 81 were considered suitable;
b. registration of water pressures (thus wave heights) in the trough of the barred profile (preferably at more locations) in order to verify the validity of the results produced by the wave decay model;

c. qualitative description of physical phenomena like rain, fog, brightness and steady foam, which affect the recorded image intensities;
d. determination of the position of the waterline for every surveyed transect (related to the time), as well as a longshore sequence of waterline positions during the registration of a time exposure image.

Of course, the moment of observation (in time) is crucial to all measurements as they have to be linked to the corresponding ARGUS images. An overview of the measurement techniques applied to obtain the desired information, as well as a short discussion on their accuracy is given in Appendix B, 'Measurement techniques of the Noordwijk'95 field experiments'.

3.1.3 Results of relevance with regard to quantification of bathymetry

This section deals with the results obtained during the Noordwijk field experiments 1995. Given the amount of collected data, not all results will be mentioned here: whenever possible a representative part of the results will be given. Furthermore, the results of the spring and autumn period will be treated separately.

Results of the spring period in the field

Central aspect of the first period has been the use of GPS for surveying the beach. With a sample distance of 1 meter the system determines its position with an accuracy of the order of cm. In this way part of the dry beach and the swash bar have been surveyed every day along cross-shore transects spacing 50 meters, starting roughly around beach pole 82 and ending up around beach pole 81.25. The (predictable) time window during which GPS could be applied was limited by instantaneous quality of the satellite configuration and the period of low water, the swash bar being dry only during low water. Furthermore, at least five satellites had to be available (or 'visible'), see Appendix B, Section B.1.

Despite the good accuracy of the GPS-ed surveys these bathymetry data are of no practical value for use into UNIBEST-TC. Reliable modelling of the surfzone hydrodynamics requires the availability of bathymetries that at least extend through this surfzone. The GPS surveyed bathymetries however just cover the dry part of the beach (including the swash bar) at low water. Even at high water, when the process of wave breaking is shifted shoreward due to the larger water depths, the surveyed bathymetries do not extend enough seaward to meet our demands. Instead, they could be used in order to get an impression of the morphological activity of the swash bar, but this is outside the scope of this report.

Moreover, the GPS has been used to determine the position of a number of clearly visible objects within the field of view of the camera, the so-called GCP's - see Chapter 2. As the camera pointing southward is ignored for the time being, just the coordinates of the GCP's to the north of the Grand Hotel are given in terms of the local ARGUS coordinate system:

GCP	Description	X-coord	Y-coord	Z-coord
1	Light Pole 1 (at parking place), base	-88.01	-89.76	6.47
2	Light Pole 1 (at parking place), top	-88.01	-89.76	10.3
3	Light Pole 2 (along boulevard), top	-91.73	-140.50	14.7
4	Light Pole 3 (along boulevard), top	-75.81	-200.25	14.6
5	Telescope on dunes, south	-59.26	-164.56	9.0
6	Telescope on dunes, north	-60.09	-198.16	9.0
7	Lighthouse, light (top)	-110.81	-740.60	36.0
8	Zeereep (road), west corner	-77.43	-832.16	9.79
9	Zeereep (road), east corner	-82.76	-832.14	10.04
10	Beachpole 81.250, top	-0.173	-754.13	2.92
11	Beachpole 81.750, top	-6.614	-253.996	2.52

Table 3.1 Surveyed Ground Control Points, Noordwijk, May 1995

In Chapter 2 the coordinates of four of these Ground Control Points have been used in order to solve the geometry for the Noordwijk site.

Finally, on May 15, the 15 mm camera lenses that had been installed in March have been replaced by 12 mm new ones, in order to widen the field of view of the cameras. Including this last adjustment the Noordwijk ARGUS system has reached its final configuration, as operational presently.

Results of the autumn period in the field

In order to gather information that might help to interpret features on the rectified images, the position of the waterline has been determined together with the corresponding time, while surveying bathymetries by waterlevel. In this way, a data set of (time varying) waterline positions is generated, that can be used in order to detect the waterline from rectified images. Apart from this a number of longshore sequences of waterline positions has been surveyed during the period of recording of a time exposure image, i.e. between hh:00 and hh:10. Two examples of results of the latter are shown in Figure 3.3, where the upper side of the images matches the dry beach and the numbers along the axes correspond to the local ARGUS coordinate system.

The crosses indicate the positions of the beach poles of the transects 80.75, 81.00 and 81.25, while the dashed lines represent the surveyed waterlines. The plotted lines might slightly deviate from the image waterlines due to positioning errors during survey and due to wave related phenomena like swash and surfbeat. Some interesting features can be seen on these images. The relatively dark spot around x = 100 m, y = -1150 m at the first image is the swash bar, that has emerged due to the low tidal level: L.W. was expected at GMT 8:56 hr. Second, the 'cloudy' white spot around x = 130 m, y = -700 m in the October 4 image is caused by a bathymetry related rip current. Due to locally larger water depths some waves can propagate 'through' the swash bar and finally dissipate at the shoreline, where faint white

regions can be observed. Note that this rip current was not present yet at September 22 and hence, it has developed in the mean time, probably during the stormy conditions of September 27 and 28.

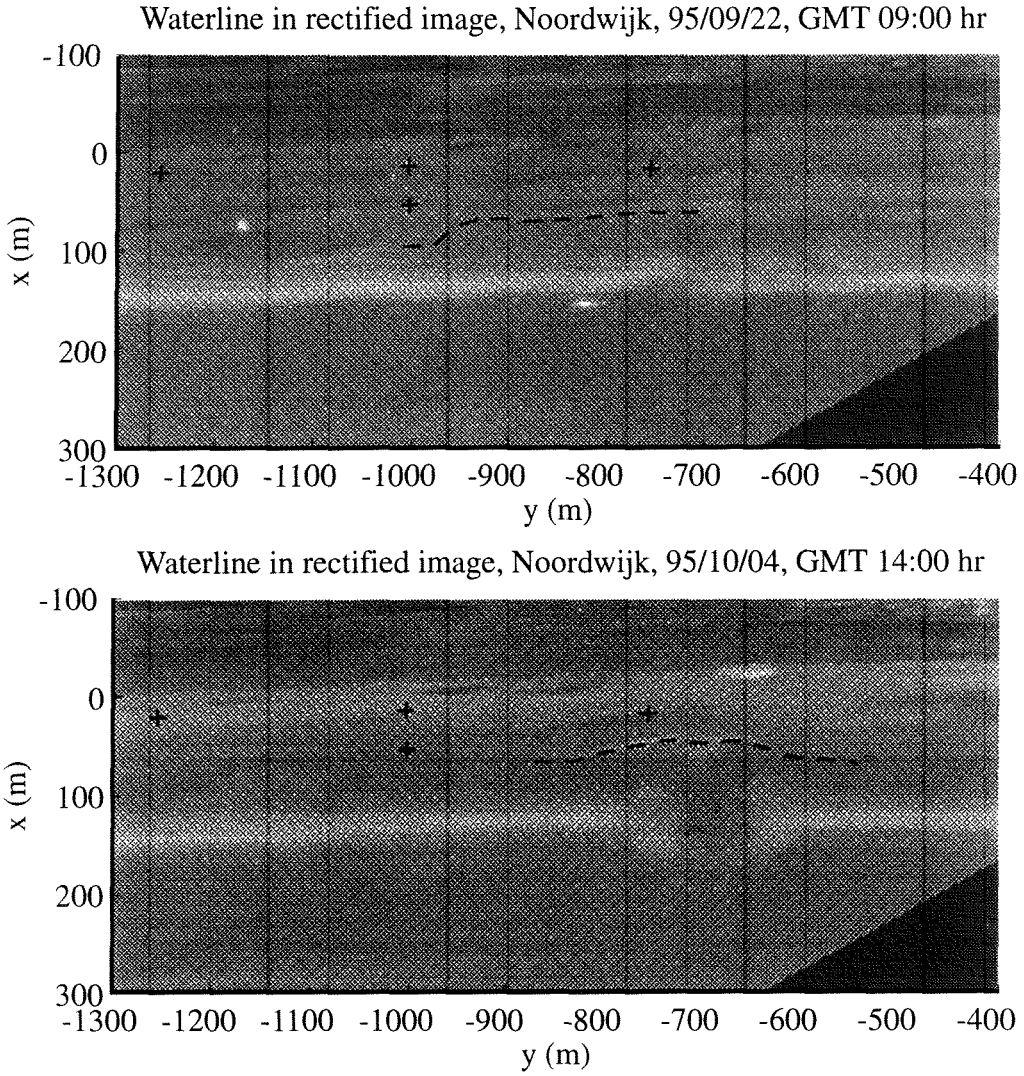

Figure 3.3 Surveyed waterlines during 10 minutes of time exposure

From inspection of the images it can be concluded that the waterline can easily be detected in case of significant wave dissipation at the shoreline. However, these circumstances do not always occur, depending on the wave conditions, the tidal level and the bottom slope. In those cases the distinction between the dark ('breaker-less') near shore water and the slightly brighter dry beach is very weak. It can be concluded that the determination of the waterline position from images, depending on the wave dissipation pattern, might be an awkward task to be executed accurately.

Cross-shore bathymetries have been determined from two different measurement techniques: water levelling and echo sounding. Though better than the May' GPS bathymetries the water levelled beach profiles still contain the disadvantage of being 'too short'. Under extremely calm conditions the distance between the person holding the rod and the water level turned out to be the limiting factor as the top of the rod could not be seen any longer, even with the waterlevel situated at the dry swash bar, while under the more rough conditions the

stability of the person holding the rod in the surfzone turned out to be the limiting factor. Despite the limited profile length visual observations learned that, given extremely mild wave conditions, all of the wave dissipation at high water took place within the region of surveyed bathymetry. The remaining question is whether building a model and calibrating it by just making use of these 'mild' high water data will be a sufficiently reliable method.

The second method, echo sounding the bathymetry from a small vessel, does not contain the disadvantage being unable to reach deep water, however, several other disadvantages arise that are partly related to the method applied at Noordwijk. First of all the ability to apply echo sounding is extremely sensitive to the wave conditions. The sea should be virtually 'waveless' in order to be able to sail the vessel in a safe manner and at the same time make a good echo sounding. Furthermore the horizontal and vertical accuracy of echo sounding is less than water levelling: factors like the wave action (especially when considering the weight of the rubber boat), the method of calibrating the echo sound, the way of determining the position of the boat, etc. strongly affect the accuracy. These aspects are discussed in more detail in Appendix B.

Both methods have been applied during the second period of field experiments in Noordwijk. Water levelling was intended to be done on a daily base for the transects 81.15, 81.05, 80.95 and 80.85 (ordered in increasing distance from the camera), except for September 26 when the rough wave conditions did not allow the execution of the measurement program. Some results are shown in the figures below. During calm conditions the cross-shore profile shape may be quite constant for several days (left hand side). However, other sequences of water levelled profiles show much more variability, which may partly be caused by inaccuracies due to the measuring and positioning technique (right hand side). The maximum depth that could be reached under extremely mild conditions was 2.25 m below N.A.P. The accuracy can be considered of the order 2 cm, in case of measurements at the dry beach, and 20 cm in case of wet profile survey, as explained in Appendix B, Section B.3.

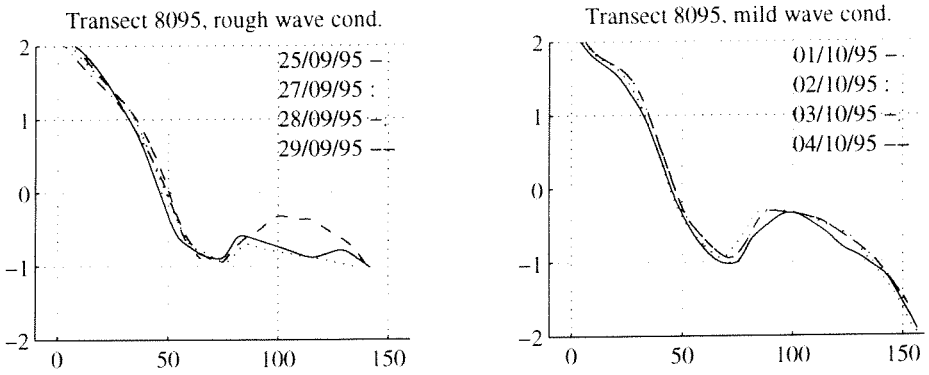

Figure 3.4 Waterleveled bathymetries Noordwijk'95

In order to summarize the results obtained from water levelling, the next table is given. Whenever known the moment of survey is indicated - see paragraph above -and the quality of a waterleveled bathymetry mentioned. The latter, being a highly qualitative indication, is estimated from the maximum seaward distance of a profile and the reliability of individual survey points. All times are expressed as Greenwich Mean Times. Finally, an asterisk (*) marks a time that a longshore sequence of waterline positions is surveyed. Apart from the ones mentioned below, another three 'time exposure waterlines' have been surveyed around transect 81.25.

Date	81.15		81.05		80.95		80.85	
	Time	Qual.	Time	Qual.	Time	Qual.	Time	Qual.
20/09					06:30	+/-	08:00	+
21/09			07:15	-	09:00	+/-	10:15	-
22/09	?	+/-	?	+/-	08:15	+	09:00*	+
23/09	10:35	+/-	09:45	+/-	10:15	+	09:00	+
24/09			10:30	+/-	11:30	+/-	11:40	+/-
25/09	12:20	-	11:45	+/-	10:00*	-	10:30	+/-
27/09	13:00	-	12:20	-	11:00	-	11:20	-
28/09	?	-	?	-	10:30	-	?	-
29/09					11:00	+/-	12:20*	+
30/09	13:45	+/-	14:00	+	13:00	+	13:20	+
01/10	?	+/-	?	+/-	13:30	+	14:15	+
02/10	16:00	+	15:30	+	15:00	+	16:10	+
03/10	?	+	?	+	15:35	+	16:00	+
04/10	16:45	+	16:00	+	?	+/-	?	+/-
05/10	08:30	+	08:00	+	08:00	+	08:30	+

Table 3.2 Overview of waterleveled bathymetries, Noordwijk'95

Unfortunately the echo sounding technique could be applied only once during the second period of field experiments, viz. during the morning hours of October 6. One transect has been surveyed, in casu transect 81.15, in combination with a waterleveled profile at the same time. Due to unfavourable conditions a complex method of positioning had to be applied, which is described in detail in Appendix B. The final results are shown in Figure 3.5. The solid line indicates the 'positioned' profile, obtained from interpolating (x,z) coordinates with 10 m spacing, correcting the profile for moving reference point and fitting the echo sounded profile to the waterleveled one and the Rijkswaterstaat June echo sounding. Additional necessary parameter values are the location coordinates x_A = 156 m, x_B = 206 m, x_C = 110 m and x_D = 400 m, each expressed with respect to the survey coordinate system at beach pole 81. For the meaning of these values, again, reference is made to Appendix B. Transformation values (Δx,Δz) amount (10,-0.30). On the background, a copy of the paper roll is projected, clearly showing the influence of the short wave motion on the vessel.

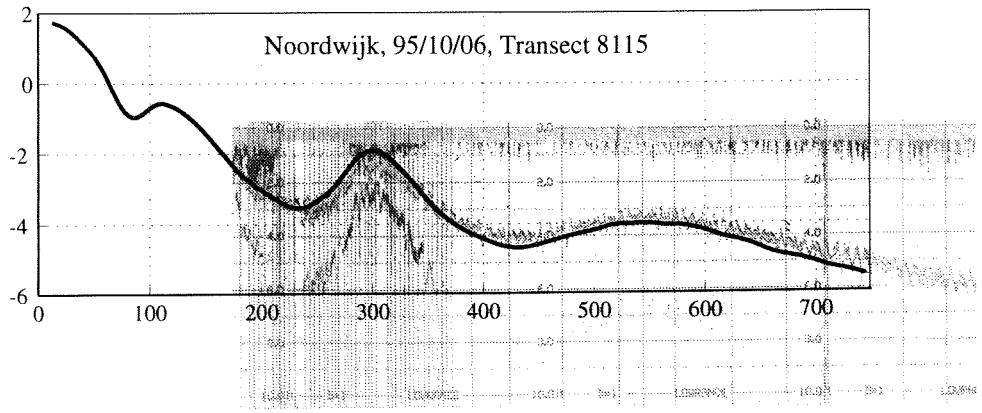

Figure 3.5 Echosounded profile transect 81.15, Noordwijk'95

Because of the positioning problems and the relatively rough wave conditions, the estimated accuracy of this sounding is estimated 0.5 to 1.0 m.

During the 3 weeks of field experiments effectively one frame was present, equipped with an EMF flow velocity meter and a pressure meter to determine wave heights, both during 40 minutes bursts. The measured wave heights are of importance with respect to this study, for calibration purposes. As such only the frame positions in one of the four daily-surveyed transects are of relevance. Investigating the collected frame data yields five surveys that can meet the demands formulated above:

Date	Run	N_{burst}	Transect	x_{RP81} (m)	z_{NAP} (m)	Remarks
23/09/95	306	12	81.15	66.4	-0.68	Runnel
25/09/95	308	11	81.15	64.5	-0.69	Runnel
28/09/95	311	9	81.15	64.8	-0.76	Runnel
03/10/95	315	9	80.95	136.5	-0.93	Seaside inner bar
04/10/95	316	11	80.95	136.5	-0.93	Seaside inner bar

Table 3.3 Overview of useful frame surveys, Noordwijk'95

During every burst wave parameters (H_{sig}, T_{sig}) have been determined representing 40 minutes of survey, who can be used in order to calibrate a numerical wave decay model.

Finally, every day notes have been made regarding the weather conditions and the wave dissipation processes as observed by eye. In this way the effect of these phenomena to the corresponding snapshot and time exposure images can be investigated, which might be useful information while trying to interpret image intensities and developing scaling routines to get from image intensity to breaking parameter in a quantitative sense.

3.2 The Duck'94 field experiments

Because of Duck being the second ARGUS site involved into this study, some information regarding the Duck'94 dataset will be given here. As the author was not involved actively in this field campaign and the geometries had already been determined, the description will be relatively brief.

3.2.1 The Duck ARGUS site

In the past Duck, North Carolina has been the site for several measurements campaigns for different goals of research. It is the site of a government research facility sponsored by the US Army. The location is on the Outer Banks and the relatively steep beaches and frequent storm and hurricane waves make this a dynamic beach environment. The shoreline orientation is approximately 340° relative to the north, positive angles counting clockwise.

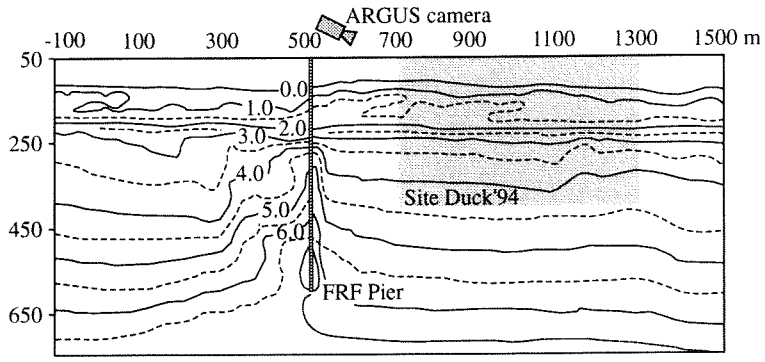

Figure 3.6 Map of Duck site

Since January 1993 an ARGUS camera is present, mounted on a tower about 44 m above sea level. Image data of the camera pointing northward have been used for the set up of the model treated by this report. All data regarding a position are expressed in terms of the local ARGUS coordinate system, which has its origin several hundreds of meters southward of the camera location, an x-axis pointing seaward and a longshore y-axis pointing in northward direction. Local times are expressed as Eastern Mean Times, which are transformed to Greenwich Mean Times by adding four hours. Figure 3.7 gives a characteristic image obtained at the Duck site, showing a white band indicating a longshore bar located approximately 150 m from the shoreline, and a second white band pointing out the shoreline itself. The vehicle that can be seen in the foreground is the so called CRAB, that has been used for the survey of bathymetries - see Section 3.2.2.

Figure 3.7 Oblique image Duck dd. Oct 11, 1994, GMT 16:00

3.2.2 The Duck 1994 experiments

The Duck 1994 experiments have been conducted at the Army Corps of Engineers' Field Research Facility (FRF) in August and October 1994. The beach profile was barred, with a steep slope (approximately 1:10) at the shoreline. During the period in the field average significant wave heights of about 1 m and peak periods of about 7 s have been measured. These wave data were recorded every 3 hours at a station 900 m offshore, in 8 m water depth. The maximum tidal range was 1.6 m, with a mean value of 0.35 m above reference level. Tidal elevations were recorded every 6 minutes by a coastal station.

Like in the case of the Noordwijk campaign, important data to be obtained were bathymetry data. In Duck they are collected at low tide by making use of the so called CRAB. This CRAB is a large steel vehicle, about 10 m in height and capable of moving itself on his wheels. Furthermore, it is equipped with a Global Positioning System. By driving into the sea along transects perpendicular to the shoreline, 'wet' beach profiles have been obtained up to a water depth of about 5 m and with an accuracy of the order of cm. Bathymetries have been surveyed on a daily basis, generally spacing 20-60 m between y = 710 m and y = 1230 m.

Data obtained during the field experiments described above are available for the period October 3 till October 21, 1994, together with the necessary photogrammetric data. Corresponding ARGUS images can be obtained from Internet, or by ftp'ing to the server of the Coastal Imaging Lab, Oregon State University. Both bathymetry, wave and photogrammetric data have been provided by Nathaniel Plant, College of Oceanography, Oregon State University, who was involved in the experiments. Finally, it should be mentioned that at October 13, GMT 19:00, the camera orientation has been adjusted somewhat shoreward, probably because of changing research goals regarding the swash zone.

3.3 Discussion on the suitability of the Duck and Noordwijk data

Besides tidal and wave data, which are available for both Duck and Noordwijk with sufficient accuracy, it is crucial to obtain a set of bathymetries of different days, in order to be able to compare intensity profiles to breaking parameters for different situations. For this reason the Duck'94 data set is preferable as it comprises an extensive set of high quality bathymetries stretching out through the surfzone to deep water. Though Noordwijk bathymetry data are available, they are either too short (water level profiles), or lack reliability (echosounding Noordwijk'95), or determined only once per year (JARKUS data set).

Based on these considerations the Duck'94 data set is selected in order to develop, verify, and calibrate a reverse model that estimates bathymetry from image intensities. Despite the good quality of the bathymetry data it can be questioned whether they are all useful. This can be explained from Figure 3.8, which is a plan view of the Duck image shown in Figure 3.7. The numbers along the axis are coordinate within the local ARGUS coordinate system, so the dry beach is at the upper side of the image. The lines indicate the routes along which the CRAB has moved during survey of bathymetry.

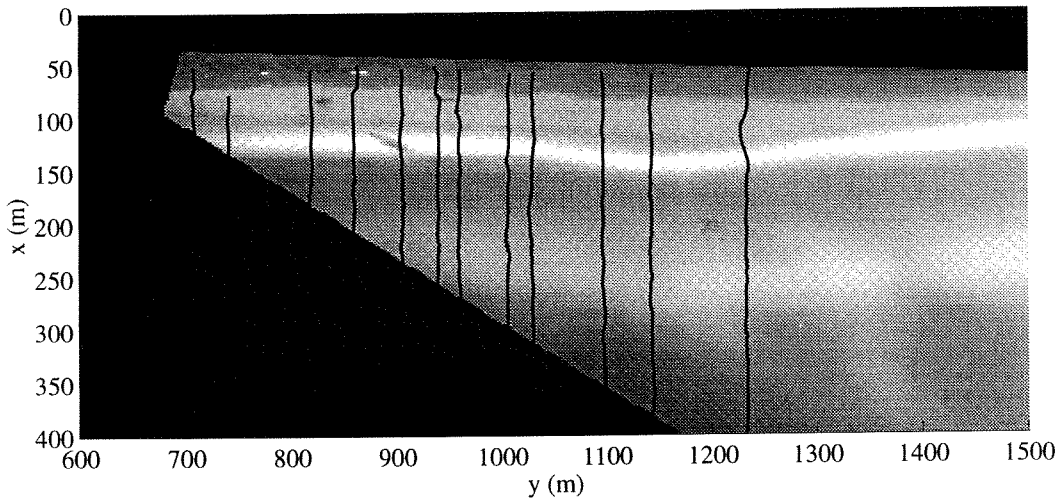

Figure 3.8 Rectified image Duck, October 11, 1994, GMT 16:00

In case of this study we are interested in cross-shore transects along which both intensities as well as bathymetry data are known. Furthermore these transects have to reach to a point outside the surfzone. At the seaward boundary the transects are limited either by the survey length or by the camera field of view. The latter limitation causes some problems in case of the Duck'94 data set. In general it can be stated that the larger the distance between surveyed transect and camera location, the wider the camera field of view. In case of the Duck'94 experiments most of the transects have been surveyed at a relatively short distance from the camera location. This is - within the framework of this study - a disadvantage of the Duck data set, which will become even more apparent after changing the camera orientation, dd. October 13. However, as can be seen from Figure 3.8, transects in the $y > 1000$ m range usually cross the whole surfzone (except maybe, for extremely rough wave conditions) and, as such, they can be used in case of the present study.

Finally, although the Noordwijk'95 bathymetry data might not be that useful, other data certainly will be. Especially when trying to interpret image features or deducing 'scaled' information (see Chapter 6) from the images, the water line surveys and the qualitative observations of atmospheric phenomena will be valuable.

4 Dissipation of random waves on an arbitrarily shaped beach profile

Wave dissipation due to breaking on a gently sloping beach is one of the dominant factors governing the hydro- and morphodynamics of the nearshore zone. It is for this reason that a lot of research effort has been paid to the modelling of breaking of incident random waves due to depth limitation. Early models for random breaking waves, developed during the first half of the seventies, express the local mean wave energy directly in terms of the incident wave parameters and the local depth, without considering energy sources or sinks explicitly. These models are physically not well founded. More recent models are all based on the wave energy balance equation, although they solve it in a different way. Within this group of energy based models *Roelvink* [1993] differentiates three classes of models, viz. the *parametric*, the *probabilistic* and the *dynamic* class of models.

In the first, *parametric* class, a shape of the breaking wave height distribution is assumed, with parameters that are a function of local, time-averaged wave parameters. By combining the energy dissipation per breaking wave (which is modelled analogous to the dissipation in a bore) and the assumed breaking wave height distribution, the average dissipation as a function of local wave parameters is obtained. The latter parameters can be computed over an arbitrarily shaped bathymetry using the wave energy equation, given the conditions at the seaward boundary.

The second, *probabilistic*, class of models equally starts from a known wave height distribution at the seaward boundary, but instead of assuming a wave height distribution which propagates through the surfzone, these models break the wave height distribution at the boundary into a discrete number of wave height classes. Crucial is the assumption that each wave height representing a class behaves like a periodic sub-group that propagates through the surfzone independently of the others. So, the wave energy balance is solved for each wave class separately. By combining the ordered results of the individual computations a breaking wave height distribution can be determined.

The two classes of models mentioned above both assume steady wave conditions. Recently, there has been a growing recognition of the importance of variations in short-wave properties on the time-scale of wave groups, which can be held responsible, for instance, for the generation of surfbeat and edge waves. The *dynamic* class of models takes into account the variations on this time-scale. *Roelvink* [1993] developed a calibrated formulation for the time-varying dissipation of short-wave energy due to breaking, and implemented it into four different wave decay models from either the parametric or the probabilistic group. The slowly varying dissipation rate is expected to have a systematic component which depends on slowly varying characteristics of the short waves, in particular the wave energy. From this, the conditionally expected dissipation rate is formulated as the product of the probability that a wave is breaking, times the expected value of the dissipation rate in a breaking wave, given the energy density E. The latter statement, the dissipation being known given this one specific value of E, is the extension of the class of dynamic models with regard to the other two. In order to compute the average wave dissipation rate a distribution for the energy density E at the seaward boundary has to be assumed, which is split into discrete energy levels which propagate through the surfzone independently (probabilistic model) or which

is multiplied by the dissipation rate given E and integrated over all possible energy levels, which yields the mean dissipation that can be used as input for the parametric models.

The dynamic models are beyond the scope of this study, so they will not be discussed any further here. Instead, attention will be paid to the first two classes, the parametric and the probabilistic models.

4.1 The parametric wave dissipation models

4.1.1 Wave decay model according to Battjes and Janssen [1978]

The first parametric model has been given by *Battjes and Janssen* [1978], here referred to as BJ78. It models the dissipation of energy in random waves breaking on a beach. Instead of assuming a direct relation between water depth and wave height it is based on the energy balance equation, an approach which has a sound physical basis and allows application to profiles where the depth is not monotonically decreasing shoreward, as well as inclusion of other energy sinks or sources. This energy balance equation for waves perpendicularly incident on a prismatic beach in stationary situation, reads

$$\frac{dP_x}{dx} + D = \frac{d(Ec_g)}{dx} + D = 0, \tag{4.1}$$

in which P_x is the x-component of the time-mean energy flux per unit length which can be expressed as the product of the energy density E and the wave group velocity c_g, x is a horizontal coordinate normal to the still-water line and D is the time-mean dissipated power per unit area, which can comprise all dissipative mechanisms affecting the waves. BJ78 present a formulation for the contribution due to wave breaking. The dissipation term in equation (4.1) is modelled as the product of the energy dissipation given a certain breaker height and the occurrence probability of this breaker height. These two aspects are treated separately, starting below with the second one.

Breaking wave height distribution according to BJ78

Reasoning that every depth determines a maximum possible wave height H_m the breaking wave height distribution can be modelled as a clipped Rayleigh distribution, an assumption which is characteristic for the Battjes and Janssen model:

$$\begin{aligned} F(H) \equiv Pr(\underline{H} \le H) &= 1-\exp(-\tfrac{1}{2}H^2/\hat{H}^2) \quad \text{for } 0 \le H < H_m \\ &= 1 \quad \text{for } H_m \le H \end{aligned} \tag{4.2}$$

$\hat{H}$ and H_m are the two parameters of the probability function. The clipped distribution assumes that the waves are Rayleigh distributed up to a maximum wave height H_m, that all higher waves are simply cut off to this height, that all waves having this height H_m are breaking and that only these waves are breaking. The fraction of breaking waves Q_b is assumed to equal the area under the delta function at H_m of the clipped Rayleigh wave height probability density function.

Instead of using $\hat{H}$ and H_m, the root mean square wave height H_{rms} and the fraction of breaking waves Q_b can be defined as the parameters of the probability function:

$$H_{rms} = \left(\int_0^\infty H^2 dF(H) \right)^{1/2} \tag{4.3}$$

$$Q_b = Pr(\underline{H} = H_m) \tag{4.4}$$

Substituting these relations yields Q_b as a function of the local wave height H_{rms} relative to the maximum wave height H_m at that depth, from which Q_b can be solved iteratively:

$$\frac{1 - Q_b}{\ln Q_b} = -\left(\frac{H_{rms}}{H_m} \right)^2 \tag{4.5}$$

For H_m BJ78 applied an adapted Miche-criterion

$$H_m = \frac{0.88}{k} \tanh\left(\frac{\gamma kh}{0.88} \right) \tag{4.6}$$

in which γ is an adjustable coefficient representing the ratio of breaking wave height to local water depth. Finally the wavenumber $k = 2\pi/L$ is the positive real root of the dispersion equation.

Energy dissipation per breaking wave

The second aspect of the dissipation expression is the rate of energy dissipation in a single breaking wave. This is modelled in analogy to the energy dissipation in a bore (*LeMéhauté* [1962]). Following the definition sketch below the dissipation D' in a bore per unit crest length can be written as

$$D' = \frac{1}{4} \rho g d_1 U_1 \frac{(d_2 - d_1)^3}{d_1 d_2} = \frac{1}{4} \rho g (d_2 - d_1)^3 \sqrt{\frac{g(d_1 + d_2)}{2 d_1 d_2}} \tag{4.7}$$

In case of a periodic bore this transforms to

$$D' = \rho g c_{bore} \frac{h(d_2 - d_1)^3}{4 d_1 d_2} \quad \text{with} \quad c_{bore} = \sqrt{\frac{g d_1 d_2 (d_1 + d_2)}{2h^2}} \tag{4.8}$$

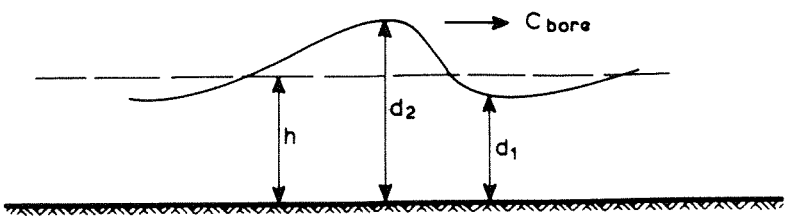

Figure 4.1 Definition sketch of bore

According to *Stive and Dingemans* [1984] at this point, the cases of shallow water and deep water should be considered separately.

a. Shallow water

In shallow water it is reasonable to assume that d_2-$d_1 \cong H$, $d_1 d_2 \cong h^2$ and $c_{bore} \cong c_{wave}$. Applying these relations to expression (4.8) yields

$$D' = \frac{\alpha}{4} \rho g c_{wave} \frac{H^3}{h} \tag{4.9}$$

in which α is a constant of order one if the assumed analogy between a breaking wave and a bore is valid.

For periodic waves the average rate of energy dissipation per unit area is obtained by dividing the dissipation per unit crest length by the wave length L:

$$D = \frac{D'}{L} = \frac{D'f}{c_{wave}} = \frac{\alpha}{4} \rho g f \frac{H^3}{h} \tag{4.10}$$

For shallow water conditions the ratio H/h is of the order 1 and expression (4.10) further reduces to

$$D = \frac{\alpha}{4} \rho g f H^2 \tag{4.11}$$

b. Deep water

In deep water Stive and Dingemans stated that the water depth d_1 in (4.8) should be considered as a penetration depth, denoting the depth of the layer in which the breaking wave characteristics may be compared with a bore. Following this, the simplifications d_2-$d_1 \cong H$, $d_1 d_2 \cong H^2$, $h \cong H$ and $c_{bore} \cong c_{wave}$ can be applied, thus yielding

$$D_{wave} = \frac{\alpha}{4} \rho g f H^2 \tag{4.12}$$

Comparing the equations (4.11) and (4.12) shows that the wave dissipation in both shallow and deep water can be described with the same expression. Furthermore, this is the same expression BJ78 found from their derivation based on shallow water conditions, however, the formulation according to *Stive and Dingemans* [1984] may be more accurate.

For a random wave field the average energy dissipation can be computed from the wave dissipation given a certain wave height (equation (4.11) or (4.12)) combined with the probability that this wave indeed is breaking (equation (4.5)):

$$D = \frac{\alpha}{4} Q_b \bar{f} \rho g H_m^2 \tag{4.13}$$

Thus, equation (4.13) determines the power dissipated in the breaking process as a function of the unknown local wave height H_{rms} (or energy density E), the known local depth (through H_m) and some constants. Starting from a known wave height at the seaward boundary of the computational area the energy distribution throughout the surfzone can be computed by integrating the energy balance (4.1).

Due to the wave breaking process the cross-shore radiation stress component decreases shoreward. To counterbalance this effect the hydrostatic pressures should increase, which explains the increasing mean water level or wave set-up in shoreward direction. The magnitude of the time averaged set-up can be computed from the momentum balance

$$\frac{d\bar{\eta}}{dx} + \frac{1}{\rho g(d+\bar{\eta})}\frac{dS_{xx}}{dx} = 0 \qquad (4.14)$$

in which d is the bottom depth below still water level and the overlined η the time averaged set-up η_{mean}. The radiation stress component S_{xx} in (4.14) is computed according to

$$S_{xx} = \left(0.5 + \frac{2kh}{\sinh 2kh}\right)E \qquad (4.15)$$

Solving the momentum balance (4.14) for η_{mean} requires a boundary condition, which normally implies that η_{mean} is set to zero outside the surfzone. By adding the wave set-up to the bottom depth below still water level the actual water depth is obtained, which should be used when solving the energy balance, although BJ used this momentum balance to provide an independent check on the validity of the model rather than correcting the mean water depth.

4.1.2 Wave decay model according to Thornton and Guza [1983]

A second frequently applied parametric wave decay model has been developed by *Thornton and Guza* [1983], here after referred to as TG83. Apart from adding a dissipation formulation due to bottom friction to the organized wave energy balance, the main difference with regard to BJ78 is the shape of the assumed breaking wave height distribution. BJ78 uses a clipped Rayleigh distribution which is said not to represent measured breaking wave height distributions very well. Although the agreement between measured and computed H_{rms} is reasonably well, it does not mean that the underlying pdf's are similar, which was also noted by Battjes and Janssen.

In order to develop a better breaking wave height distribution, Thornton and Guza carefully studied a number of measured distributions at Torrey Pines Beach, California. Although from literature the Rayleigh wave height distribution was shown to apply to deep water waves on the assumption that the sea waves are a narrow-banded, linear, Gaussian process, the Rayleigh distribution turned out to 'fit well' under a much wider range of conditions, even within the surfzone. From this Thornton and Guza concluded that the distribution of breaking wave heights $p_b(H)$ can be expressed as a weighting of the Rayleigh distribution for all waves:

$$p_b(H) = W(H)p(H) \qquad (4.16)$$

Additional demands are that (a) $p_b(H)$ should resemble the field observations, (b) $p_b(H)$ is a subset of the distribution p(H) for all waves, implying the weighting function $W(H) \leq 1$ and (c) the area under the distribution is equal to the percent of breaking waves, as a result of which $p_b(H)$ is not a pdf. In accordance with rule (c) the fraction Q_b of all waves which are breaking can be expressed by

$$Q_b = \int_0^\infty p_b(H)\, dH \tag{4.17}$$

TG83 proposes two different shapes of the weighting function W(H). The easiest form assumes that the waves break in proportion to the distribution for all waves, thus yielding

$$W(H) = A_b = \left(\frac{H_{rms}}{\gamma h}\right)^n \tag{4.18}$$

where n is a variable to be determined from observations. So, the weighting function is independent of H. The advantage of this expression for W(H) is that it yields analytical solutions for the wave height decay of H_{rms} on a plane beach, however, the reality is not represented that well since the likelihood of a wave breaking in (4.18) is independent of its height. Field observations show that at a particular location the largest waves are more likely to break and hence, the breaking wave height distribution $p_b(H)$ should be skewed to the higher waves relative to the Rayleigh distribution. The second W(H) proposed by TG83 accounts for this effect:

$$W(H) = \left(\frac{H_{rms}}{\gamma h}\right)^n \left[1 - \exp\left(-\left(\frac{H}{\gamma h}\right)^2\right)\right] \leq 1 \tag{4.19}$$

The breaking wave height distribution obtained from applying W(H) according to (4.19) turns out to give a better fit to measured field data, but an analytical solution for H_{rms} based on (4.19) is not possible. From (4.16) in combination to (4.18) or (4.19), the average rate of energy dissipation is calculated by multiplying the dissipation for a single broken wave of height H (again based on the analogy with a bore) by the probability of wave breaking at each height as given by $p_b(H)$

$$D = \frac{B^3}{4} \rho g \frac{\bar{f}}{h} \int_0^\infty H^3 p_b(H)\, dH \tag{4.20}$$

in which B is a breaker coefficient of order 1, which accounts for the differences in various breaker types. For B=1 the breaking process is completely bore-like. In TG83 this integral has been carried out for the two weighting functions mentioned. The dissipation function D obtained from the more realistic weighting function (4.19) reads

$$D = \frac{3\sqrt{\pi}}{16} \rho g B^3 \bar{f} \frac{H_{rms}^5}{\gamma^2 h^3} \left[1 - \frac{1}{(1 + (H_{rms}/\gamma h)^2)^{5/2}}\right] \tag{4.21}$$

When comparing the results obtained from BJ78 and TG83, the predictions for H_{rms} throughout the surfzone are equally correct. TG83 gives a better prediction for Q_b when

using standard values for the free parameters (α,γ) in BJ78. However *Beyer* [1994] shows that BJ78 can also predict Q_b reasonably well when using different values for the model parameters (α,γ) - see paragraph 2.2. Considering furthermore the fact that wave decay sub-model of UNIBEST-TC (*DELFT HYDRAULICS* [1995]) is based on BJ78, the decision is made that the calibration of TG83 will not be discussed within the scope of this study. Instead, all considerations in the subsequent sections concern the wave model BJ78.

4.1.3 Behaviour and calibration of the BJ78 model

The behaviour of the BJ78 model strongly depends on the combined behaviour of Q_b and H_m. At first sight equation (4.13) suggests a maximum dissipation offshore, as H_m decreases shoreward with decreasing depth. However, because of Q_b being virtually zero, the resulting dissipation is also virtually zero. While approaching the shore Q_b increases significantly around a depth less than 2 to 3 times the rms wave height. This increase of Q_b more than compensates the reduction in $(H_m)^2$ thus yielding an increased dissipation. Immediately after a bar the reverse effect takes place, thus yielding a decreased dissipation. Near the limit of very shallow water, Q_b ultimately approaches its maximum value (=unity), in which case the dissipation decreases, ultimately in proportion to $(H_m)^2$. Summarizing, the dissipation predicted by BJ starts at approximately zero offshore, reaches a maximum value somewhere in the surfzone and decreases, ultimately in proportion to $(H_m)^2$ very close to the shoreline. This behaviour matches field observations of nearshore wave breaking.

The degree of accuracy to which BJ78 simulates the wave height decay in the surfzone depends on the choice of the free parameters α and γ, which control the level of energy dissipation in a breaker and the fraction of breaking waves respectively. The sensitivity of the model properties H_{rms} and Q_b to variations in these two parameters has been investigated by *Beyer* [1994]. A decreasing α turned out to increase both H_{rms} and Q_b at every location along the cross-shore profile. With respect to H_{rms}, increasing γ showed a similar behaviour as observed for decreasing α: H_{rms} increased. Finally, changing γ turned out to have a very small influence on the predictions of Q_b, except for one case with a relatively mild bottom slope and low deep water wave steepness, for which Q_b decreased with increasing γ. The latter effect was only found on the seaward side of a bar structure.

An extensive calibration of BJ78 has been made by *Battjes and Stive* [1985]. Data from 20 different cases (laboratory- as well as field data) with different types of profiles (plane, concave, bar and bar-trough) were used to find optimal values for the model parameters α and γ. The calibration has been based on a comparison of H_{rms} values, as water level measurements (necessary for comparing computed and measured wave set-up) were available in only a few of the 20 cases. The model is forced to simulate a certain energy dissipation which depends on both α and γ (equation (4.13)). While doing this the model will be tuned only to a measured wave height which is determined by the amount of dissipation. So, there is a dependence between the two parameters α and γ; they cannot be treated separately. Different, suitable combinations (α, γ) give similar wave heigth decay. Hence, there is effectively only one degree of freedom in tuning the model, despite its two free parameters. In fact, the calibration is carried out by estimating optimal values of γ under the constraint $\alpha = 1$, which matches the assumption earlier made that α should be a coefficient of order 1.

Following the calibration method described above a set of γ-values was obtained, which turned out to depend systematically on the deep water wave steepness s_0. Fitting a hyperbolic tangent function to these data yielded a relation for γ versus s_0:

$$\gamma = 0.5 + 0.4 \cdot \tanh(33 s_0) \tag{4.22}$$

Based on this relation Battjes and Stive evaluated the model performance. A comparison of normalized computed and measured H_{rms} values in the zone of wave shoaling and breaking covering all 20 cases yielded a correlation coefficient of 0.98. Furthermore the rms relative error, i.e. the square root of the summed quadratic errors relative to the measured value at any point divided by the total number of measurements, is 0.06, after normalization with the mean value of all measured values of H_{rms}/H_{rms0}.

Despite the good results obtained in case of predicting the rms wave height the model performance turned out to be less good with respect to water level prediction. The maximum set-up is well predicted, but the predicted interval of steepest rise of the mean water level is systematically too far seaward. This can be explained by introducing a transition zone, observed in the lab (*Svendsen* [1984]) and in the field (*Nairn et al.* [1990]), which is not taken into account in BJ78. An improved modelling of this phenomenon is discussed in Section 4.1.4.

Besides this *Beyer* [1994] points out that the prediction of the fraction of breaking waves Q_b considerably underestimates the measured fraction of breaking waves when using standard values for the calibration parameters (i.e. $\alpha=1$ and γ according to (4.22)). He suggests to improve the prediction of Q_b by applying values for α and γ different from the standard ones. From his sensitivity analysis, described above, he concludes that there exist more combinations of (α,γ) that give similar wave height decay (as already noted by *Battjes and Stive* [1984]), while at the same time giving different fractions of breaking waves. A lower α, combined with an appropriate choice for γ, will give a higher Q_b and a similar wave height decay. The wave height increase resulting from the lower α is compensated by a similar wave height decrease due to a lower γ, thus still yielding a correct wave height prediction. At the same time the fraction of breaking waves increases due to the lower α, while (approximately) not being affected by changing γ, thus giving a better agreement with measured fractions. The optimal value of α seems to depend on the deep water wave steepness: α increases with decreasing wave steepness s_0. The closer α to unity (thus the smaller s_0), the better a breaking wave resembles a bore. For the plane slope cases α also was found to increase linearly with increasing surf similarity parameter ξ_0 (Irribarren), though this conclusion was based on only three cases. The γ-parameter is assumed to depend on the beach slope, though this assumption is very weak again due to the limited number of cases considered.

For seven different laboratory cases Beyer finds combinations (α,γ) of the order (0.4, 0.55) for plane slope profiles and (0.4, 0.60) for non monotonic profiles. All combinations (α,γ) he reports fulfil the relation $\alpha\gamma^5$ = constant which is described by *Dingemans* [1995]. This very simple relationship is derived from an explicit expression for the fraction of breaking waves $Q_b = 2.4*b^7$ with $b = H_{rms}/H_m$ which approximates the theoretical BJ78 expression (4.5) closely within the region of breaking. This explicit expression has been substituted into the dissipation formulation (4.13). Assuming constancy of dissipation and shallow water conditions a small offset in γ was studied, which ultimately yielded the relation between α and γ. Changing α by a factor 2 gives a change in γ of 15%, a result which was also mentioned by Beyer.

Even with these improved model parameters, two main discrepancies between predicted and measured Q_b cannot be solved by any combination (α,γ) in case of barred beach profiles. A lag between the location of the maximum predicted Q_b -at the bar crest- and the maximum measured Q_b -shoreward of the bar crest-, as well as the inability to predict the persistence of wave breaking after the bar are mentioned. In the following some attention will be paid to these two problems.

4.1.4 Modifications to the BJ78 model

From the preceding we can conclude that there are two main discrepancies for which the original model BJ78 has to be improved:

a. The transition from set-down to set-up is consistently predicted in regions too far seaward. This has already been noted by BJ [1978];
b. The maximum value of the fraction of breaking waves is predicted at a location somewhat seaward of the measured location, as pointed out by Beyer [1994].

In order to solve for the first discrepancy the roller formulation has been added to the model, for the second a weighted water depth function has been built in. Both are discussed below. The inability to predict breaker persistence, also mentioned by Beyer, is closely related to the first item.

a. Energy transformation in the surfzone (roller model)

As stated above BJ78 consistently predicts the water level set-up too far seaward. Instead of a water level rise starting immediately after the commence of breaking (as predicted by BJ78) a relatively horizontal mean water level is observed in the field. The steep gradient in the water level due to wave set-up only appears a certain distance shoreward of the starting point of breaking. This region is called the transition zone, which can be defined as the region of nearly horizontal or very weakly sloping water level inside the surfzone before the beginning of a steep gradient in the water level due to wave set-up. The existence of the transition zone can be explained from an energy point of view, as has been done by *Svendsen* [1984].

The water level rise due to wave set-up is a result of gradients in the cross-shore radiation stresses. The latter gradients are caused by dissipation of wave energy. The transition zone features rapid wave height decay without an associated increase in energy dissipation, witnessed by the nearly horizontal water level. Instead of being dissipated immediately after the breakpoint, part of the organized wave energy (or potential energy) is converted into kinetic energy first, which can be seen from the development of a roller at the face of a breaking wave. Such a roller is a turbulent bore-like mass of water representing a forward momentum flux, which is ultimately dissipated through the production of turbulence. In other words, by adding a roller to the wave decay model the dissipation of wave energy is delayed. Based on these considerations the roller model has been developed (*Svendsen* [1984], *Nairn et al.* [1990]).

The roller energy density E_r represents a forward momentum flux (or kinetic energy) per unit area. As the propagation speed of a roller travelling on top of the wave equals the phase velocity, E_r can be written as

$$E_r = \frac{\frac{1}{2}\rho A c^2}{L} = \frac{\rho A c}{2T} \tag{4.23}$$

where A is the roller area, c the phase velocity, T the wave period and L the wavelength - see the definition sketch in Figure 4.2.

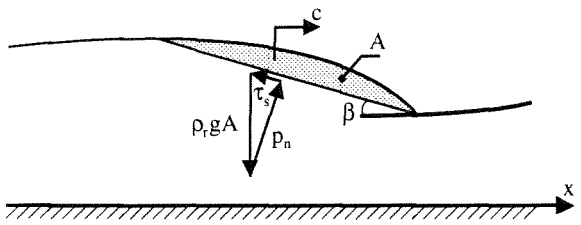

Figure 4.2 Definition sketch of roller

The energy balance of a roller consists of a source term, which is the decrease of organized wave energy as predicted by BJ78, and a sink term, which represents the dissipation of roller energy E_r through the production of turbulence, thus yielding the roller energy balance

$$\frac{d(E_r c)}{dx} = D_{BJ} - D_{roll} \tag{4.24}$$

The system of differential equations (4.1) and (4.24) can be solved by using Svendsen's concept of a roller as a 'block' of water moving at the phase velocity at the sloping face of a breaking wave. When the sink term D_{BJ} of the organized wave energy is assumed to be known as a function of the local wave parameters, the roller energy density E_r becomes the unknown parameter. If the roller dissipation D_{roll} can be modelled as a function of E_r, the roller energy E_r can be solved from (4.24).

According to Nairn et al. the dissipation of kinetic roller energy can be modelled as the work per unit of time, performed by the shear stress τ_r between the roller and the organized wave motion

$$D_{roll} = \overline{\tau}_r c \tag{4.25}$$

This shear stress τ_r counterbalances the gravity force acting on the roller, so the magnitude of the shear stress can be deduced from the balance of forces parallel to the slope of the wave surface, which leads to

$$\overline{\tau}_r L = \beta \rho g A \tag{4.26}$$

where β represents the mean slope under the roller. This coefficient β is assumed to be a constant of order 0.05 - 0.10 (i.e. independent of H_{rms} and x). Combining (4.25), (4.26) and (4.23) indeed yields the dissipation of roller energy as a function of E_r:

$$D_{kin} = \beta \rho g c \frac{A}{L} = 2\beta g \frac{E_r}{c} \tag{4.27}$$

According to *Stive and De Vriend* [1994] this roller dissipation formulation should be changed once more because of an additional roller energy dissipation due to changing roller volume. Besides the energy dissipation due to shear stresses there is another sink, caused by a net transfer of water from the wave to the roller. If the roller is losing water ($dA/dx < 0$) the horizontal momentum transfer from the roller to the wave is not only that due to the shear layer, but also the momentum of the water leaving the roller. This can be considered as an additional (seaward) shear stress as changing momentum per unit time implies a force. If the roller gains water ($dA/dx > 0$), the water leaving the wave has a negligible horizontal velocity which again can be considered as a retarding braking force on the roller as the roller has to accelerate the gained water. In both cases, however, the amount of kinetic energy in the roller changes in proportion to the changed volume, so the additional dissipation for both cases amounts to

$$D_{roll,2} = \tfrac{1}{2}\rho c^2 \left|\frac{dA}{dt}\right| \approx \tfrac{1}{2}\rho c^2 c \left|\frac{\partial A}{\partial x}\right| \tag{4.28}$$

where the partial derivative to time has been ignored because of the assumed steady wave conditions. Dividing expression (4.28) by L results into the dissipation per unit area due to changing roller volume. If the dissipation formulation (4.27) is considered as $D_{roll,1}$ the total dissipation of kinetic energy can be written as

$$D_{roll} = D_{roll,1} + D_{roll,2} = 2\beta g \frac{E_r}{c} + \tfrac{1}{2}\rho f c^2 \frac{\partial A}{\partial x} \tag{4.29}$$

The dissipation of roller energy according to (4.29) can be used in the roller energy balance equation (4.24). However, the balance equation can be simplified by substituting the equations $f = c/L$ and $A = (2 \cdot E_r \cdot L)/(\rho \cdot c^2)$ into expression (4.29). If the spatial variations in c are assumed to be small with regard to the spatial variations in E_r, the term $D_{roll,2}$ reduces to the cross-shore gradient in roller energy flux and the following roller energy balance equation is obtained:

$$\frac{\partial 2E_r c}{\partial x} = \frac{\alpha}{4} Q_b \bar{f} \rho g H_m^2 - 2\beta g \frac{E_r}{c} \tag{4.30}$$

which is the balance equation for roller energy as it is used in UNIBEST-TC.

As the radiation stress is defined as the contribution of the waves to the mean horizontal flux of horizontal momentum, the contribution of a roller to S_{xx} is

$$S_{xx,roller} = \frac{(\rho A c)c}{L} = 2E_r \tag{4.31}$$

and the momentum balance equation including roller energy reads

$$\frac{\partial\left(\tfrac{1}{2} + \frac{2kh}{\sinh 2kh}\right)E}{\partial x} + \frac{\partial 2E_r}{\partial x} + \rho g h \frac{\partial \bar{\eta}}{\partial x} = 0 \tag{4.32}$$

which is the expression UNIBEST-TC applies.

b. Breaking delay due to inertia

In case of rather strong bottom variations BJ78 does not describe the process of wave breaking very accurately as the sub-model which predicts the fraction of breaking waves reacts only to the local water depth and disregards the fact that waves need a distance in the order of a wave length to actually start or stop breaking. Phrased in different words, once the wave has felt the bottom and realizes it has to break, there still remains a time gap till the beginning of the breaking process. *Roelvink et al.* [1995] describe a method to take this feature into account. In the formulation where the breaking wave height H_m (and thus Q_b) is computed, the local water depth has been replaced by a water depth weighted over a certain distance seaward of the computational point. Thus the computation of Q_b based on the bathymetry some distance further offshore results into a shoreward shift of the Q_b-curve, which meets one of the objections *Beyer* [1994] made. A triangular weighting function $W(\xi) = X\,\xi$ has been used, where the integration distance $X = \lambda L_p$ has been taken proportional to the local peak wave length L_p with λ taken constant of order 1. The expression for the weighted water depth h_b reads

$$h_b(x) = \frac{\int_{x-X}^{x} W(x-x')h(x')dx'}{\int_{x-X}^{x} W(x-x')dx'} \qquad (4.33)$$

An example of such a weighted bottom depth $h_b(x)$ is given in the figure below. Significant changes mainly occur in regions of strong bottom variations. Although the physical base for the application of this weighted bottom depth for the computation of Q_b is rather weak, application is justified given the better results produced with the weighted bottom depth (see *Roelvink et al.* [1995]).

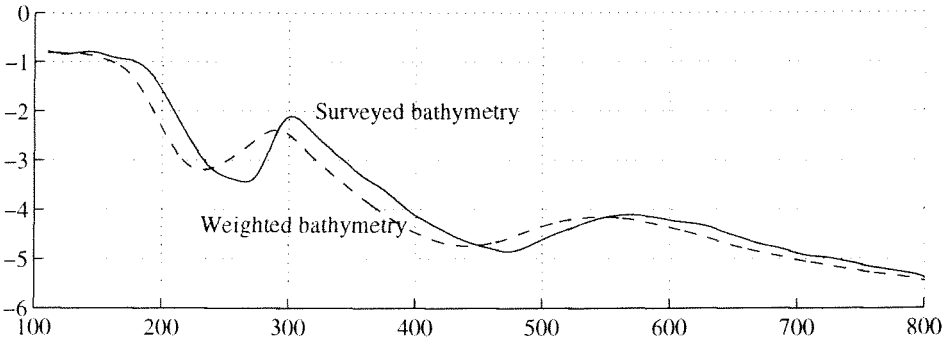

Figure 4.3 Surveyed versus weighted bathymetry, Noordwijk, Transect 81.00, June 1995

4.2 The probabilistic wave dissipation models

In addition to parametric wave dissipation models, probabilistic wave dissipation models have been developed. In literature several reasons are mentioned to justify this, like the fact that the cumulative distribution function of the wave height - in case of a clipped Rayleigh distribution - is discontinuous at the point of the wave height of breaking limit which is not very realistic (*Mase and Iwagaki*, [1982]). Furthermore it is argued that the assumption of a Rayleigh type breaking wave height distribution through the surfzone is not valid. *Mizuguchi*

[1982] blames this to non-linear interactions in the surfzone yielding a changed wave period distribution, while *Dally and Dean* [1986] explain the statement from measured wave height distributions in laboratory and field. An individual wave analysis is proposed in order to meet these criticisms. The probabilistic models developed by *Mizuguchi* [1982] and *Dally and Dean* [1986] will be treated here. The model of *Mase and Iwagaki* [1982] is based on the small amplitude wave theory in case of shoaling, a modified version of the breaker index for monochromatic waves according to Goda and the bore model in case of energy dissipation. However, it is limited to planar beaches and for this reason, it will not be considered any further here.

4.2.1 Wave decay model according to Mizuguchi [1982]

The concept of Mizuguchi is based on the modelling of a so called Primary Individual Wave (PIW). A lot of effort is spent to define such a PIW. In order to do so a method has to be chosen to distinguish between individual waves. The zero-down crossing method is selected because of its capability to define the small secondary waves, which are a characteristic feature of the surfzone. Thus determined surfzone wave height spectra confirm this statement, as the down method yields a double peaked spectrum, contrary to the mono peaked one given by the up method. A second problem is the presence of low frequency fluctuations (arising from standing waves) that affect the zero level for progressive individual waves. The magnitude of these fluctuations is visualized by applying a low-pass filter and comparing the root mean square value of the long period fluctuations to the raw fluctuations: especially near the shoreline, the long period fluctuations become significant. In order to prevent that zero crossings are missed due to these fluctuations, high-pass filtered data will be corrected for this effect by subtracting the long period fluctuations from the measured water surface fluctuation. Finally, a reading error E_R, i.e. a band width of magnitude E_R around the zero level, is introduced into the model. Initially this has been done to remove the error of reading related to the optical measurement technique applied, however, later on it is also adjusted to suppress the effect of the secondary fluctuations. Primary wave peaks exceeding the E_R level are easily identified from observations, which suggests the introduction of 'Primary Individual Waves' (PIW). As all secondary fluctuations are suppressed, a one-to-one correspondence exists between thus defined individual waves and the eminent peaks.

Summarizing, a PIW can be defined by applying the zero-down cross method with a suitable value of E_R to the high-pass filtered water surface fluctuations. This spatially varying, proper value of E_R should be chosen such that the same number of waves is observed throughout the observation area as for the most offshore-ward region: increasing E_R yields higher values of T_{sig} and hence, less waves. The corresponding wave period distributions - like the number of waves - are also seen to be essentially constant and therefore, the wave periods of the PIW can be considered to be constant through the area of concern. So each PIW can be treated as a regular wave. Near the shoreline, where the PIW's themselves become small and can not be distinguished from the secondary fluctuations, the observed number of waves is not constant. In this region the secondary fluctuations are not negligible any more and should be included in the modelling of the wave transformation, affecting as such just the acting wave heights.

The thus defined individual wave (or PIW) is modelled according to a wave-by-wave approach. Outside the surfzone the wave height is assumed to obey the relation (*Shuto* [1974])

$$H^{\frac{5}{2}}\left[\left(\frac{gHT^2}{d^2}\right)^{1/2}-2\sqrt{3}\right] = \text{const.} \tag{4.34}$$

where H is the wave height and d represents the water depth. Inside the surfzone an energy balance equation is assumed to hold:

$$\frac{d(Ec_g)}{dx} = -\epsilon = -\tfrac{1}{2}\rho g \nu_e (kH)^2 \tag{4.35}$$

with

$$\nu_e = \nu_{eb}\left(\frac{H}{\gamma d}-\frac{c}{\gamma}\right)^{1/2} \tag{4.36}$$

In these relations ν_e is the eddy viscosity, k the wave number, ν_{eb} the eddy viscosity at the breaking point, γ the wave height to water depth ratio at the breaking point and c the wave height to water depth ratio in the wave reforming zone. The breaker criterion reads

$$\frac{H_b}{H_0} = s^{0.2}\left(\frac{H_0}{L_0}\right)^{-0.25} \tag{4.37}$$

where s is the slope of the uniform beach and the index 0 indicates deep water values. Due to the form of the viscosity according to relation (4.36), waves are enabled to recover under certain situations.

In this way the wave height transformation of an irregular wave train while crossing the surfzone can be described by considering individual waves, and afterwards, taking the results together. In general, the agreement between calculated and observed PIW's is fair, although decay after breaking is more rapid in the observation than in the calculation. Near the shoreline wave heights are consequently underestimated due to the inapplicability of the concept of PIW near the shoreline, the exclusion of set-up effects and the fact that the wave height in the model is assumed to be zero at the waterline which does not match reality.

4.2.2 Wave decay model according to Dally and Dean [1984, 1986]

Another model describing the transformation of the probability density function of wave heights as random waves cross the nearshore region and surfzone is described by *Dally and Dean* [1986]. It is based on a previous study of the same authors regarding regular breaking waves, dating from 1984. Investigating results obtained from wave decay models based on the concept of a moving hydraulic jump they concluded that none of these models predicted the phenomenon of the wave height stabilizing at some value in a uniform depth following the initiation of breaking. This phenomenon had been seen in laboratory as well as field observations. Dally and Dean have included it by adding a stable energy flux term to the wave energy balance equation:

$$\frac{\partial Ec_g}{\partial x} = -\frac{K}{h'}\left[Ec_g - Ec_{g,stab}\right] \tag{4.38}$$

where K is a dimensionless decay coefficient, h' the still water depth and $E \cdot c_{g,stab}$ the energy flux associated with the stable wave that the breaking wave is striving to attain - see the definition sketch below.

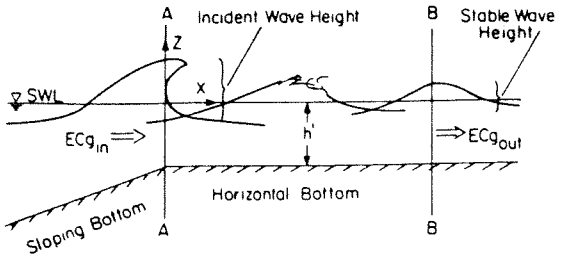

Figure 4.4 Definition sketch wave decay model Dally

From laboratory experiments a stable wave criterion $H_{sig} = \Gamma \cdot h'$ could be deduced and hence, the basic model equation (4.38) can be written as

$$\frac{\partial(H^2\sqrt{h'})}{\partial x} = -\frac{K}{h'}\left[H^2\sqrt{h'} - \Gamma^2 (h')^{\frac{5}{2}}\right] \tag{4.39}$$

where c_g is taken as $(gh')^{1/2}$. For three different cases, viz. a shelf beach, a plane beach and an equilibrium beach profile, equation (4.39) can be solved analytically - results are given in *Dally et all.* [1984]. From wave height measurements in a wave flume it could be seen that, as the still water depth approached zero, the wave height did not. For this reason the water level variations due to wave induced set-up/down have been added to the model by means of the relation

$$\frac{\partial \bar{\eta}}{\partial x} = -\frac{3}{16}\frac{1}{(h' + \bar{\eta})}\frac{\partial H^2}{\partial x} \tag{4.40}$$

Furthermore, though of minor importance, a formulation of the energy dissipation due to bottom friction has been introduced. Due to these modification the possibility to determine analytical solutions vanished, which moreover also holds for the case of more realistic beach profile shapes. Hence a numerical solution technique had to be developed in order to solve the energy balance equation - again reference is made to *Dally et all.* [1984]. Required boundary conditions include H and h at a nearshore location, a breaker coefficient γ at incipient breaking, a bottom friction coefficient and a bottom profile. In this way an alternating process of shoaling - reach incipient breaking - breaking - stabilizing - shoaling of reformed wave - etc. is simulated. The model is calibrated by determining best values for the stable wave factor Γ and the wave decay factor K, by minimizing the error function $\epsilon(\Gamma,K)$ in a least squares sense, based on laboratory flume tests. Both parameters turn out to vary with the beach slope. However, as the error surfaces are relatively broad and flat in the vicinity of their minimums, the dependence on the beach slope is ignored and the constant values $\Gamma = 0.40$ and $K = 0.15$ have been adopted. In this way a simple model has been developed that satisfactorily describes wave transformation due to shoaling, breaking and reformation over a wide range of beach slopes, though the predicted distribution of set-down/up across the surfzone is less adequate.

In *Dally and Dean* [1986] the regular wave model described above is used in order to develop a random wave model. Basic concept is the assumption of no wave-wave interaction in case of a random wave train propagating through the nearshore zone. As such, starting with a known histogram of wave height at some offshore location, each representative wave of the histogram is transformed as if it were associated with a regular wave train. The joint distribution of wave heights and periods for deep water derived by Longuet-Higgins [1983] is used as initial condition. This joint pdf is discretisized into a histogram of 3600 bins, each characterized by a representative wave height, period and probability weight. Next every representative 'wave' is transformed across the near shore zone independently of other waves.

While running the model a bottom slope is needed in order to determine incipient breaking. Based on laboratory observations showing breaking occurring in the trough, an alternative beach slope is used for the determination of incipient breaking, viz. the beach slope obtained by averaging over a section just seaward of the point of interest, for a distance of one wave length - compare Section 4.1.4. After having transformed all 3600 'waves' the results are ordered according to increasing wave height, at every location along the profile. In this way, spatially varying wave height distributions have been obtained across the near shore zone.

Comparison of model predictions to field data showed quite satisfactory results with regard to the wave height, except for an underprediction of $H_{1/10}$ and perhaps H_{sig} in the region just seaward of the surf zone. The basic shape of the predicted pdf appears correct, although in the surfzone, the models tends to underpredict the number of smaller waves (i.e. $H/H_{mean} < 1$). Next, Dally and Dean have investigated the interaction of currents with the shoaling and breaking process, as well as the effects of mean wave steepness and surf beat (both water level as current variations). However, these aspects are outside the scope of this study.

5 Physical interpretation of intensities

In order to make use of intensities for quantification of bathymetry it is necessary to extract information from the intensity patterns provided by the time exposure images. So, we should find out how to interpret the intensity patterns, or, in other words, find out which physical parameters are related to them. The search for these parameters is started with an investigation of the empirical correlations between observed intensity patterns and spatial distributions of several physical parameters, simulated with a wave decay model (Section 5.1). The interpretation of these results will be described afterwards, in Section 5.2. All of the investigations and results described in this chapter have been worked out in good cooperation with Nathaniel Plant, College of Oceanography, Oregon State University, during his two month stay at DELFT HYDRAULICS, October - November 1995.

5.1 Empirical correlation between intensities and breaking related properties

Comparing the bright, longshore intensity bands seen from the images to what can be observed when looking at the sea from the beach, it can be concluded that the intensities result from one or the other wave breaking related process. As the derivation of an intensity related parameter directly from physics is rather complicated the analysis is started by comparing intensities to several variables describing the processes occurring in the nearshore zone. In order to do so these nearshore processes are simulated with a numerical wave decay model, in this case the wave submodel of UNIBEST-TC, developed by DELFT HYDRAULICS. The UNIBEST model is based on the wave decay model according to Battjes and Janssen [1978], upgraded with the roller formulation according to equation (4.24) and (4.27), and the breaker lag function described by (4.33).

UNIBEST applies a coordinate system with an x-axis in shoreward direction, and the origin at the deep water location, where the boundary conditions are known. In this report the onshore UNIBEST coordinate system will be referred to by double indices (xx-axis), in order to distinguish it from the local ARGUS coordinate system. Input consists of a bathymetry, a tidal level and a set of wave parameters (wave height H_{rms}, wave period T_{sig}, angle θ). As output UNIBEST-TC can generate up to 29 predefined functions (including wave, current and sediment transport features), both time varying at one location as well as spatial distributions at one moment. The latter output can be compared to the cross-shore intensity profiles, obtained from the time exposure images.

In the present case default values according to the empirical relation (4.22) were used for the dissipation parameter α and the breaker parameter γ. Other important parameters were set to values as recommended in literature, yielding a (constant) roller slope β equal to 0.1, a breaker lag parameter λ of 2 and a bottom friction coefficient f_w equal to 0.01. Output was generated for the rms-wave height H_{rms}, the phase speed c, the corrected fraction of breaking wave Q_{sl}, the organized wave dissipation D_w, the roller dissipation Diss and de roller energy E_r. From this output two additional functions were derived, viz. E_r/c and E_r/c^2 which are involved in the considerations. Cross-shore distributions of six of these variables (Q_{sl}, D_w, Diss, E_r, E_r/c and E_r/c^2) are compared to intensity profiles within the same transect; the results are described in a statistical manner.

In statistical terms, the generation of every single UNIBEST function can be considered as an experiment. Every single experiment yields a result which is a realisation of the same stochastic process, i.e. 'generating an intensity-like profile'. A well known method to characterize the degree of resemblance between various realisations and the measured intensity profile is to establish the correlation function. Distinction should be made between the auto correlation function and the cross correlation function. The first compares the values of one and the same measured property at different times while the second compares two different realisations. When comparing cross-shore intensity profiles to spatial distributions of wave parameters, the cross correlation coefficient γ_{xy} is considered a useful parameter. In fact γ_{xy} represents the covariance $cov(x_s,y_s)$ of two stochastic variables x_s and y_s, normalized by the product of the standard deviations of the two variables. In this notation the subscribe s denotes the stochastic character of a parameter. The variance of a stochastic parameter represents a measure of the degree to which random samples of a stochastic parameter differ from its mean value. It is defined as

$$var(x_s) \equiv E\left[(x_s-\mu_x)^2\right] = E\left[x_s^2\right]-\mu_x^2 \tag{5.1}$$

in which μ_x is the mean value of the stochastic variable x and E(x) the expectation of x, which can be written as

$$E\left[h(x_s)\right] = \int_{-\infty}^{\infty} h(x)p(x)dx \tag{5.2}$$

where p(x) is the probability density function of this specific variable. Estimates of $var(x_s)$ based on N_x samples from a measured data set, can be obtained from

$$var(x_s) \approx \frac{\Sigma x^2}{N_x} - \left(\frac{\Sigma x}{N_x}\right)^2 \tag{5.3}$$

Analogous to the meaning of the variance of a single stochastic variable, the covariance represents a measure of the coherence between two different stochastic variables. It is defined as

$$cov(x_s,y_s) \equiv E\left[(x_s-\mu_x)(y_s-\mu_y)\right] = E\left[x_s y_s\right]-\mu_x\mu_y \tag{5.4}$$

In case of numerical application, the covariance estimated from N samples can be written as

$$cov(x_s,y_s) \approx \frac{\Sigma xy}{N} - \frac{\Sigma x \Sigma y}{N^2} \tag{5.5}$$

Finally, the correlation coefficient γ_{xy} is the normalized covariance of two stochastic variables. Having available a measured data set, the cross correlation coefficient can be computed from the equations (5.3) and (5.5) according to:

$$\gamma_{xy} = \frac{cov(x_s,y_s)}{\sqrt{var\,x_s}\sqrt{var\,y_s}} \tag{5.6}$$

The value of γ_{xy} can be interpreted as a measure of the linear dependence between x and y: if γ_{xy} equals 1 or -1 (which are its extreme values) x and y are said to be completely linear dependent; on the contrary, if γ_{xy} equals 0, x and y are said to be uncorrelated (which, however, does not necessarily imply there is no relation between them at all).

Knowing this, the correlations between numerical realisation and measured intensity can be computed. High correlations show that the function in question is strongly related to the measured intensity. As the resulting value of γ_{xy} depends on the cross-shore position of the compared profiles relative to each other, the computations are done several times. For every single case the profiles are shifted a certain distance relative to each other (called 'lag'), thus yielding a different value for γ_{xy}. The quality of the agreement between intensity and numerical function is judged from the maximum value of the correlation coefficient.

This method has been applied to intensity data from the cross-shore transect at Duck, y = 1100 m at October 11, 12, 14 and 17. Both measured intensities and numerical functions were normalized by subtracting the minimum value and reducing the area under the profile to 1. The profiles were shifted relative to each other with 2 meter steps. The figures given in Appendix C present some results. The graphs on the left hand side of the figure show the measured intensities (solid lines) and the numerical function in question (dashed lines) with regard to the cross-shore coordinate. The graphs on the right hand side show the value of the correlation coefficient as a function of the shift or lag between the two profiles.

These calculations have been executed for 47 different situations. A way to summarize the results is to plot the computed maximum correlations versus the corresponding lag. These plots give an impression of which function approximates the measured intensities best (see Figure 5.1).

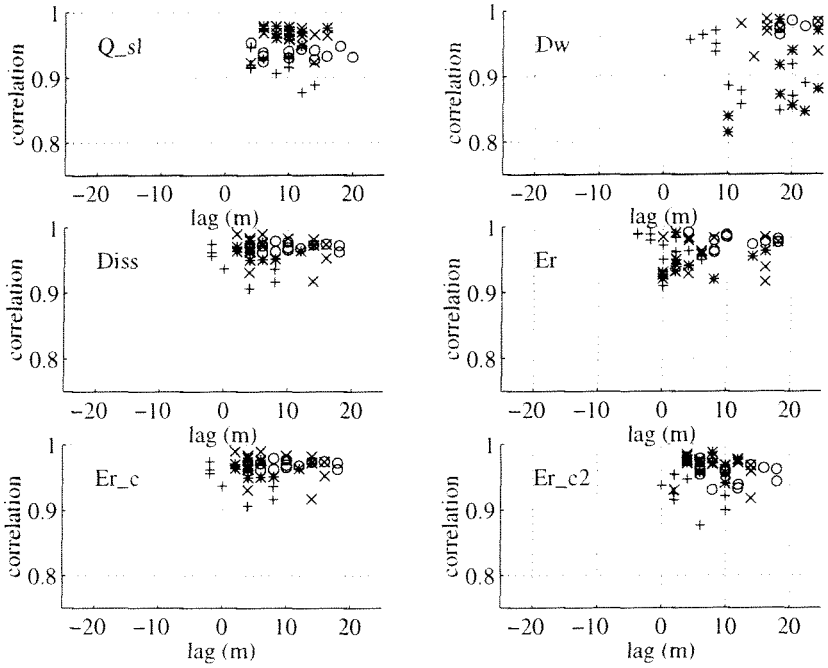

Figure 5.1 Comparison of intensity profiles to breaking related functions

The results shown in Figure 5.1 should be interpreted very carefully in a quantitative sense. It is logical to reject numerically simulated functions which show significantly worse correlation than others. As can be seen from Figure 5.1, this is the case for the fraction of breaking waves Q_{sl} (due to relatively large lag values) and the dissipation of organized wave energy D_w. However, it is difficult to distinguish between the other four, which are all roller related, as they all show relatively high correlations. In order to make a choice among them it is necessary to do some further investigation. One of the possible methods is by trying to find a physical basis from which one of the four remaining functions can be selected as the most suitable. As will be shown in the next section, E_r/c^2 could be a reasonable parameter to be related to intensities from a physical point of view.

5.2 Interpretation of the empirical correlation results

At the moment a wave breaks potential energy is transformed into kinetic energy forming a roller, which is a turbulent, aerated, bore like structure at the face of the breaking wave. While moving shoreward on this breaking wave, kinetic roller energy is dissipated through the production of turbulence, see Section 4.1.4. Due to air entrainment into the turbulent roller the water surface lights up brightly in regions where rollers are present, while relatively dark water is observed in the 'roller-free' surroundings.

Imagine one could get into one 'wet' pixel of an image obtained from an ARGUS camera. In case of a time exposure image, the resulting intensity in that pixel is the average value of 600 different snapshot intensities, recorded during the 10 minutes of time exposure while observing the waves passing by. That part of a wave covered by a roller contributes to high intensities, absence of a roller contributes to low values. Adopting an on/off model where presence of a roller yields intensities of value 1 and absence intensities of value 0 (Figure 5.2), then the resulting intensity can be estimated from the relative duration a roller is present in the considered pixel.

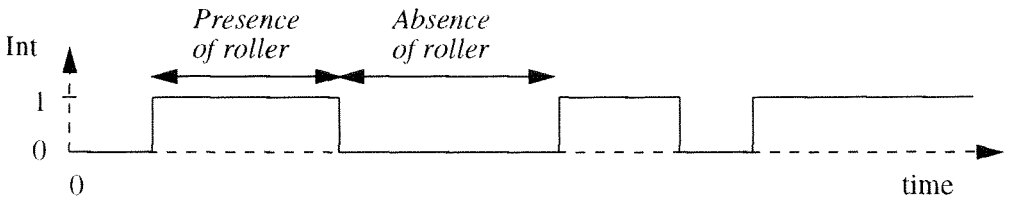

Figure 5.2 On/Off intensity model

So, the sum of all roller lengths L_r relative to the sum of all wave lengths L can be interpreted as a measure of the observed intensities. In analogy to the classification of wave decay models, two types of models can be distinguished in order to derive an expression for L_r/L, viz. the parametric and the probabilistic. They are treated in Section 5.2.1 and 5.2.2 respectively.

5.2.1 Relating intensities to a predetermined roller energy distribution

The parametric approach implies starting from the roller area as a function of the roller energy E_r, combined with an assumption regarding the shape of the roller. Deducing the roller area from the roller energy E_r implicitly means that the roller distribution throughout the surfzone is known a priori, as the production of E_r is directly related to the dissipation

of organized wave energy. In order to compute the latter a distribution of breaking wave heights has been formulated explicitly (*Battjes and Janssen* [1978]).

The amount of kinetic energy that a roller contains (per unit crest length) can be written as

$$E_{kin,roller} = \tfrac{1}{2}\rho c^2 A \tag{5.7}$$

where A is the roller area, see Figure 4.2. The fact that we are studying time averaged images allows to consider the roller energy per unit area E_r instead of individual rollers. This roller energy density E_r is obtained by dividing the expression for the kinetic energy per roller by a representative wavelength L (e.g. the wavelength at the peak frequency f_p of the spectrum):

$$E_r = \tfrac{1}{2}\rho c^2 \frac{A}{L} \tag{5.8}$$

When assuming a rectangular roller with height H_r and length L_r, then the roller area A can be written as $A = H_r \cdot L_r$. Substituting this into equation (5.8) yields the following expression for the ratio L_r/L:

$$\frac{L_r}{L} = \frac{A}{H_r L} = \frac{E_r}{\tfrac{1}{2}\rho c^2 H_r} \tag{5.9}$$

In order to eliminate the unknown H_r from this expression the roller area A has to be modelled, which can be done in several different ways.

a. By assuming a constant roller shape

In order to model a constant roller shape, the ratio H_r/L_r is assumed to be constant. So H_r can be written as $H_r = \kappa \cdot L_r$ where κ is a constant. This formulation matches the findings of *Longuet-Higgins and Turner* [1974], who stated that the height H_r of a growing roller is proportional with the distance from the wave crest, in case of steady flow (in time) and constant slope and density difference between roller and wave. Substituting $H_r = \kappa \cdot L_r$ into relation (5.9) and multiplying both sides of the equation by L_r/L yields

$$\left(\frac{L_r}{L}\right)^2 = \frac{E_r}{\tfrac{1}{2}\kappa\rho c^2 L} \tag{5.10}$$

Treating the constants κ and ρ as part of the transfer function from image intensities to numerical output function, the intensities can be related to the physical parameter $(E_r/(c^2 \cdot L))^{1/2}$ or $(E_r/c^3)^{1/2}$, after substituting $L = c \cdot T$.

b. By assuming a constant roller height H_r

According to roller model b, the process of 'self-aeration' is considered to be the dominant mechanism for the entrainment of air (*Longuet-Higgins and Turner* [1974]). This air entrainment can occur only when the turbulence at the free surface

of the roller has enough energy to overcome the surface-tension energy, and so allow eddies to project out of the surface and trap air bubbles. These local surface instabilities are related to capillary effects and therefore independent of the wave height and depth scale. As the surface-tension energy does not vary along the wave surface, a foamy layer of constant thickness H_r is supposed to be formed. As a consequence, variations in roller area A only affect the roller length L_r. Following relation (5.9), the constant H_r can be treated as part of the transfer function and intensities can be related to the wave parameter E_r/c^2.

The definite choice of the wave parameter to relate intensities to has been made based on both the statistical and the physical considerations described above. For the time being, the 'self aeration' roller model with constant H_r is adopted in case of the present study and hence, intensities are related to the wave parameter E_r/c^2. Given moreover, the observed high correlations of the intensity profile with the E_r/c^2 curve, the choice to select E_r/c^2 as the intensity matching wave parameter furthermore wins confidence.

5.2.2 Relating intensities to individual rollers

Instead of elaborating an a priori defined breaking wave height distribution, individual waves could be surveyed, which implies a probabilistic approach. In analogy to the wave by wave approach in case of wave decay modelling across the surf zone (Section 4.2), the offshore wave height distribution is discretisized, and each representative wave with height H of the histogram is transformed as if it were the height of a regular wave train.

Again, an attempt is made to describe what is observed into one single pixel. An intensity I_{pix} unequal to zero indicates the presence of a roller, a returned intensity I of zero means no roller within this pixel in case of the representative wave of height H. A roller can produce non zero intensities in a pixel if a) a wave is breaking some distance seaward of the observed pixel thus generating a roller and b) the roller is persistent enough to reach the pixel in question. Furthermore, if a wave containing a roller passes, the roller will not be seen within the pixel during all of the time the wave is passing by, but just during that fraction of time which equals the percentage of wave surface covered by the roller, i.e. the ratio L_r/L. Hence the on/off intensity model shown in Figure 5.2 is applied again. In mathematical terms the model can be formulated as follows (see Figure 5.3).

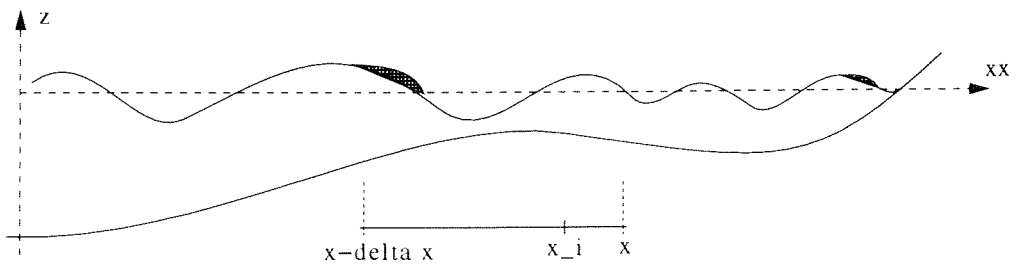

Figure 5.3 Definition sketch of individual roller model

Let x be the cross-shore coordinate of the observed pixel and Δx a seaward distance which should be at least larger than the largest persistence length l_p possible. Furthermore x_i is the x-coordinate of a cross-shore location which varies from $x-\Delta x$ to x. With these notations the probability of observing a roller (i.e. $I_{pix}(x) \neq 0$) in a pixel in case of a wave of height H can be estimated from

$$I_{pix}(x,H) = \sum_{x_i=x-\Delta x}^{x_i=x} Pr\left[H(x_i) = H_m(x_i)\right] \cdot Pr\left[l_p > (x-x_i)\right] \cdot \frac{L_r}{L} \qquad (5.11)$$

where l_p is the persistence length of a single roller and H_m the local, depth limited, maximum wave height. Next the intensity model according to (5.11) is run for each representative wave of the histogram and the results are combined, based on the known wave height distribution along the cross-shore transect. This finally yields the modelled pixel intensity:

$$I_{timex}(x) = \sum_{H_{rep}} Pr(H_{rep} = H \mid x = x) \cdot I_{pix}(x,H) \qquad (5.12)$$

In this way a mean intensity for every pixel within a cross-shore transect can be obtained, following individual waves from the seaward boundary up to the waterline. However, some additional problems arise when applying this method:

- In order to estimate the percentage of wave surface which is covered by the roller, again, an assumption is necessary concerning the shape of the roller. Spatial variations depending on cross-shore location as well as size variations during the 'lifetime' of a roller need to be taken into account.
- A formulation should be developed concerning the persistence of a roller. *Lippman and Thornton* [1994] derive an expression for this roller advection distance, as they name it, normalized with the wave length L. The wave asymmetry and the local roller energy density relative to its value at deep water turn out to be the important parameters. However, the Lippmann and Thornton expression has been derived for a strongly simplified beach profile and cannot be applied directly to the bathymetries that are found at Duck and Noordwijk.
- In case of the model formulated above, a simple on/off intensity model has been adopted. However, other schematizations may be possible, in which the resulting intensity may depend on the breaking wave height, the type of breaking or other parameters. The latter cases require the definition of a complicated intensity function, and the simple expression for L/L_r can not be applied any more.

5.2.3 Conclusion

Modelling the intensities according to the second model requires a lot of further investigation of literature (roller shape, roller persistence length) and as such it is outside the scope of this study. Apart from this it should be stressed that UNIBEST-TC, the numerical model we use here in order to generate an intensity matching parameter, has not been verified for all specific partial processes, like for example the predicted fraction of breaking waves Q_b. The latter variable might play a role when developing the model of Section 5.2.2. As the verification has been performed for its overall behaviour, one has to rely on an integral parameter of the wave breaking process.

In view of these considerations it has been decided to follow the first method and, as a first step, the roller height H_r is assumed to be constant throughout the surfzone. Thus E_r/c^2 is used as the intensity matching parameter in this first type of inverse model for the generation of an associated bathymetry.

6 The inverse model MONIMORPH

In the preceding chapters the basic components of the present monitoring technique have been treated: ARGUS related photogrammetry, wave decay modelling within the surfzone and the collection of tidal, wave and bathymetry data in the field. In this chapter these aspects are integrated into an approach which uses an inverse model called MONIMORPH, that produces a quantitative estimate of the nearshore bathymetry based on image intensities. The latter cannot be done immediately from 'raw' intensities, as will be explained in Section 6.1. The process of transferring raw intensity data into applicable input data is called 'scaling'. Afterwards the inverse MONIMORPH equations will be treated (6.2) as well as the statistical filtering method applied in order to include information deduced from images on different times (6.3). The inclusion of this filter technique has been performed by Michiel Knaapen during his 3 month stay at DELFT HYDRAULICS. The resulting overall model will be considered in Section 6.4, while in the final section an alternative, iterative approach will be mentioned.

6.1 Transferring raw intensities into applicable input data

In Chapter 5 it has been argued that it may be useful to try to interpret image intensities as a roller energy E_r divided by a squared phase speed c^2. An attempt has been made to substantiate this statement both from a statistical as well as a physical point of view, though the assumption of constant roller height through the surf zone might be rather crude. Nevertheless, in this section a sequence of operations is described which transform a raw intensity profile into a curve that approximates the cross-shore E_r/c^2 variation in a quantitative sense. Collectively, the sequence of operations forms the scaling routine.

The raw intensity data as obtained from ARGUS video images concern so-called indexed intensities, i.e. intensities with values ranging from 0 to 1. A value '0' indicates black, '1' represents white. As stated in Chapter 2, wave breaking causes bright intensity patterns in the images, so in regions of wave breaking, intensity values are increased relative to regions outside the surfzone. The goal of the scaling procedure is to filter the wave breaking related part of the observed, raw intensity data and to give it a quantitative match with the E_r/c^2 profile. The scaling routine as implemented into MONIMORPH performs this by means of four separated operations, viz. (see Figure 6.1):

a) a trend removal. Often, an intensity gradient is present across a whole image, which clearly is not wave breaking-, but rather atmospheric condition related. As such, the cross-shore intensity profile has to be adjusted by removing this trend;
b) a base correction. Outside the surf zone intensity values are unequal to zero, due to the presence of a background light intensity level. Correcting for this base level (after trend removal) yields so-called 'base intensities';
c) an upscaling of the base intensities. As the base intensities originate from indexed intensities, their values are between 0 and 1. By multiplying these base intensities with a certain factor, a quantitative match with the E_r/c^2 values is obtained;
d) a vertical shift of the intensity profile such that the intensity I_b at the seaward boundary matches the boundary value $(E_r/c^2)_b$.

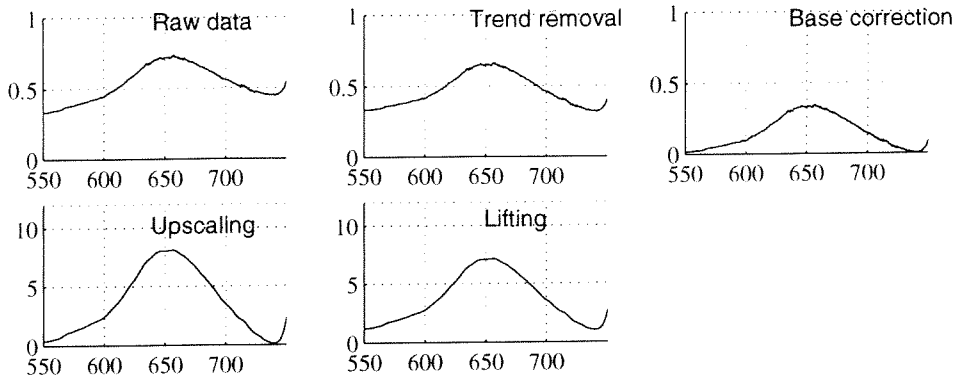

Figure 6.1 MONIMORPH scaling operations

The four operations can be described in terms of three scaling parameters, viz. a trend function $\psi_I(x)$, a base level parameter I_{base} and a scale factor SF. In case of the fourth operation no scaling parameter is needed, as the magnitude of the necessary shift can be derived from the value of E_r/c^2 at the boundary and the upscaled intensity I_b (see Section 6.1.4). As such the scaling function $F(I_{raw})$ can be written as

$$F[I_{raw}(x)] = SF\cdot([I_{raw}(x) - \psi_I(x)] - I_{base}) \qquad (6.1)$$

The aspects involved with the four respective scaling operations are treated separately, in the following subsections.

6.1.1 The trend function $\psi_I(x)$

Due to varying angles of incidence of the sunlight and atmospherical phenomena affecting the image intensities, horizontal intensity gradients may be present across ARGUS images. In order to correct for their influence, the trend function $\psi_I(x)$ is introduced. As a first approach a linear trend $\psi_I(x) = r\cdot x$ is adopted. The value of the tangent r can be determined by sampling pixel intensities along a horizontal reference line l on the screen, see Figure 6.2. As the presence of dry beach, buildings or wave breaking causes sharp intensity variations through which it is difficult to identify the actual trend, the reference line is located at deep water, in absence of wave breaking.

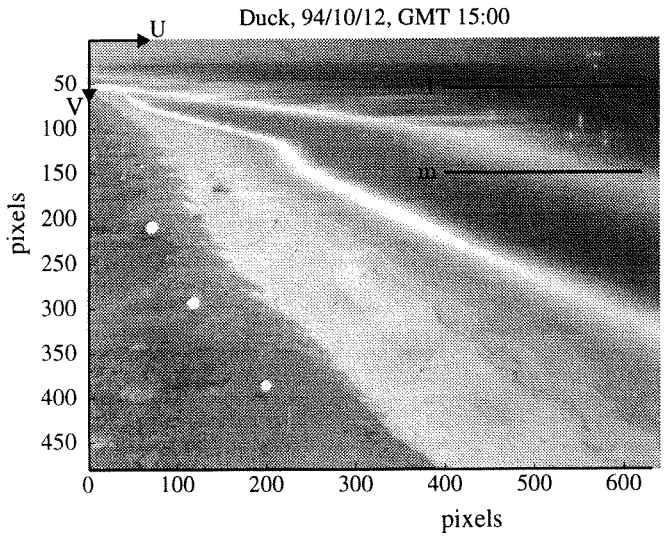

Figure 6.2 Reference line for the determination of the trend function

Closer to the camera location, within the region of interest to application of the inverse model, no spaces of plain light intensity can be detected. For this reason, the horizontal trend within those regions, e.g. along line m in Figure 6.2, is assumed to equal the gradient observed along line l. Differently formulated, the horizontal intensity trend is assumed to be independent of the vertical image coordinate.

So, by sampling pixel intensities along a deep water line l and fitting a straight line through them, the horizontal intensity gradient $\partial I(U)/\partial U = r$ is obtained, where U is the horizontal screen coordinate. The thus resulting intensity gradient per pixel can be transferred to a gradient per meter in terms of field coordinates, by making use of the photogrammetry relations described in Chapter 2. Knowing the tangent r, the trend can be removed from the raw intensity data by subtracting the trend function $\psi_t(x) = r \cdot x$ from the intensity data, starting at the seaward boundary. In this way so-called neutralized intensities are obtained.

6.1.2 The base intensity level I_{base}

The base intensity level I_{base} is added to the model as a term representing overall present background intensities. As we are interested in the 'extra' intensity part related to wave breaking, the neutralized intensities have to be corrected for this base level. In order to do so I_{base} has been defined as the minimum intensity value of the neutralized intensity profile. The so-called base intensities are obtained by subtracting this base level I_{base} from the neutralized intensity profile.

6.1.3 The scale factor SF

In order to get a profile that quantitatively matches the UNIBEST determined E_r/c^2 curve, the base intensity profile has to be scaled with a certain factor, called the scale factor SF. The value of SF represents the ratio between the areas under the E_r/c^2 curve and the intensity profile respectively. Its value has to be 'predicted' from information at the seaward boundary of MONIMORPH, as this is the only information known a priori.

In MONIMORPH the value of SF is estimated from a dimensionless wave height parameter H_{sig}/H_{max}, at the seaward boundary of the model. The reason why can be explained as follows. The roller energy E_r is determined from the roller energy balance equation (4.24). When this equation is integrated in shoreward direction and one realizes that the organized wave energy E as well as the roller energy E_r reduce to zero at the waterline, then the sum of the deep water fluxes of organized wave energy and roller energy equal the integrated energy dissipation through the surf zone. The roller energy flux $E_r \cdot c$, integrated in cross-shore direction, can be scaled with the incoming flux of organized wave energy E_f. Continuing this reasoning the integrated parameter $E_r/c^2 = E_r \cdot c/c^3$, which we are interested in as SF is related to the area under the E_r/c^2 curve, can be scaled with $(E_f/c^3)_b$. This yields

$$\frac{E_r}{c^2} \sim \frac{E_f}{c^3} = \frac{Enc}{c^3} = \frac{\frac{1}{8}\rho g H^2 n}{c^2} \approx \frac{\frac{1}{8}\rho g H^2 n}{gh} \approx \frac{1}{8}\rho H \qquad (6.2)$$

where H is a wave height and n the ratio between the group velocity c_g and the phase speed c, both defined at the boundary of the inverse model. Again, in accordance with the assumptions made in Section 4.1.1 when formulating the dissipation terms, shallow water conditions are assumed, and a wave height of the order of the water depth.

Formulated in terms of a relation between SF and $(1/8)\rho \cdot H_{sig}$ the scaling relation can not be applied generally, due to the fact that the independent variable $(1/8)\rho \cdot H_{sig}$ is not dimensionless. In order to scale the parameter $(1/8)\rho \cdot H_{sig}$ between 0 and 1, the actual incoming energy flux is related to the maximum flux as locally possible. So, $(1/8)\rho \cdot H_{sig}$ is divided by $(1/8)\rho \cdot H_{max}$, where H_{max} represents the maximum, depth limited, wave height as determined from stream function theory. A table containing H_{max}/h values as a function of $h/(g \cdot T^2)$ is given in Appendix D (*Williams* [1985], Tables C and D). In this way SF is related to a boundary parameter containing both wave height and water depth information.

6.1.4 The intensity boundary value I_b

In order to correct for overall background intensities, the minimum value of the base intensity profile is set to zero. Generally, this minimum is located at the seaward boundary of the computational area. Comparing thus scaled intensity profiles to corresponding E_r/c^2 profiles learns that the boundary value I_b generally underestimates the correct boundary value $(E_r/c^2)_b$. Apparently, the dissipation present within the region of the boundary location cannot be neglected.
Due to this offset at the boundary location, the upscaling operation fails. This will be explained with the help of Figure 6.3:

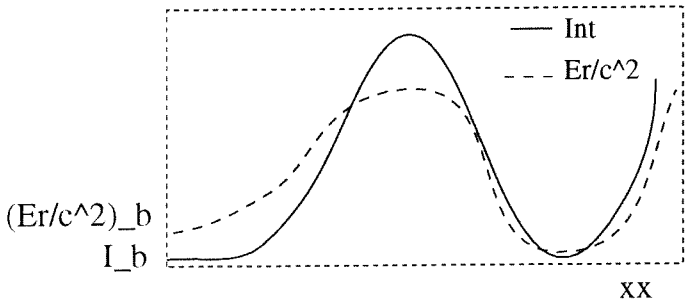

Figure 6.3 Upscaled intensity profile in case of incorrect I_b

The scale factor is defined such, that the area under the intensity profile equals the area under the E_r/c^2 curve. Due to the offset near the seaward boundary, scaled intensities in this region significantly underestimate the correct E_r/c^2 values. This is compensated by an overestimate of the E_r/c^2 values within the region of the peak, as shown qualitatively in Figure 6.4. For this reason the intensity profile is 'lifted' such that it matches the value of E_r/c^2 at the seaward boundary. The latter is either known from numerical wave computations starting at deep water (where wave data are collected) to the edge of the camera field of view, or can be set to zero in case of a camera field of view clearly stretching outside the surfzone. Knowing a scale factor SF, the boundary level can be approximated iteratively by computing a vertical shift $s = (E_r/c^2)_b/SF)-I_b$, adding this as a base level to the intensity profile, reset the area under the intensity profile to its original value, determine again the necessary shift, etc. Figure 6.4 illustrates this technique. Starting from the solid line, the dashed line is profile is obtained after the first iteration step, and the dashdot line after the second:

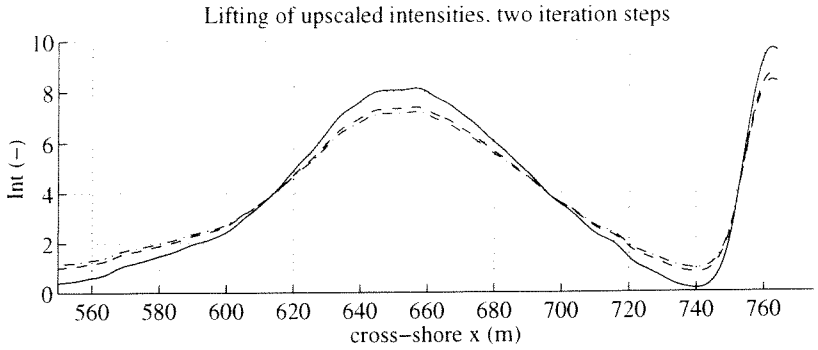

Figure 6.4 Iteratively lifting the intensity profile

After lifting the intensity profile, a better match between the two curves is observed. Unfortunately, this technique can not be applied in all situations. Considering the iterative routine in detail yields an upper limit to the intensity I_b at the seaward boundary, as will be explained here (see also Figure 6.5). When adding a shift level $s = (E_r/c^2)_b - I_b$ to the base intensity profile the original area A under the profile is increased with a term $s \cdot L_{comp}$, where L_{comp} is the length of the computational region. After resetting the area to its original value, i.e. multiplying the intensity values by a factor $A/(A+L_{comp})$, the new intensity value at the boundary reads

$$I_{b,new} = \frac{A}{A + s \cdot L_{comp}} \left(I_{b,old} + s\right) = I_{b,old} + \frac{s\left(A - L_{comp} \cdot I_{b,old}\right)}{A + s \cdot L_{comp}} \qquad (6.3)$$

Thus for $I_{b,old} > A/L_{comp}$ the subsequent boundary value decreases, instead of rising as it should. The decrease within the boundary region is corrected by a rising of the trough minimum, finally yielding a straight horizontal line limiting an area equal to $SF \cdot A$. In Figure 6.6, an incorrect lifting is shown for an (extreme) example, viz. a line that has to be lifted towards a circular profile, according to their boundary values at $x=0$. As $I_b = 0.859 > A/L_{comp} = 0.430$, it is expected that the iteration yields a horizontal line. This indeed occurs as can be seen after 2 steps already:

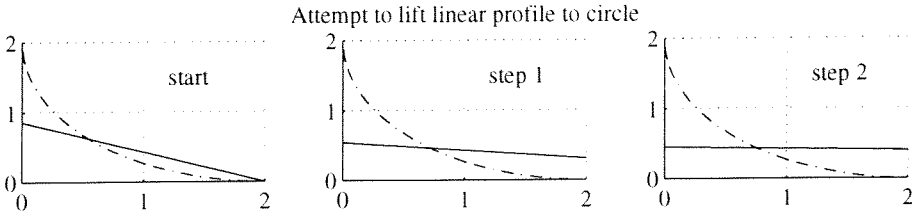

Figure 6.5 Incorrect lifting of line towards circular profile

In case of transects relatively close to the camera location with hence, relatively high intensity values I_b at the seaward boundary and associated small length scales L_{comp} of the computational region, this situation may occur.

The opposite case, I_b being too large with respect to $(E_r/c^2)_b$, will result in a negative value of s and hence, in general, negative intensities in the trough which is not realistic from a physical point of view. In MONIMORPH, these situations are dealt with by rotating the intensity profile around its most seaward point, such that the minimum intensity becomes

zero again in the trough. After resetting the area A the boundary intensity I_b has decreased while all intensities along the transect remain positive. Following the same reasoning as above, it can be concluded that for cases $s < 0$ the technique again fails if $I_b > A/L_{comp}$. Formally, though of minor importance, an additional constraint for the cases $s < 0$ reads that $s > -A/L_{comp}$.

Some alternative scaling techniques, comprising a.o. a neural network approach, have been investigated only superficially until now. However, as they might be of interest to future research within the present framework, they are mentioned in this report, in Appendix E.

6.2 Formulation of the MONIMORPH wave model

The MONIMORPH wave equations are deduced from those within the wave submodel of UNIBEST-TC, version 1995. Starting from known wave conditions at the seaward boundary and a known bathymetry, UNIBEST computes the wave properties through the surfzone in shoreward direction: the three balance equations for organized wave energy, roller energy and cross-shore momentum are solved for E (thus H_{rms}), E_r and η respectively. In case of MONIMORPH the roller energy balance equation is solved for c (thus h) instead of E_r and hence the sequence of computation of the various wave parameters is different.

6.2.1 The MONIMORPH wave equations

In chapter 4 the balance equations for wave energy, roller energy and cross-shore momentum have been described in case of waves with crests parallel to the shoreline. MONIMORPH however - like UNIBEST - is applicable to situations with waves approaching the shore with an angle θ between the wave propagation direction and the shore normal. In that case the balance equations read

$$\frac{\partial(E c_g \cos\theta)}{\partial x} = -D_{BJ} - D_{fric} \qquad \textit{wave energy} \qquad (6.4)$$

$$\frac{\partial(E_r c \cos\theta)}{\partial x} = \tfrac{1}{2}(D_{BJ} - D_{roll}) \qquad \textit{roller energy} \qquad (6.5)$$

$$\frac{\partial \overline{\eta}}{\partial x} = -\frac{1}{\rho g h}\frac{\partial S_{xx}}{\partial x} \qquad \textit{cross-shore momentum flux} \qquad (6.6)$$

where

$$S_{xx} = \left(2\frac{c_g}{c}\cos^2\theta - \tfrac{1}{2}\right)E + E_r\cos\theta \qquad (6.7)^1$$

---

[1] The formulation of S_{xx} according to (6.7) matches the expression as implemented in UNIBEST-TC. A more consistent formulation would read

$$S_{xx} = (n + n\cdot\cos^2\theta - \tfrac{1}{2})E + 2E_r\cos^2\theta$$

As the wave set-up η is the only variable affected by S_{xx} and θ approximates zero in the surfzone, the resulting deviations are of minor importance in view of the model MONIMORPH, however.

Although the expressions for the dissipation terms are treated already in Chapter 4, they are repeated here for completeness. In case of organized wave energy, bottom friction and roller energy they respectively read

$$D_{BJ} = \frac{\alpha}{4}\rho g f_p H_{max}^2 Q_b$$
$$D_{fric} = \frac{1}{8\sqrt{\pi}}\rho f_w \left(\frac{2\pi H_{rms}}{T\sinh(kh)}\right)^3 \qquad (6.8)$$
$$D_{roll} = 2\beta g c \frac{E_r}{c^2}$$

with Q_b and H_{max}, which appear in the expression for D_{BJ}, according to expression (4.5) and (4.6) respectively. The extra unknown θ is found from Snel's law

$$\frac{\sin\theta}{\sin\theta_0} = \frac{c}{c_0} \qquad (6.9)$$

where subscript 0 refers to deep water values.

The system of four equations (6.4, 6.5, 6.6 and 6.9) in four unknowns (H_{rms}, c, η and θ) is solved by integrating them shoreward. Integration is carried out for all computational points within the field of view of the camera with a step size that meets stability requirements (see Section 7.1.1). Boundary conditions are needed for H_{rms}, h, η and θ, while also the deep water wave period has to be known. Finally, E_r/c^2 has to be known along the whole transect.

The pair of unknowns (c, θ) can be determined relatively simply from the integrated equation (6.5) and Snel's law (6.9), given the E_r/c^2 curve along the profile. Consider the integrated roller energy balance, written in terms of $(E_r/c^2)\cdot c^3$ instead of $E_r \cdot c$:

$$\left(\frac{E_r}{c^2}\cdot c^3\cos\theta\right)_{i+1} = \left(\frac{E_r}{c^2}\cdot c^3\cos\theta\right)_i + \tfrac{1}{2}\cdot(D_{BJ} - D_{roll})\cdot\Delta x \qquad (6.10)$$

In this notation subscript i marks the actual computational point, while subscript i+1 denotes the next one in shoreward direction. From equations (6.9) and (6.10), c_{i+1} and θ_{i+1} can be determined iteratively.

Knowing the phase speed at the next point x_{i+1} the wavelength L_{i+1} can be computed from $L_{i+1} = c_{i+1}\cdot T$, after which h_{i+1} can be found by evaluating the dispersion relation in terms of L and h:

$$h_{i+1} = \frac{L_{i+1}}{2\pi}\,\mathrm{atanh}\left(\frac{2\pi L_{i+1}}{gT^2}\right) = \frac{L_{i+1}}{2\pi}\,\mathrm{atanh}\left(\frac{L_{i+1}}{L_0}\right) \qquad (6.11)$$

Knowing the new water depth h_{i+1} the group velocity $c_{g,i+1}$ can be determined from linear wave theory and the wave energy balance equation (6.4) can be solved for E_{i+1}:

$$(Ec_g\cos\theta)_{i+1} = (Ec_g\cos\theta)_i - (D_{BJ} + D_{fric})\cdot\Delta x \qquad (6.12)$$

As $E = (1/8)\cdot\rho\cdot g\cdot(H_{rms})^2$ the new wave height $H_{rms,i+1}$ can be determined from E_{i+1}. Similarly, the cross-shore momentum balance equation can be integrated, yielding a new wave setup value η_{i+1}, after which, finally, a new estimate of the bottom elevation z_b at x_{i+1} can be made:

$$z_{b,i+1} = z_{tide} - h_{i+1} + \eta_{i+1} \tag{6.13}$$

In this way the bottom elevation z_b along a cross-shore transect can be computed, using a forward stepping integration method. In case of MONIMORPH an Euler explicit numerical scheme has been applied. This implies that the local truncation error is of the order Δx and that the absolute stability depends on the computational step size Δx. Later on, in Section 7.2.1, the numerical stability will be investigated empirically.

6.2.2 Implementation of the MONIMORPH equations in a MATLAB routine

In order to be able to obtain the required intensity data, ARGUS images have to be processed. This is done by using the MATLAB image processing toolbox, a choice made at the Coastal Imaging Lab, Oregon. For this reason, the wave equations of MONIMORPH are also implemented in a MATLAB environment. Some aspects of this process will be mentioned here.

Determination of the computational region

Input into MONIMORPH is a matrix containing (x,y,z) coordinates along a surveyed, cross-shore transect and adjoining intensity data obtained from a rectified image (see Appendix F, 'subsequent operations when applying the inverse model'). Starting at deep water, pixel intensities are zero (= black) as they are outside the field of view of the camera. Next the surfzone is passed with useful intensity information and finally, after crossing the waterline, pixel intensities at the dry beach are measured. Along this intensity profile the boundaries of the computational region have to be defined.

The most seaward pixel within the camera field of view is clearly defined. Due to the interpolation between pixel intensities performed when rectifying the image, the most seaward pixels of the transect are slightly 'polluted' by zero intensities from outside the field of view. For this reason the first twenty, non-zero intensity values within this field of view are stripped from the profile, which implies a certain loss of information. So computations start from the twenty-first sampled intensity.

The determination of the shoreward boundary of the computational region is more complicated. In case of a surveyed bathymetry $z_b(x)$ the position of the waterline can be deduced from the intersection point between bathymetry and tidal level. In order to avoid computational problems around the waterline (c approaching to zero and hence E_r/c^2 approaching infinity) the shoreward boundary of the computational region is defined 10 m seaward of the intersection point found above. In this way some safety has been built in for possible deviations of the actual water level with regard to measured tidal level, due to wind, time effects, inaccuracy of instruments and other factors.

Normally a surveyed bathymetry will not be present. In those cases the position of the waterline has to be determined from the oblique images, or by recognizing a certain characteristic pattern in an intensity profile that indicates the shoreline. Another promising technique to

determine the shoreline position (and to be investigated in future) implies a more fundamental approach. For each snap shot that contributes to the time exposure image, every screen pixel is considered individually. It seems reasonable to assume that the intensity observed in a 'wet' pixel in the surfzone will vary strongly, while in case of a pixel at the dry beach, the observed intensity will be more or less constant for all of the 600 snap shot images. Hence, by computing the variance of the 600 observed intensities per pixel, the wet pixels will be characterized by their relatively high variances, as such defining the border between land and water.

Once the boundaries are known a computational grid is defined between these two locations, and the intensity data are interpolated to the computational points. Next the scaling routine is applied to the thus selected ('relevant') part of the intensity matrix, which finally yields the input of MONIMORPH.

Application of the breaker lag function in case of an unknown bathymetry

As described in Section 4.1.4 UNIBEST uses a weighted water depth when computing the breaking wave height H_m, in order to simulate a certain breaking delay due to inertia. The weighted water depth h_b is determined by taking into account some water depths seaward of the computational point. However, in case of the inverse model MONIMORPH, the water depth seaward of the first point is unknown. This problem can be solved by simply cutting off the weighting operation once the weighting function enters an area of unknown bathymetry. In those cases h_b and hence H_m will contain a certain error. The solution applied in case of MONIMORPH partly corrects for these errors. Starting from the first computational point the bottom is elongated seaward with a slope 1:100. Though still not perfect the resulting errors in h_b are reduced considerably. The phenomenon described here plays a role near the seaward edge of the computational region, at relatively deep water, where the fraction of breaking is relatively small. Hence, the deviation of h_b does not affect the finally computed bathymetry that strongly.

Definition of the deep water wavelength in UNIBEST

In MONIMORPH, like in UNIBEST, the deep water wavelength L_0 is used in two different situations: when solving the dispersion relation and when computing the deep water wave steepness in order to determine (the default value of) the breaking parameter γ. In the first situation this wavelength is defined as $L_0 = g \cdot T^2/(2\pi)$, while in the second the wavelength $L(x_1)$ at the first computational point is used. Actually the latter definition $L_0 = L(x_1)$ is incorrect, however, as MONIMORPH concerns an inverse model of UNIBEST-TC, the same definitions are adopted here. In order to avoid confusion when reproducing the implemented MONIMORPH relations, the author felt necessary to state this inconsistency explicitly.

Checking the performance of MONIMORPH

The correctness of the implementation of the MONIMORPH wave equations has been checked by running the model for a synthetic data set. This artificial data set (comprising 'true' E_r/c^2 values) was generated by running UNIBEST for the Duck bathymetry and corresponding wave conditions dd. 11/10/1994. The result of this computation, with spatial step size 0.5 m, is shown in Figure 6.6:

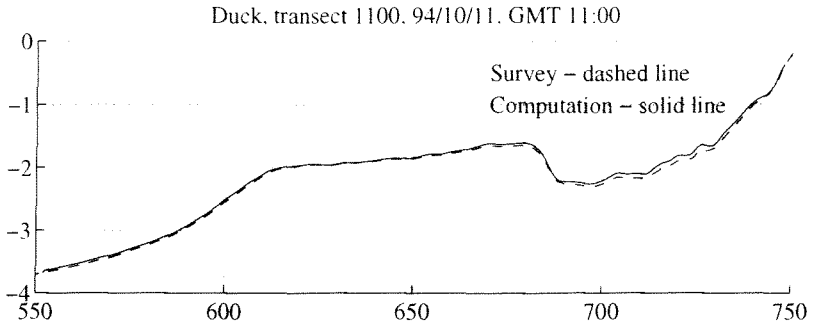

Figure 6.6 Estimate of bathymetry from a synthetic dataset

Considering the small deviations between correct and computed bathymetry, the conclusion can be drawn that no obvious numerical errors are present in the MATLAB routine, related to the process of implementing the MONIMORPH relations.

6.3 Filtering different estimates of bathymetry

Application of the model described in Section 6.2 yields an estimate of bathymetry based on one image. Nevertheless, there is more information available with respect to the same state of the system (i.e. 'bathymetry'), as the time exposure image of one hour later again provides one estimate. This new information can be added to the first result in order to improve the quality of the first estimate. The technique for doing this in a weighted way is called 'data assimilation', which can be described as a method to improve the quality of the numerical model output by integrating additional, measured information regarding the same state of the system.

Crucial part when applying data assimilation in case of MONIMORPH is the assumption that the time exposure image of one hour later adds new information regarding the *same* state of the coastal system, i.e. the assumption that morphological changes can be ignored at this time scale of order hours. Generally speaking the time scale of morphological sand bar variations (order days - months) is much longer than the hydrodynamical time scale (order minutes - hours). This yields a valid base for the assumption of unchanged bathymetry during a couple of hours. However, in case of rough wave conditions, morphological changes may occur on a much shorter time scale and the bathymetry can not be assumed constant during, say, a tidal cycle. So, a criterion regarding the length of the (cross-shore varying) morphological time scale has to be established, based on observed image intensities. From this, the number of images to be used for the filtering operation can be stated, which, in accordance with the morphological time scale, also may vary with the cross-shore coordinate xx.

Applying such a filter technique in the present case requires three operations:

- Linearizing the UNIBEST equations;
- Investigating propagation of errors through the model;
- Summing different estimates, weighted according to the reliability of the estimate.

In the following sections these three steps will be treated separately.

6.3.1 Linearizing the UNIBEST equations

Generally speaking, linearizing a function means approximating a nonlinear function by straight lines. In order to do this with sufficient accuracy, the step size between points where the expression for the line is computed should be sufficiently small. In practice, the first order Taylor polynomial is used as the gradient of the line.

Assume a function $y = f(x)$. The value of y at a nearby point $x+\Delta x$ can be estimated from the actual function value and the derivative to x at the location $x=x$, thus yielding a linear approximation:

$$f(x+\Delta x) \approx f(x) + \frac{df(x)}{dx} \cdot \Delta x \tag{6.14}$$

Hence, the effect of a small disturbance Δx is modelled according to $(df(x)/dx)\cdot\Delta x$. The same principle holds when using linearized UNIBEST equations in order to investigate the propagation of errors. In order to illustrate this statement, a one-dimensional case is treated first, before switching to the linearization of the UNIBEST equations.

Consider a system S with only one state variable Y. The value of Y may vary with time or location, however, in view of the present study it is obvious to consider a spatially varying variable. The state of S at location k is completely described by the value of its only state variable Y_k. Furthermore, the spatial variation of Y obeys a relationship given by the state function f:

$$Y_{k+1} = f(Y_k) \tag{6.15}$$

Equation (6.15) expresses that the state variable Y_{k+1} at location $k+1$ can be determined exactly from its known value Y_k at location k, given the absence of any error terms. On the contrary, measured data regarding the state variable Y_k always comprise a certain deviation ϵ_k due to measurement errors, etc. As such, the estimated state of the one-dimensional system S, based on measured data, depends on the estimated state variable $\hat{Y}_k$, written as $\hat{Y}_k = Y_k + \epsilon_k$. The offset ϵ_k can be treated in the same way as the disturbance Δx in (6.14). Consider, for example, a system where the exact state function reads $Y_{k+1} = b*Y_k^2$. In case of an estimated state variable $\hat{Y}_k$ the new estimate $\hat{Y}_{k+1}$ can be written as

$$\hat{Y}_{k+1} = b(Y_k+\epsilon_k)^2 = bY_k^2 + \epsilon 2bY_k + O(\epsilon_k^2) \tag{6.16}$$

where the second term on the right hand side matches the linear approximation $(dY_{k+1}/dY_k)\cdot\epsilon_k$ of the state function. Again it is seen that the effect of an initial disturbance is modelled as the product of the derivative to the independent variable times the initial disturbance. In this way the propagation of a small error ϵ_k through a system S can be investigated, based on a linearized relation. The same reasoning can be applied in case of a system with multiple state functions and state variables, like UNIBEST.

The UNIBEST equations describe the state of a coastal system depending on a number of parameters like wave height, water depth, density and so on. As multiple state functions are present, every single relation has to be linearized, such that partial derivatives $\partial Y_{k+1}/\partial Y_{k,i}$ are determined for every variable Y_i at location k the variable Y_{k+1} depends on. Thus a

relation $Y_{k+1} = f(Y_{k,1..n})$ reads in linearized form $[\hat{Y}_{k+1}] = [f(Y_{k,1..n})] + [P]_{1xn} \cdot [\epsilon_k]_{nx1}$ where $\hat{Y}_{k+1}$ is a 1x1 matrix containing the new estimated state variable Y_{k+1}, $f(Y_{k,1..n})$ a 1x1 matrix describing the 'exact' new state as deduced from the old state, P a 1xn matrix containing the partial derivatives $\partial f(Y_{k+1})/\partial Y_{k,i}$ and ϵ_k the nx1 error matrix describing the disturbances within each parameter. This notation is in full analogy with the one dimensional example given in the paragraph above; an example of this matrix notation is given in *Knaapen* [1996].

After having applied this linearization technique to all UNIBEST equations the results are collected into three matrix equations, for reasons of clarity. Three (column) vectors V_1, V_2 and V_3 are defined: Among these V_1 is a 9x1 matrix containing all variables that can be computed implicitly, V_2 is a 5x1 matrix containing all variables computed explicitly and V_3 a 7x1 matrix containing a number of constants:

$$\begin{aligned} V_1 &= [p \;\; c \;\; L \;\; k \;\; h \;\; c_g \;\; E \;\; H_{rms} \;\; \theta]^T \\ V_2 &= [H_m \;\; Q_b \;\; Diss_{BJ} \;\; Diss_{fr} \;\; D_r]^T \\ V_3 &= [\alpha \;\; \beta \;\; \gamma \;\; T \;\; f_w \;\; \rho \;\; L_0]^T \end{aligned} \tag{6.17}$$

Using these definitions the linearized equations of the inverse UNIBEST model can be written in matrix notation:

$$\begin{bmatrix} V_1 \\ V_2 \end{bmatrix} = \begin{bmatrix} f_1(V_1,V_2,V_3) \\ f_2(V_1,V_3) \end{bmatrix} + \begin{bmatrix} [\frac{\partial f_1}{\partial V_1}] & [\frac{\partial f_1}{\partial V_2}] \\ [\frac{\partial f_2}{\partial V_1}] & 0 \end{bmatrix} \cdot \begin{bmatrix} [\epsilon_{V_1}] \\ [\epsilon_{V_2}] \end{bmatrix} + \begin{bmatrix} [\frac{\partial f_1}{\partial V_3}] \\ [\frac{\partial f_2}{\partial V_3}] \end{bmatrix} \cdot [\epsilon_{V_3}] \tag{6.18}$$

In this notation the functions f_1 and f_2 are matrices describing the exact inverse relations, in absence of errors. The values of the elements of these two matrices are obtained from the individual equations for every variable, 'put on the right row and into the right column'. The matrices containing the partial derivatives are built up as following: Consider a matrix $[\partial f_i/\partial V_j]$ with i = 1..2 and j = 1..3; every first row of these matrices is composed of elements $\partial f_i(Y_1)/\partial V_j(Y_1)$ .. $\partial f_i(Y_1)/\partial V_j(Y_{max})$, every second row of elements $\partial f_i(Y_2)/\partial V_j(Y_1)$ .. $\partial f_i(Y_2)/\partial V_j(Y_{max})$ etc. In this way $[\partial f_1/\partial V_1]$ results into a 9x9 matrix, $[\partial f_1/\partial V_2]$ into a 9x5 matrix and $[\partial f_1/\partial V_3]$ into a 9x7 matrix. Furthermore $[\partial f_2/\partial V_1]$ yields a 5x9 matrix and $[\partial f_2/\partial V_3]$ a 5x7 matrix. Finally a matrix $[\epsilon_{Vi}]$ contains the error terms of all elements of V_i, thus $[\epsilon_{V1}]$ is a 9x1 matrix, $[\epsilon_{V2}]$ a 5x1 matrix and $[\epsilon_{V3}]$ a 7x1 matrix. Investigating these matrix dimensions results into the conclusion that the computational rules for matrices can be applied.

In fact, the two matrix equations (6.18) are the linearized inverse UNIBEST equations, which are the starting point of the further analysis of the propagation of errors through the inverse model.

6.3.2 Propagation of errors through the model

In order to investigate the propagation of errors through a model, consider the one dimensional case. As described above, the new estimate $\hat{Y}_{k+1}$ can be deduced from the old model state Y_k and a linearized error term:

$$\hat{Y}_{k+1} = f(\hat{Y}_k) = f(Y_k + \epsilon_k) = f(Y_k) + \epsilon_k \frac{\partial f(Y_k)}{\partial Y_k} \tag{6.19}$$

At the same time, according to the definition, the new estimated state of the system $\hat{Y}_{k+1}$ can be written as

$$\hat{Y}_{k+1} = Y_{k+1} + \epsilon_{k+1} \tag{6.20}$$

Eliminating $\hat{Y}_{k+1}$ from these two equations and substituting relation (6.15) yields the expression

$$\epsilon_{k+1} = \epsilon_k \frac{\partial f(Y_k)}{\partial Y_k} \tag{6.21}$$

This expression describes the way in which an initial disturbance ϵ_1 propagates through the model, as a function of the model governing relations which are represented by the function f. An important parameter is the value of the variance P_{k+1} of ϵ_{k+1}. This can be computed from $(\epsilon_{k+1})^2$ as the variance is defined as the expected value $E\{(\epsilon_{k+1}-\mu_{\epsilon,k+1})^2\}$. Taking into account that $\mu_{\epsilon,k+1} = 0$ (normally distributed), the formulation for P_{k+1} reduces to $P_{k+1} = (\epsilon_{k+1})^2$, which says that the squared value of the error ϵ_{k+1} indeed represents the variance var(ϵ). If F_k is assumed to represent the partial derivative of equation (6.21) then the variance P_{k+1} of the error term can be computed as $(\epsilon_k \cdot F_k)^2$, in this one dimensional case.

The variance of the error ϵ can be considered as a characteristic of the reliability of the estimate: Areas with large values of var(ϵ) should be interpret as areas containing information with low reliability. On the other hand, for areas with low values of var(ϵ), the opposite holds. This information can be used when combining information from different times describing the same state of the system - see Section 6.3.3.

Nowadays models describing for instance the hydrodynamics of the surfzone are certainly more complex than the one dimensional case considered above, as the state vector Y_k comprises a number of variables. Consequently, applying this reasoning to those models is also more complicated, but the basic principles do not change. Instead of computing squared values like in the one dimensional case above, some matrix operations have to be performed. Assuming again a nx1 matrix ϵ_k comprising of error terms for the variables $y_{i..n}$ and a nxn matrix F_k that contains a set of partial derivatives, then the expression for the covariance matrix P_{k+1} reads $P_{k+1} = F_k \cdot P_k \cdot F^T_k$, where P_k is a nxn covariance matrix defined as $P_k = \epsilon \cdot \epsilon^T$. So with respect to the linearized MONIMORPH equations (6.18) this operation has to be executed five times, as those relations comprise five different error matrices.

In case of the inverse UNIBEST equations, the linearization and investigation of propagating errors has been performed by Michiel Knaapen (see *Knaapen* [1996]). His results show high reliability areas where the observed intensities are relatively large, and low reliability areas where relatively low intensities are seen, for instance in the trough. This can be explained from the fact that in the trough, small variations result into relatively large gradients $\partial f(Y_k)/\partial Y_k$, thus yielding increasing error terms ϵ_{k+1} and hence lower reliability.

6.3.3 Optimizing the model output by combining weighted results

From the theory described above the reliability of the computations at any computational point can be determined by means of the covariance matrix P. Application of statistical filter techniques, in this case, is based on two central assumptions:

a. A surplus of information (concerning the same state of the system) is available such that 'extra' information can be used to update 'existing' model output.
b. The indication of reliability, offered by P, serves as a base for weighting operations when combining the available information.

The interpretation of these two aspects in case of the present problem - quantification of bar bathymetry from video observations - will be treated separately, starting with the first.

Under moderate wave conditions, i.e. no storms or hurricanes, the morphological time scale is much longer than the hydraulic time scale: the wave climate may change every hour while morphological variations are rather of the order of weeks/months, or even years. This knowledge is used when combining information from different ARGUS images. As mentioned in the introduction ARGUS images are collected every hour. Every image contains information regarding the instantaneous bathymetry. However, as the time scale of the morphological changes is much larger than the sample interval of the images, a certain sequence of images can be assumed to contain information regarding the same state of the coastal system. Or, in different words, the bathymetry is assumed to be constant during the period of collection of a certain number of images. The information supplied by the second image can be used to improve the quality of the estimate of bathymetry based on the first image, while the information supplied by the third can be used to improve the estimate based on the first and second image, etc. By concentrating on the 'best' (i.e. most reliable) information when combining information from different images an optimal estimate of the bathymetry can be deduced from the given data.

Starting point for this combining operation is the covariance matrix representing a degree of reliability - see aspect b. For every single image the elements of this matrix are known at any cross-shore computational point, in which the bathymetry is estimated. Thus, when information from K different images is taken into account, then K different estimates of the local bottom position are available, each of them linked to a certain (known) reliability. The weighted combining operation is based on the relative values of these K different reliability parameters, and can be executed most easily by a iterative routine (see *Knaapen* [1996]):

$\hat{Y}_0 = 0$
$P_0 = 999$
for k = 1 to K
  $A_k = P_{k-1}[P_{k-1}+P_{m,k}]^{-1}$
  $\hat{Y}_k = \hat{Y}_{k-1} + A_k[\hat{Y}_{m,k}-\hat{Y}_{k-1}]$
  $P_k = [I-A_k]P_{k-1}$
end

In this notation subscript m indicates the current estimate and k is a loopvariable denoting the current estimate $\hat{Y}_{m,k}$ that is due to be added to the overall estimate. $P_{m,k}$ represents the covariance matrix of this current estimate, P_{k-1} is the covariance matrix of the weighted estimate based on the combination of all k-1 previous estimates, P_k is the covariance matrix

of the weighted estimate based on the combination of all k estimates and A_k is the so called filter gain or weighting factor. Substituting the first equation of the loop into the second yields an equation that clearly shows how different estimates are 'weighted':

$$\hat{Y}_k = \frac{P_{k-1}}{P_{k-1}+P_{m,k}}\hat{Y}_{m,k} + \frac{P_{m,k}}{P_{k-1}+P_{m,k}}\hat{Y}_{k-1} \qquad (6.22)$$

As can be seen from this relation, increasing values of $P_{m,k}$ corresponding to decreasing reliability of the current estimate add smaller contributions to the final result, as the first term of equation (6.22) decreases somewhat relatively to the second.

In case of the present study twelve images per day have been taken into account in order to generate one final estimate. Doing so implies the assumption of an unchanged bathymetry during 11 hours, which may be violated under severe wave conditions. However, as the locations of wave breaking and hence the locations with 'high information density' strongly depend on local water depth, which varies with the tidal cycle, usage of 12 images covering nearly the whole tidal cycle includes the advantage of an optimal spatial distribution of the available information. Formulated in different words, highly reliable information is used along the widest part of the cross-shore profile possible, in order to generate an optimal estimate of bathymetry, weighted for twelve hours of available information.

6.4 Integration of the wave model and the scaling c.q. filtering technique

The structure of MONIMORPH can be characterized by the presence of two main loops, viz. the time loop covering twelve time exposure images (or one tidal cycle) and the cross-shore loop covering all computational points of a transect. The latter loop is called within the time loop. Every time cycle boundary conditions for h, H_{rms}, and θ are obtained from UNIBEST runs, starting at the deep water location with known depth and wave conditions towards the edge of the camera field of view, while the set up η is assumed to be zero. Furthermore 'measured E_r/c^2 values' are gained by scaling raw intensity data and the initial disturbance ϵ_{bound} within all parameters involved in the model has to be defined. Generally, the latter is done by introducing an estimated error of say 5% with 95% confidence interval, assuming normally distributed noise with mean value zero.

Once all boundary conditions and initial disturbances are known the cross-shore computational loop is called. The two submodels (hydraulic and filtering) are sequentially run, the statistical filter model computing the covariance matrix P_{k+1} from hydraulic model output at any computational point. Output regarding h and η, who determine the local bottom position given the tidal level, and the variance of h, which is used when weighting the individual results, are stored. The scheme of Figure 6.7 is meant to explain the subsequent computational steps performed by MONIMORPH.

After having run the model through the whole time loop, twelve new bathymetries according to (6.13) are computed and their relative weights are evaluated according to the calculated variances. This ultimately yields the final result, a weighted estimate of bathymetry based on observed image intensities.

A more detailed description of the data flow as necessary to run MONIMORPH is given in Appendix F, 'Subsequent operations when estimating bathymetry from video observations', together with some output examples for all separated phases.

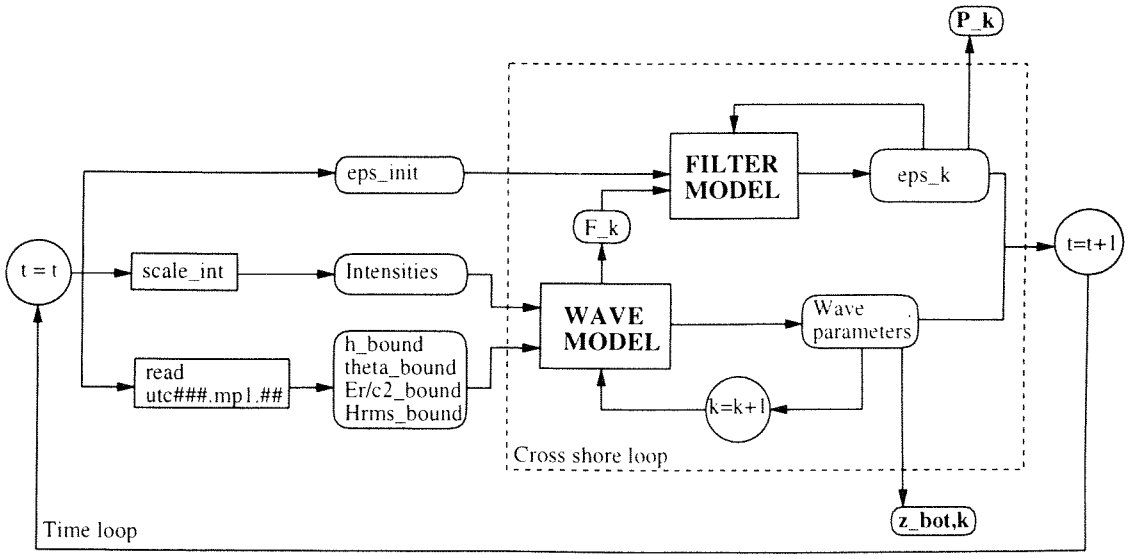

Figure 6.7 Sequence of computations of MONIMORPH

6.5 Alternative technique to quantify bathymetry from video observations

In this chapter, MONIMORPH consistently has been called an inverse model. MONIMORPH can be classified as an inverse model of UNIBEST as it computes one of the UNIBEST system parameters (viz. z_b) based on a measured property and the model equations. In MONIMORPH this has been done by immediately inverting the UNIBEST equations, however, other inverse technique are frequently based on an iterative approach. An example of the latter is given in this section.

An iterative technique starts from an initial guess of the bathymetry, judges the quality of the guess by comparing a computed feature (based on the guess) to its measured appearance and next adjusts the estimate such that the correlation between computed and desired output is improved. The example given below has been developed by Nathaniel Plant during his stay at DELFT HYDRAULICS, October - November, 1995.

Scaled intensities I(x) are assumed to be related to a certain wave breaking associated function F(x), that can be simulated with a wave decay model. For the time being E_r/c^2 has been assumed to represent this function F(x), however, the theory holds generally. The solution technique is based on minimizing the deviations between $F_{model}(x)$ and $F_{data}(x)$ at any cross-shore location, while iterating on a first guess of $h_{i,0}(x)$.

The value of $F_{model}(x_i)$ at location $x = x_i$ is considered to be a function of the local water depth h_i. If the true depth $h(x_i)$ is assumed to equal h_{true}, then ideally the relation

$$F_{model}(h_i) = F_{data}(h_{true}) \qquad (6.23)$$

would hold, indicating that the model water depth h_i equals the true water depth. Due to noise in the field data set and an offset of the initial guess, however, this will not be case. The resemblance can be improved by correcting the initial guess $h_{i,0} = h_{true} + \Delta h_i$ for the error-term Δh_i, which value is obtained from the linearized equation

$$F_{model}(h_{true} + \Delta h_i) = F_{data}(h_{true}) + \frac{\partial F}{\partial h} \cdot \Delta h \tag{6.24}$$

where the value of the partial derivative $\partial F/\partial h$ (in case of $F = E_r/c^2$) is determined from the integrated roller energy balance equation (6.10). Knowing Δh, the first estimate $h_{i,0}$ is adjusted according to

$$h_{i,1} = h_{i,0} - \Delta h \tag{6.25}$$

thus yielding a new estimate of bathymetry at $x = x_i$. The quality of the 'adjusted guess' is judged from the value of $\delta = (F_{model}-F_{data})^2$. By repeating this procedure iteratively the final result can be optimized by minimizing the value of δ. Though some effort has been spent in order to implement this model into a MATLAB routine, it does not work yet, probably due to inaccurate estimates $\partial F/\partial h$. However, the basic principles seem valid.

Clearly, the advantage of the iterative technique is that it can be applied to any physical parameter the function F is associated with, no matter the appearance of the model equations. Because of being less time consuming, however, an approach based on inverted model equations may be appreciated for the time being.

7 Performance of MONIMORPH in case of the Duck bathymetry

This chapter will treat the verification, calibration and application of the inverse model MONIMORPH in case of Duck, NC. In order to do so two different types of intensity data are used: synthetical (or artificial), UNIBEST generated data representing 'correct' E_r/c^2 values and the common 'polluted' image intensities or field data. As both data sets serve different goals of investigation, the test results derived from these are treated separately, in Section 7.1 and 7.2 respectively.

7.1 Model performance based on synthetic intensity data

Synthetic intensity data are obtained by running UNIBEST-TC in case of well-known bathymetry and offshore wave conditions. Output is generated for the cross-shore variation of roller energy E_r and phase speed c, from which the intensity matching parameter E_r/c^2 can be deduced. UNIBEST computations start at 900 m offshore where wave data are collected, while the MONIMORPH computational region reaches up to 350 m offshore (around the y = 1100 m transect), limited by the camera field of view. The MONIMORPH boundary conditions (H_{rms}, h, η and θ) are derived from the results of the UNIBEST computations at this specific location. E_r/c^2 input data have to be splined along the MONIMORPH computational grid, while no scaling operations are needed. Results are expressed in terms of the MONIMORPH axis system, which has an xx-axis pointing shoreward with the origin, like the UNIBEST axis system, at 900 m off shore.

As a first test on the correct numerical performance, Figure 6.6 shows the capability of MONIMORPH to reproduce an original bathymetry from synthetic data. Its numerical stability and dependence on an offset in the boundary conditions will be discussed in the following.

7.1.1 Test on numerical stability: varying computational step size

The effect of a changing computational step size has been investigated from synthetic intensity data of Duck, dd. October 12, 1994, GMT 11:00 hr. Offshore wave conditions of H_{rms} = 1.35 m, T_{sig} = 6.19 s and θ = 40° resulted into MONIMORPH boundary conditions of H_{rms} = 1.17 m and θ = 28° at xx = 550 m. At this location the water depth h = 3.64 m and the set up η is set to zero.

The model has been run with 9 different computational step sizes, starting from a spatial step Δxx = 0.0625 m. Next Δxx has been increased by a factor 2 for each different run, finally yielding the maximum Δxx = 16 m. Results are shown in Figure G.1 of Appendix G, 'Results stability & sensitivity analysis MONIMORPH'.

Small deviations with maximum values up to 8 cm appear to be present in the low intensity regions, where the 95% confidence bands become wider. Though they decrease with decreasing step size - differences δ are 8.37, 8.20 and 8,12 cm for Δxx = 0.25, 0.125 and 0.0625 m respectively - some error will be present irrespective of the chosen step size. This can be explained by the different way, in which the breaker lag function is applied in case

of MONIMORPH with regard to UNIBEST - see Chapter 7.2.2. Careful investigation of the absolute difference plots learns that small errors are generated within the most seaward part of the computational region, where the influence of the artificially stretched bathymetry is the largest. Furthermore, using a different bottom slope for the stretched profile yields different errors in the same region. Hence these two observations lend support to the identified error source. Another small deviation might be introduced by setting the set-up at the seaward boundary to zero. Once generated these errors propagate through the model, where they reach maximum values in regions where the influence of initial disturbances is maximal, i.e. the trough region. From a physical point of view this can be explained by considering the fact that the availability of E_r/c^2 information is minimal in the trough, hence, the influence of errors entering this region is relatively large and as such, inaccuracies arise. This statement is confirmed by the increasing band width of 95 percent confidence, outside the actual regions of energy dissipation.

Up to a computational step size of 0.5 - 1.0 m, no significant decrease of accuracy can be observed, while on the other hand, the computational time decreases rapidly (from order 2 hours for $\Delta xx = 0.0625$ m to 1 minute for $\Delta xx = 0.5$ m). From $\Delta xx = 2.0$ - 4.0 on, the inaccuracy increases considerably (compare 95 percent confidence bands) and the absolute difference starts 'jumping'. Finally, at $\Delta xx = 11$ m, the integrated value of $(E_r/c^2)\cdot c^3\cdot\cos(\theta)$ according to expression (6.12) becomes negative due to large gradient terms (with θ necessarily positive, in this case) and as a consequence, the iteration routine from which c is computed, yields imaginary values. At this moment the computation is stopped.

From the considerations above it can be concluded that a computational step size of 0.5 - 1.0 m is acceptable, for reasons of accuracy and computational time. However, as intensities can be sampled every 0.5 m (based on considerations regarding pixel resolution at the Duck site, compare chapter 2), the measure of 0.5 m is chosen as the computational step size.

7.1.2 Test on sensitivity: varying boundary conditions and input signal

Apart from numerical deviations, errors can be introduced into the model via the boundary conditions and the intensity input signal, due to measurement errors or from other mistakes. The sensitivity of MONIMORPH to an offset in either one of these factors will be investigated in this section. Again, considerations concern October 12, 1994, GMT 11:00 hr.

In order to express the 'degree of sensitivity' and hence to be able to compare the effect of different factors, four parameters have been established. The parameter δ_{max} gives the maximum difference between computed and surveyed bathymetry, negative values indicating an overestimation of the water depth. In dimensionless form this maximum absolute difference is given as δ_{max}/h, although generally, the maximum value of δ/h will be located more shoreward due to decreasing water depth, hence $(\delta/h)_{max}$ is reported. Finally, as an indication of the overall error, the mean rms error $(\delta/h)_{rms,m}$ of the dimensionless difference δ_i/h_i along the profile is given.

Offset in rms wave height H_{rms}

A (relative) increase and decrease of H_{rms} up to 5%, corresponding to a measurement error of 8 cm in significant wave height, has been investigated. Results are given in Figure G.2, Appendix G, and in Table 7.1:

$(\Delta H_{rms})/H_{rms,bound}$ (-)	δ_{max} (m)	δ_{max}/h (-)	$(\delta/h)_{max}$ (-)	$(\delta/h)_{rms,m}$ (-)
0 %	0.087	0.048	0.048	0.0010
+2.5 %	-0.190	-0.052	-0.088	0.0022
+5.0 %	-0.417	-0.106	-0.164	0.0048
-2.5 %	0.291	0.153	0.159	0.0043
-5.0 %	0.491	0.286	0.294	0.0081

Table 7.1 Sensitivity of MONIMORPH to offset in H_{rms}

The large relative differences in case of an offset of -5% are caused by the fact that the largest differences occur in the trough at about 2 m water depth; the absolute difference of, say, +0.5 m further amplifies this effect.

Results can be explained from the integrated roller energy balance, equation (6.10). An increase of H_{rms} will yield a larger dissipation term D_{BJ}, while D_{roll} is unaffected at the boundary. As E_r/c^2 values do not change either, c consequently will increase and so will the water depth (equation 6.11). Increasing water depth causes decreasing D_{BJ} and increasing D_{roll} terms, thus yielding a compensating effect after a certain distance. However, due to the decreasing dissipation of organized wave energy, the model does not damp down the initial disturbance, which can be seen clearly from the absolute difference plots. One could say that a new equilibrium bathymetry is found that links the given 'breaking curve' to the new wave height conditions, hence, an increased water depth is found along the whole computational region.

Offset in wave angle θ

Wave angles at the boundary of the MONIMORPH computational region have been varied from -5% up to 5%, which equals a maximum off set of 1.4°. Figure G.3, as well as Table 7.2 show some results.

$(\Delta\theta)/\theta_{bound}$ (-)	δ_{max} (m)	δ_{max}/h (-)	$(\delta/h)_{max}$ (-)	$(\delta/h)_{rms,m}$ (-)
0 %	0.087	0.048	0.048	0.0010
+2.5 %	0.115	0.061	0.063	0.0014
+5.0 %	0.145	0.078	0.080	0.0018
-2.5 %	0.061	0.035	0.035	0.0007
-5.0 %	0.039	0.022	0.025	0.0004

Table 7.2 Sensitivity of MONIMORPH to offset in θ

Due to the iterative solution of the two equations (6.9) and (6.10) in two unknown (θ,c) it is difficult to describe the effect of an increase of θ explicitly. Starting at the boundary, increasing θ causes the term $\cos(\theta)\cdot c^3$ to decrease (roller balance) and the term $\sin(\theta)/c$ to increase (Snel's law), though not in proportion to each other due to the presence of the dissipation terms in equation (6.10). In that case both θ and c are affected ('the offset is

spread over θ and c) yielding a smaller value for c and hence a smaller water depth. Next the dissipation term D_{BJ} increases while the roller dissipation D_{roll} decreases slightly. Both contribute to a larger water depth at the next point and as such this functions as a compensating mechanism for the initial off set $\Delta\theta$. More shoreward, in the trough, the phenomenon of amplified error terms as predicted from the linearized equations, occurs again. This mechanism - damping of the disturbance in regions of high energy dissipation and amplification in the trough - can clearly be seen from the figures in the appendix.

Introduction of a negative offset of θ into the model partly compensates for initially present deviations, due to the breaker lag function. For this reason the final result, at first sight, seems remarkably well. However, the effects are exactly opposite: initially an increase of h, which is damped c.q. amplified within the same regions of the cross-shore transect.

Offset in significant wave period T_{sig}

In accordance with the cases above, variations of T_{sig} between -5% and 5% have been considered, corresponding to a maximum offset of 0.31 s. Figure G.4 as well as Table 7.3, show the results.

$(\Delta T_{sig})/T_{sig}$ (-)	δ_{max} (m)	δ_{max}/h (-)	$(\delta/h)_{max}$ (-)	$(\delta/h)_{rms,m}$ (-)
0 %	0.087	0.048	0.048	0.0010
+2.5 %	0.060	0.018	0.040	0.0008
+5.0 %	0.095	0.028	0.045	0.0008
-2.5 %	0.127	0.068	0.069	0.0014
-5.0 %	0.169	0.092	0.093	0.0018

Table 7.3 Sensitivity of MONIMORPH to offset in T_{sig}

In case of a positive offset, both the absolute maximum difference and the relative maximum difference were located seaward of the bar, relatively near the boundary. On the other hand, a negative offset caused both maxima to be located in the trough. This explains the different order of magnitude of the relative error terms.

The behaviour of the error curve within the seaward region of the profile can be explained from the following. Increasing the wave period T has 3 effects, viz.:

a. due to the larger deep water wave length $L_0 = g \cdot T^2/(2 \cdot \pi)$, the phase speed as computed from the dispersion equation increases;
b. due to the smaller deep water wave steepness $H_{rms,0}/L_0$ the breaker parameter γ decreases and hence the region of wave dissipation is shifted seaward which corresponds to increasing values of D_{BJ} at the seaward side of the profile. Hence the phase speed will increase in this region;
c. due to the presence of the peak frequency f_p in the expression for D_{BJ}, the dissipation of organized wave energy is also affected directly by changing wave periods, increasing wave periods yielding decreasing dissipation terms.

Numerical investigation of the order of magnitude of these three phenomena learns that the third effect strongly dominates the other two, which is reasonable considering the less direct effect of T via a tanh-function, i.e. the dispersion equation (case a) and the γ-calibration curve (case b). Hence increasing wave period will yield decreasing phase speed in the region near the seaward boundary, and so does the water depth. As a consequence of that, D_{BJ} increases due to decreasing water depth, and D_{roll} decreases, so again, the same mechanism of damping/amplifying as observed in case of increasing θ takes place.

Offset in water depth h

Finally, an offset in initial water depth varying between -5% and +5% is considered, which matches a measurement error of 18 cm. Results are shown in Figure G.5 and Table 7.4.

$(\Delta h)/h_{bound}$ (-)	δ_{max} (m)	δ_{max}/h (-)	$(\delta/h)_{max}$ (-)	$(\delta/h)_{rms,m}$ (-)
0 %	0.087	0.048	0.048	0.0010
+2.5 %	0.091	0.024	0.032	0.0007
+5.0 %	-0.182	-0.048	-0.048	0.0008
-2.5 %	0.123	0.066	0.068	0.0016
-5.0 %	0.182	0.053	0.089	0.0022

Table 7.4 Sensitivity of MONIMORPH to offset in h

Except for the negative 2.5% offset, all maximum absolute differences are found near or at the seaward boundary, while generally the maximum relative differences are located in the trough.

The explanation of the resulting deviations has already been given in the paragraphs above: again a self stabilizing system is observed, which can be demonstrated from equation (6.8). A water depth, which is too large, will yield a D_{BJ} term which is too small and a D_{roll} term which is too large. Hence the gradient of roller energy flux will be smaller, finally yielding a smaller c and hence smaller h. In the trough an initial disturbance is amplified as predicted from the linearized equations, although the case $\Delta h = +5$ % (where the offset of h compensates for the 'breaker lag induced error') does not really confirm this phenomenon. It has been observed for larger initial offsets (+20%), however.

The effect of noise in the intensity signal

In order to verify the sensitivity of MONIMORPH to variations in the E_r/c^2 input signal, a normally distributed random noise has been added to the synthetic intensity profile. The noise has been defined by multiplying the 95% confidence band width of a E_r/c^2 offset (varying from 2.5% till 20%) with a random number, taken from a normal distribution with mean 0 and variance 1. Next this signal is added to the original E_r/c^2 profile. Results are shown in Figure G.6, where the difference plots show the deviations relative to the 'synthetically' computed bottom, and Table 7.5:

$2.81 \cdot \Delta(E_r/c^2)/(E_r/c^2)$	$\mu\{(\delta/h)_{max}\}$	$\sigma\{\delta/h)_{max}\}$	$\mu\{(\delta/h)_{rms,m}\}$	$\sigma\{(\delta/h)_{rms,m}\}$
0 %	$4.845 \cdot 10^{-2}$	0	$1.008 \cdot 10^{-3}$	0
+ 5.0 %	$7.783 \cdot 10^{-2}$	$5.619 \cdot 10^{-3}$	$1.285 \cdot 10^{-3}$	$5.869 \cdot 10^{-5}$
+10.0 %	$1.126 \cdot 10^{-1}$	$9.344 \cdot 10^{-3}$	$1.891 \cdot 10^{-3}$	$9.816 \cdot 10^{-5}$
+15.0 %	$1.576 \cdot 10^{-1}$	$1.373 \cdot 10^{-2}$	$2.608 \cdot 10^{-3}$	$1.639 \cdot 10^{-4}$

Table 7.5 Sensitivity of MONIMORPH to noise in the E_r/c^2 profile

The table reports the mean value μ and the standard deviation σ of the maximum relative error δ/h and the mean rms error of the dimensionless deviation δ_i/h_i, both determined from 25 runs with random noise. The value '2.81' in the header of the first column denotes that the 95% confidence level is determined from the absolute deviation by dividing it by '2.81', in case of a normally distributed error.

Although deviations increase with increasing offset of the input signal, deviations from the correct E_r/c^2 profile are not amplified by the model. Again this can be explained from the energy dissipation mechanism. Consider the case of a positive offset of E_r/c^2 at one location xx_{i+1} (i.e. intensity too large), while all other E_r/c^2 values across the transect match the synthetic intensity profile. The positive offset at xx_{i+1} yields a negative deviation of c_{i+1} (and hence h_{i+1}), as the right hand side of equation (6.10) remains constant. Thus $D_{BJ,i+1}$ will be too large and $D_{roll,i+1}$ too small and hence, the integrated roller energy balance yields a higher value for c_{i+2} (and hence h_{i+2}). In this way the initial disturbance causing a negative deviation of h is damped. In case of a random offset across the whole computational region, the model is continuously correcting for 'errors from the past', however, the basic principle is equal: disturbances are damped rather than amplified.

Conclusion

A favourable mechanism damping the initial disturbance induced by errors in the boundary conditions makes MONIMORPH suitable to deal with relevant inaccuracies (order 5%) within all boundary conditions. In general, increasing disturbances result into increasing deviations between estimated and true bathymetry, except for those cases where an initial offset corrects for the error initiated by the breaker lag function. The values of $(\delta/h)_{rms,m}$ may serve as an indication of the sensitivity of MONIMORPH to various boundary parameters. It can be seen that variation of h, θ, T_{sig} and E_r/c^2 cause deviations of the same order of magnitude: $(\delta/h)_{rms,m} \sim 0.001$ - 0.002. In case of an initial H_{rms} offset the resulting deviations become significantly larger: $(\delta/h)_{rms,m} \sim 0.008$ and even a new 'E_r/c^2 curve matching bathymetry' is reached. In addition to this, it should be noted that the reliability of the results generated in the trough is considerably less than along the rest of the profile, especially in dimensionless form relative to the local water depth.

In summary, from the sensitivity tests it can be concluded that the inverse estimation of bathymetry produces its most reliable results within the actual region of wave breaking. Furthermore, given the relatively high sensitivity to wave height variations, it is of utmost importance to have accurate wave height information.

7.1.3 The influence of the width of the camera field of view

All computations until now have been based on exactly known MONIMORPH boundary conditions, derived from a synthetic data set that has been obtained by running UNIBEST across a bathymetry stretching out to deep water. In reality however, MONIMORPH boundary conditions will have to be determined in a different way. At the seaward boundary of the MONIMORPH computational region (i.e. the boundary of the camera field of view) a water depth has to be known. In practice this means that the depth at this location, determined during the most recent survey, will be used, assuming that the morphological changes between the date of this survey and the date of the MONIMORPH run can be ignored. Furthermore, the wave conditions at this location have to be deduced from the wave conditions, measured further offshore at 8 m water depth in case of Duck. The latter can be done by running a wave propagation model in which the bathymetry is schematized to a straight line, lacking any better information.

In order to check the validity of this approach and the sensitivity of MONIMORPH for thus introduced errors, the seaward boundary of the computational region has been varied between xx_{bound} = 475 m and xx_{bound} = 650 m. Up to xx_{bound} the water depth decreases linearly from h = 8 m at xx = 0 to the known depth h_{bound} at xx_{bound}, which yields slightly different boundary conditions. From xx_{bound} to the waterline the surveyed profile dd. Oct 12, GMT 11:00 hr is used, in combination with the already determined E_r/c^2 curve. Results are shown in Figure G.7, as well as Table 7.6. The value of the parameter $H_{rms,p}/H_{rms,c}$ gives the ratio between the new 'plane profile' wave height boundary condition and the previously determined 'correct' H_{rms}.

xx_{bound} (m)	$H_{rms,p}/H_{rms,c}$	δ_{max} (m)	δ_{max}/h (-)	$(\delta/h)_{max}$ (-)	$((\delta/h)_{rms,m}$ (-)
475	1.005	0.087	0.021	0.027	0.0004
500	1.010	0.069	0.017	0.039	0.0006
525	1.010	0.051	0.022	0.035	0.0005
550	1.000	0.086	0.047	0.048	0.0010
575	0.970	0.318	0.169	0.176	0.0053
600	0.855	1.034	0.876	1.274	0.0329
625	0.814	0.970	0.735	1.023	0.0345
650	0.954	0.246	0.130	0.141	0.0066

Table 7.6 Sensitivity of MONIMORPH to changing camera filed of view

While interpreting these results it is important to realize that the surfzone starts around location xx = 550 - 575 m. In case of a boundary outside the surfzone the deep water plane beach does not cause significant inaccuracies, as can be concluded from the reported mean rms errors. In case of field data this situation might be different. Studying figure the first subplot of Figure G.7 learns, that at deeper water the band of 95% confidence becomes wider, which means that the model becomes more sensitive to disturbances, that certainly will be present in a field data set. However, in case of synthetic data the boundary can be chosen anywhere outside the surfzone.

Putting the boundary further shoreward, inside the surfzone, the linear schematization appears to be far from reality. Offshore water depths are underestimated consistently, causing too much energy dissipation seaward of the computational region and hence a computed bathymetry which is adapted to the milder wave conditions inside the computational region - compare Section 7.1.1. As a consequence the water depth is underestimated across the whole computational region.

This problem may be partly solved by assuming a so called equilibrium beach profile. The bottom depth of such a profile increases in proportion to the 2/3 root of the distance offshore. As this yields a concave profile shape, the amount of dissipation outside the computational region will decrease. However, the best way to deal with this problem is by selecting a cross-shore transect such that the seaward boundary of the camera field of view is located (just) outside the surfzone.

7.2 Model performance based on image intensity data

7.2.1 Field data used in order to calibrate MONIMORPH

As stated in Section 3.3, the Duck data set is used in order to calibrate the inverse model. Based on considerations regarding image quality, wave climate and availability of 'far away' transects, 3 days and 2 different transects have been selected to act as data source for calibration purposes. Table 7.7 summarizes some characteristics of the calibration data set:

Date	Transect	Number of images	H_{sig}		T_{sig}	
			min	max	min	max
94/10/10	1100	7	1.67	1.81	5.84	6.58
94/10/11	1100/1230	12	1.59	2.11	6.24	7.04
94/10/12	1100/1230	11	1.907	2.33	6.19	7.04

Table 7.7 Overview of field data used for the calibration of MONIMORPH

Geometry information, necessary in order to derive intensity data from the images, is available by means of binary files, which have been updated at least once per day during the October period of the Duck field experiments. For the three days considered waves typically approach the shore from NE directions, which means that they are not affected by the presence of the FRF-pier. The bathymetry comprises a relatively flat, bar like structure, that 'suddenly' drops into the trough. The minimum water depth above this bar is about 1.5 m below the low water level and 2.6 m below the high water level, for both the y = 1100 and y = 1230 m transect. The beach profile is relatively steep, with a mean slope of approximately 1:12 at the shoreline and 1:23 (transect 1100) respectively 1:16 (transect 1230) at the seaward face of the bar. During the three days considered most of the wave energy was dissipated at the flat sand bar, while a second dissipation peak, though of less importance, was observed near the waterline.

7.2.2 Calibration of the inverse model MONIMORPH

In Section 6.1 the MONIMORPH way of scaling intensities has been treated, based on a three parameter model (I_b, r, SF) with linear trend function $\psi_I(x)$:

$$\psi_{I,lin}(x) = r(x-x_{bound}) \tag{7.1}$$

The horizontal image intensity gradients are derived from pixel intensities at deep water locations. In case of Duck intensities from pixels with coordinates (U,V) = (370:620,50) have been used, corresponding to field coordinates within a nearly shore normal transect around y = 2405 m, from x = 677 m to x = 1152 m relative to the ARGUS coordinate system, which is clearly outside the surfzone. The intensity gradient along this transect can be modelled reasonably well by the linear function $\psi_{I,lin}(x) = r(x-x_{bound})$. Figure H.1, Appendix H, shows this linear approximation of the deep water intensities, as well as the transect where they are sampled. The resulting function turns out to be insensitive to a change in reference transect at deep water, i.e. the application of a different V-coordinate. If necessary (e.g. in case of survey transects relatively close to the camera location) the gradient function will be extrapolated to smaller U-coordinates.

Now that I_b is defined to equal the minimum intensity I_{min} and the tangent r of the linear trend function is can be determined, the scale factor SF can be optimized by minimizing the least squares difference between an upscaled intensity profile and the UNIBEST E_r/c^2 curve. Figure H.2 (Appendix H) compares the so scaled intensities to the 'correct' UNIBEST generated E_r/c^2 values, dd. Oct 12, transect 1100. Solid lines are the scaled intensities, broken lines the UNIBEST profiles and dotted lines the ratio between the two profiles, which ideally would be of order 1. In this way a set of 53 optimal scale factors has been generated, based on field data of the calibration data set described in Section 7.2.1. Following the theoretical considerations of Section 6.1.3, they should be related to the dimensionless boundary wave height H_{sig}/H_{max}. Figure 7.1 shows the result of this exercise, together with an exponential best fit through the data points:

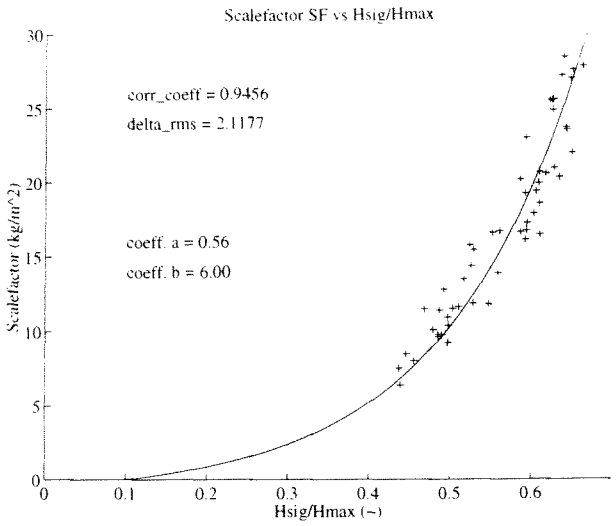

Figure 7.1 Exponential regression of SF versus H_{sig}/H_{max}

The correlation coefficient is 0.95, the rms value of the absolute difference is 2.12. The two constants defining the best fit of the exponential regression through the SF data set have been determined by minimizing the rms error term. This yields an empirical relation that can be written as

$$SF = 0.56 \cdot e^{\left(6.0 \cdot \frac{H_{sig}}{H_{max}}\right)} \tag{7.2}$$

where H_{sig} represents the significant wave height at the seaward boundary of MONIMORPH and H_{max} the adjacent maximum local wave height, derived from theoretical, stream function considerations (*Williams* [1985], Tables C and D). An example of a sequence of scaled intensity profiles during one day (based on relation (7.2)) is given in Figure H.3, Appendix H. Again, solid lines are the scaled intensities, while dashed lines represent the E_r/c^2 profiles.

7.2.3 Restrictions to MONIMORPH's ranges of input data and final results

While building and testing MONIMORPH some restrictions turned out to be appreciable in order to prevent the model from 'jamming' and 'exploding' and to improve the output results. Each of these can be justified as it can be considered to be related to a fundamental limitation of the present model, mentioned below. In order to improve the reader's understanding of what is happening inside MONIMORPH, the artificial restrictions will be treated here.

Restrictions due to polluted input data

The ratio between scaled image intensities and correct E_r/c^2 values, ideally of order 1, sometimes reaches values up to 6 or 7, in particular at relatively deep water and in the trough. In the first situation, E_r/c^2 values, being virtually zero, generally are overestimated and hence, the computed dissipation of roller energy D_{roll} is too large. Following the integrated roller energy balance (6.10) the roller energy flux will decrease and may even become negative. Imagine the latter occurs at location x_{i+1}. Solving relation (6.10) for c_{i+1} yields an imaginary value, as both E_r/c^2 and $\cos(\theta)$ cannot be negative. This is not allowed and for this reason, the computed (negative) value of the roller energy flux at xx_{i+1} is artificially set equal to its (positive) value at xx_i. As such a lower limit to the phase speed is introduced.

The opposite case, measured intensities being too small, sometimes occurs in the trough. In consequence of that, the phase speed is overestimated and the local depth becomes unrealistic large, even larger than at the seaward boundary of the computational region. In order to handle this situation, the local wavelength L_{i+1} is not allowed to exceed the value of $0.95 \cdot L_0$, where $L_0 = g \cdot T^2/(2 \cdot \pi)$, the deep water wavelength. Again, L_{i+1} is artificially set to its (allowed) value at L_i, thus imposing an upper limit to the phase speed (and hence, the water depth).

Wave height filter in order to assure a minimum dissipation level at the bar

MONIMORPH estimates the bar bathymetry from observed wave dissipation. This requires that waves actually have to break over the sand bar. An indication whether they do or not can be derived from the ratio between H_{sig} at the boundary and the theoretical maximum wave height H_{max} above the top of the bar. Based on the comparison of output results for different

wave height conditions, a threshold value of 0.6 for the ratio H_{sig}/H_{max} has been adopted as criterion for the applicability of an intensity profile. This value of 0.6 can be reasoned in the following way: a time exposure image covers a time span of 600 seconds, which roughly corresponds to 100 waves. In order to have information, at least one wave has to break, which implies that the $H_{1\%}$ of the Rayleigh distribution has to exceed H_{max}. The ratio $H_{sig}/H_{1\%}$ equals 0.66 for the Rayleigh distribution which is of the same order of magnitude as the chosen value of 0.6. The fact that the actual ratio could be chosen slightly lower can be explained from wave shoaling between the seaward boundary and the top of the bar.

Disadvantage of this approach is the fact that, generally speaking, the height of the bar crest is not known a priori. This lack of information can be handled by using the most recent estimate obtained from 'optimal' wave conditions, which is sufficient reliable as will be pointed out in Section 7.2.4. Apart from this, the estimated bar crest height is only applied to judge whether to use an image or not and as such, the impact of a certain inaccuracy will not be very significant.

Restrictions due to scaling induced errors

The actual relationship between image intensities and E_r/c^2 values is extremely complicated. The simplified neutralizing-lifting-upscaling operation as described in Section 6.1 is not capable of dealing with all features involved. Most obvious is the incorrect lifting operation if $I_b > A/L_{comp}$ for $s > 0$, see Section 6.1.4. An example of this phenomenon is given in Figure 7.2. The curved, solid line represents the base intensities, obtained during moderate wave conditions at October 19. According to the E_r/c^2 boundary condition it has to be lifted to a level $I = 0.172$. Instead of doing so the trough intensities are raised and after 8 iteration steps an almost constant intensity level is obtained. Checking the criterion learns that $A/L_{comp} = 0.090$, which indeed is smaller than $I_b = 0.106$. This effect has been observed a few times, all within transects relatively close to the camera location, and those were excluded from further analysis. The constraint regarding I_b has not been implemented yet in the present model.

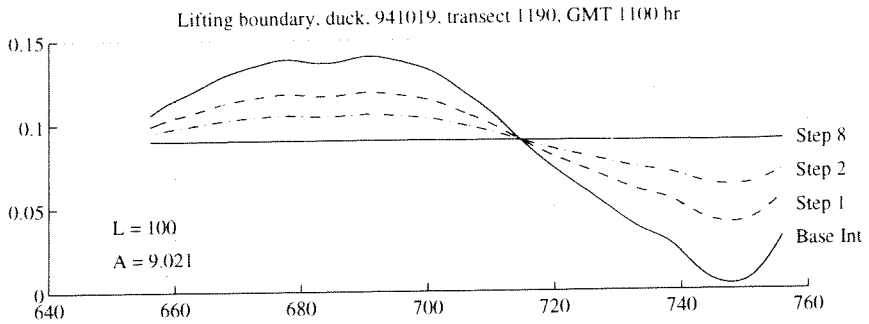

Figure 7.2 Incorrectly lifted profile Duck, 94/10/19, Transect 1190, GMT 11:00

A negative shift ($s < 0$) may result into negative intensities in the region of the trough, which are artificially corrected by an overall rotation of the intensity profile relative to the most seaward point of the profile. Slightly negative intensity values near the seaward boundary of the computational region, which occasionally occur, are set to an arbitrarily small value 0.005, as a rotation relative to the most seaward point would affect the near shore intensities too much.

In case of moderate wave conditions with wave heights H_{sig} of 1.5 to 2.5 m, the larger waves turn out to have a dominant contribution to the resulting deviations. Knowing this, the filter $H_{sig}/H_{max,bar} < 1.2$ has been applied to the wave conditions, just in order to improve the results. As such this approach is justified for operational reasons. At first sight, the wave demands $H_{sig}/H_{max} > 0.6$ ànd $H_{sig}/H_{max} < 1.2$ seem to create a very narrow window of allowed wave heights. This is not really the case due to the tidal water level variations. Consider a bar with its crest at 1.5 m below L.W. and a tidal amplitude of 1 m, which is characteristic for the Duck site. Assuming $H_{max} = 0.7 \cdot h_{bar}$ yields a wave window of 0.63 m $< H_{sig} <$ 1.26 m at L.W. and 1.05 $< H_{sig} <$ 2.1 m at H.W., so all wave conditions between 0.63 m and 2.1 m can be applied at least once during a one day computation.

Finally, an overestimation of the scalefactor SF causes MONIMORPH to simulate too much energy dissipation. As a consequence, all organized wave energy E is dissipated before the shoreward boundary of the computational region is reached. As the integration of the energy balance equation (6.4) continues, negative values of E are introduced and hence, imaginary values of H_{rms}. As this is not allowed from a physical point of view, the shoreward computational loop is interrupted.

7.2.4 Results: the Duck bathymetry as obtained from inverse computations

MONIMORPH has been tested under the widest range of conditions possible within the limits of the available Duck dataset, both with regard to bathymetry as to wave conditions. Knowing the restriction due to the positioning of a transect relative to the camera, only transects with y > 1000 m have been selected. This holds for the period till October 13, the day of adjusting the camera orientation. From this date on only the transects around y = -1200 can considered to be useful. Furthermore, days with significant waves of the order 0.5 m have been excluded. In this way the following test dataset has been generated:

Date	Number of Transects	Number of images	H_{sig} (m)		T_{sig} (s)	
			min	max	min	max
94/10/04	5	12	0.93	1.14	5.84	8.87
94/10/05	5	12	0.56	0.73	4.01	8.16
94/10/10	5	7	1.67	1.81	5.84	6.58
94/10/11	4	12	1.59	2.11	6.24	7.04
94/10/12	5	11	1.91	2.33	6.19	7.04
94/10/20	3	12	1.04	1.25	11.98	13.56

Table 7.8 Overview of field data, used for investigating the MONIMORPH performance

In case of days where a number of 5 transects is mentioned, this concerns the transects at y = 1030, 1100, 1140, 1190 and 1230 m. At October 11 the bathymetry of the 1190 transect was not available. At October 20 all transect starting from y = 1140 m could be used due to the mild wave conditions, though this is not representative for the period after changing the camera orientation (at October 13) - reference is made to Figure 7.2! All together the model performance has been tested for 27 different transects.

Due to the large deviations outside the region of wave breaking it is difficult to describe the results in terms of the whole profile. Instead, reported results will concentrate on the predicted position and shape of the breaker bar, which matches the primary goal of this study. Furthermore distinction is made between transects with (boundary) wave conditions inside the range of calibrated H_{sig}/H_{max} situations (the so-called calibration window) and those which clearly do not obey this criterion. As can be seen from Figure 7.1 the latter category comprises situations for which, during the majority of daylight-hours, the ratio H_{sig}/H_{max} is smaller than 0.44, or exceeds the value 0.66. Some representative results are reported graphically in Appendix I, 'Inverse estimates of the Duck bar bathymetry'.

Situations matching the calibration window

The results of 13 cases matching the calibration window are summarized in Table 7.9. The top of the surveyed respectively computed bar is given, as well as its location. The slope of the seaward face of the sand bar has been determined by hand, around the region of steepest rise, i.e. near the curving point of the bar face. Consequently, this point turned out to be located between xx = 580 m and xx = 620 m. Though the author is aware of the highly subjective approach followed when determining the bar slope, the method works fine as a first, qualitative indication of the resemblance in bar shape between computed and surveyed bar.

Case	No Im.	Surveyed bar			Computed bar		
		z_{top} (m)	xx_{top} (m)	m (-)	z_{top} (m)	xx_{top} (m)	m (-)
1030, 94/10/10	6	-1.77	654	1:35	-1.70	666	1:40
1030, 94/10/11	10	-1.89	637	1:36	-1.62	675.5	1:37
1100, 94/10/10	7	-1.67	657	1:30	-1.63	680	1:37
1100, 94/10/11	12	-1.85	651	1:27	-1.71	658	1:45
1100, 94/10/12	4	-1.85	651	1:27	-1.78	657	1:33
1140, 94/10/10	6	-1.68	660	1:43	-1.64	697	1:41
1140, 94/10/11	10	-1.84	661	1:37	-1.74	652	1:52
1140, 94/10/12	4	-1.53	634	1:34	-1.75	651	1:42
1190, 94/10/10	6	-1.67	644	1:39	-1.67	651	1:46
1190, 94/10/12	4	-1.43	632	1:36	-1.68	646	1:40
1230, 94/10/10	6	-1.71	642	1:33	-1.71	640	1:33
1230, 94/10/11	12	-1.68	633	1:18	-1.68	638	1:13
1230, 94/10/12	4	-1.60	636	1:10	-1.55	643	1:22

Table 7.9 Summary of MONIMORPH results for situations matching the calibration window

The number of images mentioned in the second column represents the number of 'valid' images involved into the inverse computation, after having applied the two wave condition filters. Due to extreme wave conditions on October 12, none of the 12 available images could

pass the operational constraint in case of two transects with a relatively high bar crest, the transects 1140 and 1190. For this reason, the wave window has been widened up to $H_{sig}/H_{max,bar} < 1.4$ in order to have a minimum of 4 available images, however, this has just been done in these two specific situations.

Situations not matching the calibration window

Table 7.10 outlines the results of running MONIMORPH for 14 cases not matching the calibration window. Occasionally 'noise' in low intensity regions at the seaside of the bar caused relatively large, jumping deviations from the surveyed profile, such that a reasonable estimate of bar slope could not be made. In the table below those cases are denoted by a (-).

Case	No. Img.	Surveyed bar			Computed bar		
		z_{top} (m)	xx_{top} (m)	m (-)	z_{top} (m)	xx_{top} (m)	m (-)
1030, 94/10/04	7	-1.76	651	1:33	-1.92	648	1:46
1030, 94/10/05	3	-1.68	654	1:33	-1.60	644	-
1030, 94/10/12	4	-1.74	644	1:36	-1.37	678	1:37
1100, 94/10/04	9	-1.63	652	1:36	-1.77	629	-
1100, 94/10/05	5	-1.55	656	1:37	-1.54	608	-
1140, 94/10/04	9	-1.34	673	1:43	-1.91	627	1:44
1140, 94/10/05	5	-1.35	679	1:41	-1.77	679	1:75
1140, 94/10/20	11	-1.18	676	1:40	-1.59	681	1:38
1190, 94/10/04	9	-1.64	674	1:36	-2.07	639	1:63
1190, 94/10/05	4	-1.58	647	1:36	-1.91	633	1:50
1190, 94/10/20	8	-1.14	695	1:42	-2.01	657	1:47
1230, 94/10/04	8	-1.72	655	1:29	-2.13	636	1:56
1230, 94/10/05	5	-1.57	642	1:31	-1.80	641	1:91
1230, 94/10/20	10	-1.31	693	1:49	-2.19	658	1:91

Table 7.10 Summary of MONIMORPH results for situations conflicting the calibration window

Due to the combination of a relatively mild wave climate to a relatively deep bar crest at October 5 - transect 1030, only 3 images could be used after applying the wave filters. At October 12 - transect 1030 the operational wave filter had to be raised up to 1.3 in order to have at least 4 images left.

7.2.5 Discussion on model performance

Test cases matching the calibration window

In case of preferable wave conditions MONIMORPH, applied with its normal wave window, is capable of predicting the height of the bar crest with a maximum error of 20 cm, while the majority of cases show differences even less than 10 cm (Figure I.1, I.2). Systematically the crest height is overestimated, which confirms the earlier made statement that the scaling routine tends to produce too sharply peaked E_r/c^2 profiles. This holds for all situations, except for 2 test cases: transect 1140 and 1190 of October 12. The latter two cases, being exactly the two with widened wave window, also show slightly higher deviations of 22 and 25 cm respectively. This again yields a justification to the application of the, empirically determined, operational filter.

The bar position is systematically predicted too far shoreward, though the differences are not large: generally they are of the order of 10 - 20 m. Two exceptional cases can be observed from the results in the table, originating from different error sources. First, the bar of transect 1030, October 11 differs 39 m from the correct one which is caused by an overestimate of the scalefactor, as can be seen when investigating the scaled intensity profile. As a consequence, the whole bar bathymetry is overestimated, thus yielding relatively large deviations. Second, the way of defining the top c.q. middle of the bar affects the final results. The testcase October 10, transect 1140, can be considered as an example in this respect. If the top of the computed bar has been defined in accordance with the definition of the middle of the surveyed bar (to which it is compared) the reported differences would have been smaller. However, this phenomenon is of minor importance.

Comparing the computed bar slopes to the surveyed ones and remembering the method based on which they were determined, the conservative conclusion may be drawn that the MONIMORPH predicted values 'follow' the surveyed slopes: steeper slopes in the field consequently cause MONIMORPH to predict the same. Furthermore the computed values are systematically too mild. This can be explained from the presence of noise in the intensity signal, seaward of the sand bar. As a consequence, too shallow water depths are computed in this region and a less severe rise of the bottom level is needed to reach the top of the bar, thus yielding less steep bar slopes.

When considering the spatial variation of deviations across the middle region of the bar, it can be concluded that generally, the mean error is restricted to a maximum value of 20 cm, though even better approximations are reported. Furthermore, local errors tend to increase when getting further away from the middle of the bar, though still limited to maximum values of 40 cm. In exceptional cases of extremely sharp variations of surveyed bar bathymetry MONIMORPH turns out to be incapable of reproducing these and hence, locally larger deviations may occur. Examples can be given by means of the sudden drop of the 1100-bar into the trough at October 10, where MONIMORPH tends to continue the bar (Figure I.3) and the strongly peaked bar of transect 1190 at October 12 (Figure I.4)

Test cases not matching the calibration window

Except for the test case of transect 1030, October 12, all situations within this group show significantly milder wave conditions than those, for which MONIMORPH has been calibrated.

Comparing the scaled intensity profiles to the correct E_r/c^2 curves, it can be concluded that the empirical scaling relation (7.2) cannot be applied to these situations: systematically an underestimate of the actual scalefactor is returned. At October 20, when long period waves approach the shore, this phenomenon is even amplified due to the larger value of H_{max}, adjoining the swell at equal depth. In consequence of that, the computed bathymetry suddenly 'drops' relative to the surveyed one at the moment that the region, where E_r/c^2 information is available, is reached. Several test cases clearly show this behaviour, for example transect 1140 at October 4 (Figure I.5). Adjacent deviations amount 40 to 60 cm along the middle region of the sand bar, while generally the position of the top of the bar is predicted too far seaward. Up to this point of sudden decrease the surveyed bathymetry is approximated with reasonable accuracy, although the extremely calm wave conditions at October 5 produce larger variations across the seaward bar face due to the lack of reliable information. In addition, the slope of the seaward face of the bar is systematically predicted too mild which again (like in case of the underestimated bar height) can be explained from the scalefactor being significantly too small.

The opposite case, wave conditions exceeding the range of calibrated H_{sig}/H_{max} values, result into an overall overestimate of the bar profile. Transect 1030 at October 12 clearly shows this phenomenon (Figure I.6). Like in the above described case of transect 1030, October 11, the cause can be found in an overestimate of the scalefactor, based on relation (7.2). As a consequence, a shallow bottom profile is needed in order generate the desired wave dissipation at the bar, yielding again a predicted bar position, that is located too far shoreward.

Conclusion

In case of wave conditions that match the range of calibrated H_{sig}/H_{max} values, MONIMORPH produces reliable results, from which the crest height and position of the sand bar can be determined with reasonable accuracy. In particular the behaviour of MONIMORPH in case of the transects 1140 and 1190, which were no part of the calibration data set, improves the confidence in the model. Regarding the results obtained from runs outside the calibration range it has to be concluded that they have to be ignored for the time being. Summarizing these findings, it can be stated that it is not advised to apply MONIMORPH to situations outside the calibration range of wave conditions, i.e. $0.44 < H_{sig,bound}/H_{max} < 0.66$. The same counts for the case of swell, which was not included in the calibration data set; applying the MONIMORPH scaling relation to swell conditions yields underestimated values of the scalefactor and hence, overestimates water depths. Finally, 'strange' bar bathymetries like the 'wavy' bar profile of transect 1100 and sharply varying bar dimensions cannot be handled by MONIMORPH, although the relevant parameters (top, position) are reproduced reasonably well.

A scaling induced constraint, I_b necessarily being larger than A/L_{comp}, prevented the running of MONIMORPH only once, at October 19. Though different scaling routines may be capable to handle this phenomenon, the problem is not that significant, because of the existence of a clear criterion ($I_b > A/L_{comp}$) to predict whether a profile can be applied, or not.

Once again it is stressed that the application of the wave height filters $H_{sig}/H_{max,bar} > 0.6$ and $H_{sig}/H_{max,bar} < 1.2$, based on wave dissipation and operational considerations respectively, considerably improve the results. The examples in Appendix I, concerning transect 1100 at October 4 (Figure I.7, I.8) and transect 1230 at October 10 (Figure I.9, I.10), illustrate this

statement. No situations have been met where application of the wave window deteriorated the quality of the final results.

For the time being, the computed position of the waterline has not been involved in the considerations yet. The vast majority of all testcases show a certain drop of the computed bathymetry around xx = 750 m, whereas a rise of the profile due to the dissipation peak around the waterline had been expected. This phenomenon is caused by the fact that the E_r/c^2 profile approaches infinity near the waterline, which is poorly reproduced by the scaled intensities. Second, in cases where water depths are overestimated systematically (scalefactor too small), the same counts for the depth near around the waterline. Being able - in future - to determine the position of the waterline from the image itself, this information can be applied to adjust the scalefactor artificially and determine iteratively a bathymetry that matches the boundary conditions at both sides of the profile.

8 Performance of MONIMORPH in case of the Noordwijk bathymetry

Initially, this study was intended to develop a model performing an inverse computation of the Noordwijk bathymetry. However, because of the poor quality of the available bathymetry data, MONIMORPH has been developed based on the Duck'94 dataset. In this chapter we switch back to Noordwijk, and apply the inverse model as generated for Duck. The considered Noordwijk field data are shortly discussed in Section 8.1. Some additional adjustments were necessary, which are described in Section 8.2. Some results are presented (8.3), while a conclusion is drawn in Section 8.4.

8.1 Description of the applied Noordwijk data

The present model MONIMORPH determines the shoreward boundary of its computational region from UNIBEST output, in particular the phase speed c. So, at least around the waterline, a bathymetry has to be known in order to run UNIBEST. For this reason only the Noordwijk data concerning the second period of field experiments could be taken into account. Investigation of the time exposure images during this period learns that no significant wave dissipation was occuring on the first bar (around xx = 5700 m) for mild wave conditions (H_{sig} < 1.0 m). Furthermore, all days with images of poor quality due to heavy rain were cancelled from analysis. This finally yielded the Noordwijk dataset, for which MONIMORPH has been run. Some characteristics are summarized in Table 8.1:

Date	Number of Transects	Number of images	H_{sig} (m)		T_{sig} (s)	
			min	max	min	max
95/09/24	3	12	1.15	2.17	5.45	7.20
95/09/25	3	12	1.27	1.75	6.90	8.00
95/09/28	3	12	2.03	2.63	8.60	9.10
95/09/29	3	12	1.59	2.46	7.25	7.90

Table 8.1 Overview of suitable Noordwijk field data

The three transects considered concern 81.05, 81.05 and 80.95, which are situated at y = -850 m, y = -950 m and y = -1050 m respectively. All of them stretch outside the surfzone. Finally, a storm has to be mentioned, occurring on September 27 with wave heights up to 3.40 m.

8.2 Noordwijk related adjustments of MONIMORPH

While applying MONIMORPH to the Noordwijk ARGUS site some additional problems were met. The way they were handled is shortly discussed here.

a. Lacking reliable bathymetry data for the period September 20 - October 6, UNIBEST has been run with fictitious beach profiles. They were obtained by combining the Rijkswaterstaat echosoundings of June 1995 and the waterleveled profiles of the second period of field experiments. As such, the shoreward boundary of MONIMORPH's computational region could be determined at least.

b. Application of the Duck based calibration relation (7.2) consistently produced scalefactors which significantly underestimated the values necessary for a satisfactory order of magnitude match with the E_r/c^2 values, obtained from running UNIBEST. The mismatch has been explained from a depth-dependence of relation (7.2). As the Noordwijk transects stretch out to deeper water, a larger value of H_{max} is found at the boundary and hence, a lower value of SF. For the time being, this has been solved by rewriting the scaling relation in terms of an independent variable H_{sig}/H_{max}, defined at a reference depth. This depth was chosen at a bottom elevation z_b = -4.5 m, below MSL. Plotting the 53 Duck-scalefactors versus the ratio H_{sig}/H_{max} at reference depth, and determining a best fit through the data points yielded the scaling relation

$$SF = 1.0 \cdot e^{\left(5.2 \cdot \frac{H_{sig}}{H_{max}}\right)} \qquad (8.1)$$

The correlation coefficient is 0.84, the rms value of the absolute difference is 3.35. Despite the worse correlation with regard to the exponential fit (7.2), relation (8.1) has been applied in case of Noordwijk.

c. During all days the intensity values of the first and the last image during daylight hours (i.e. GMT 6:00 hr and GMT 17:00 hr) were considerably lower than the image intensities of the hours in between. For this reason they have been excluded from analysis.

d. Occasionally, all organized wave energy was dissipated before reaching the waterline as determined from UNIBEST output. As a consequence, unrealistic shallow water depths are computed within regions with relatively high reliability, according to the variance of the error term. Again, these few cases are also excluded from analysis.

8.3 Results: the Noordwijk bathymetry as obtained from inverse computations

The only way to judge the quality of the inversely computed bathymetries is by comparing them to the corresponding waterleveled beach profiles. In analogy to the findings at Duck, the scalefactor is clearly underestimated in case of relatively mild wave conditions, outside the range of calibrated conditions. In case of Noordwijk, this concerns the runs dd. 95/09/24, 95/09/25 and 95/09/29. As a consequence, the water depths are considerably overestimated. Judged as unreliable, they are not treated any further here.

Appreciable wave conditions were met on September 28. The results of this day are reported graphically in Appendix J, 'Inverse estimate of the Noordwijk bathymetry'. The inversely computed bathymetries are compared to the waterleveled beach profiles of September 30, as a reliable survey could not be performed on September 28 due to the rough wave conditions. A satisfactory quantitative match is observed within the region of the swash bar (around xx = 5875 m), based on which the computed position and height of the first bar (around xx = 5700 m) wins confidence. Unfortunately, in this case no comparison to field data can be made.

As an indication of consistency in the longshore behaviour of MONIMORPH, computations have been executed for 11 transects with 20 m spacing, between y = -850 m and y = -1050 m. The results are presented by means of a three dimensional impression of the Noordwijk bathymetry dd. 28/09/1995, given in Figure 8.1:

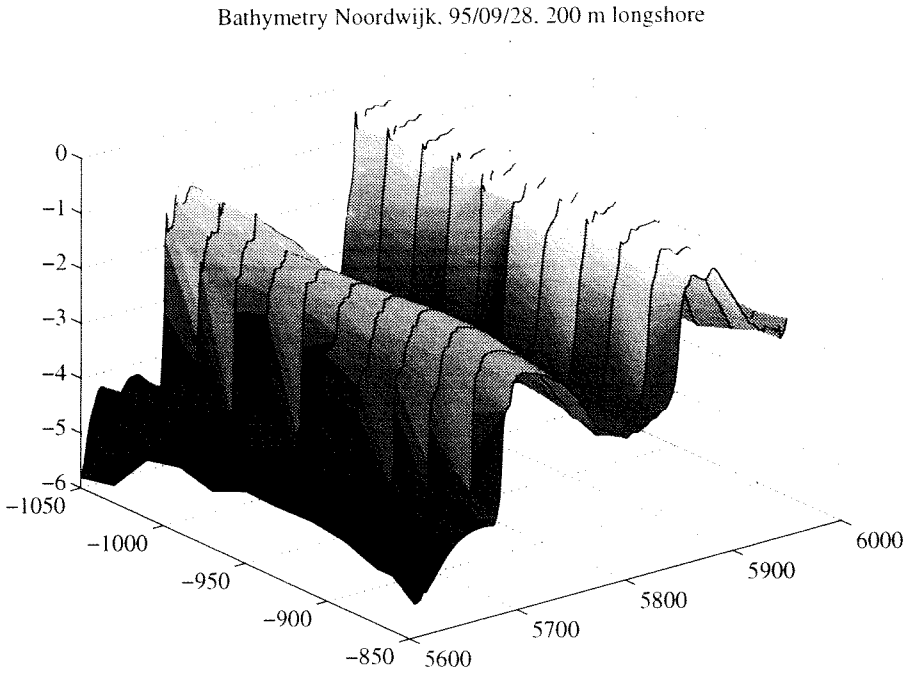

Figure 8.1 Impression of Noordwijk bathymetry, 28/09/95

8.4 Conclusion

Lacking reliable bathymetry data it is difficult to judge the quality of the MONIMORPH results in case of the Noordwijk site. From the results reported above, two restrictive conclusions can be drawn:

a. MONIMORPH can not yet be applied to situations with wave conditions outside the range of calibrated conditions. In particular in case of relatively mild conditions, the scalefactor is underestimated considerably. This finding is in accordance with the conclusion that could be drawn after testing MONIMORPH in case of the Duck site.

b. It is yet unknown whether the scaling parameters derived for the Duck dataset can be applied to an arbitrary ARGUS site. From the Noordwijk application it was learned

that the scaling parameters are depending on a H_{sig}/H_{max} which is depth dependent. Further field experiments would be required to resolve these questions.

As a final conclusion (see Figure 8.1), it can be stated that these first results are promising in character and that they justify further research in order to develop this inverse technique.

9 Conclusions and recommendations

In this thesis an inverse model called MONIMORPH has been developed, that quantifies bar bathymetry from video observations of the surfzone. The major conclusions with regard to model performance and the range of applicable wave conditions are summarized in Section 9.1. In Section 9.2 recommendations with respect to the further development of the model are given.

9.1 Conclusions

MONIMORPH generates a quantitative estimate of bar bathymetry by relating observed, time-averaged image intensities to the roller energy density E_r divided by the squared phase speed c^2. Image intensities are 'translated' into E_r/c^2 values by means of a scaling routine, comprising three scaling parameters (r, I_{base}, SF). The trend removal parameter r is derived from the deep-water intensity gradient, while the background intensity parameter I_{base} is stated to equal the minimum intensity along a transect. The model has been calibrated by generating a set of optimal scalefactors SF, based on 53 different images. A scaling relation has been established by relating the optimal values of SF to the ratio H_{sig}/H_{max} at the seaward boundary of MONIMORPH's computational region. Individual estimates of bathymetry, based on a single time exposure image, are combined by means of a data assimilation technique.

The sensitivity of MONIMORPH to an offset in either one of its input parameters (H_{rms}, h, θ, T_{sig}, E_r/c^2) has been investigated, based on a synthetic dataset. Due to a favourable mechanism damping initial disturbances, the model was concluded to be suitable to deal with relevant inaccuracies of the order of 5%. In case of an offset ΔH_{rms} the sensitivity turned out to be relatively large, which stresses the importance of the availability of accurate wave height information.

The performance of MONIMORPH in case of field data regarding the Duck site has been investigated for 27 different transects. For situations matching the calibration wave conditions (i.e. matching the window $0.44 < H_{sig}/H_{max} < 0.66$ at the seaward boundary), the model is reasonably well capable of predicting the bar bathymetry: The top of the bar is estimated with an accuracy of 10 to 20 cm, while across the bar, the mean deviation amounts 30 to 40 cm. The position of the bar crest is systematically predicted too far shoreward, though differences are small (10 to 20 m) considering the mild slope of the bar. The situations not matching the calibration window mainly concern relatively mild wave conditions ($H_{sig}/H_{max} < 0.44$). For these cases the scalefactor SF is underestimated systematically, hence, water depths are overestimated. For the time being these cases can not be handled by MONIMORPH.

Some additional constraints regarding the range of allowed input data should be mentioned. In order to improve model output, two wave filters have been introduced which judge the applicability of a single image: only images for which $H_{sig}/H_{max,bar} > 0.6$ ànd $H_{sig}/H_{max,bar} < 1.2$ are suitable for analysis. Intensity profiles, for which the boundary value I_b exceeds the ratio A/L_{comp} (see Section 6.1.4), are incorrectly processed by the scaling routine. Hence they were cancelled from the analysis. Finally it is advised to start the computations as close as possible to the seaward boundary of the region of actual wave breaking, in order to avoid inaccuracies due to noise from more seaward located, 'low-information' regions.

Eventually, the performance of MONIMORPH in case of field data regarding the Noordwijk site has been investigated. Again, it was concluded that the model can not be applied to situations outside the range of calibration conditions. Furthermore, a depth-related adjustment of the SF-scaling relation turned out to be necessary.

9.2 Recommendations for further investigation

An important topic to be investigated further is the determination of the waterline from time exposure images. The approach mentioned in Section 6.2.2 (which was based on the variance of the pixel intensities of 600 succeeding snap shot images) seems promising. Knowing the position of the waterline, the scalefactor can (iteratively) be adjusted such, that the computed bathymetry fits to the known bathymetry both at the seaward side of the computational region, as well as the shoreward side. As intensities poorly match the E_r/c^2 profile near the waterline (because of c approaching zero), it might be necessary to select a reference depth of say 1 m below MSL to provide a criterion, based on which the scalefactor can be adjusted.

All deviations between computed and surveyed bathymetry can be explained immediately from a comparison of the scaled intensity profile to the simulated E_r/c^2 profile. Hence they originate either from noise in the field data, or from a less correct choice of E_r/c^2 as the intensity matching parameter, or from an incorrect scaling routine. Starting with the latter cause, the MONIMORPH scaling routine is a severe simplification of the complex reality. Probably it is even too complicated to model the path from light signal via pixel intensity to wave parameter, based on optical considerations. Hence it seems reasonable to adopt a neural network approach, which is capable of dealing with fuzzy information whose functional relation is not clear. A first introduction on this is reported in Section E.4 of the appendix.

Solving for the second cause by adopting a different intensity matching parameter would completely change the inverse model. Adopting the assumption of a constant roller shape H_r/L_r yields $(E_r/c^3)^{1/2}$ as the intensity matching parameter. The cross-shore variation of both parameters is plotted in Figure 9.1, in case of Duck, transect 1100 dd. 94/10/11, GMT 11:00 hr.

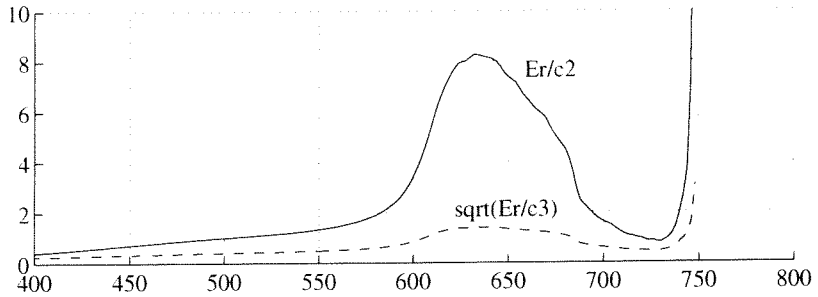

Figure 9.1 E_r/c^2 profile vs. $(E_r/c^3)^{1/2}$ profile Duck

As can be seen from Figure 9.1, the $(E_r/c^3)^{1/2}$ curve is considerably less peaked than the E_r/c^2 profile. Comparison of these two profiles to the intensity profiles learns that it may be questioned whether the $(E_r/c^3)^{1/2}$ is capable of reproducing the sharp intensity peak in case of relatively rough wave conditions. On the contrary, its (visually observed) resemblance

with intensity profiles in case of mild wave conditions is much better. The latter conditions provide exactly the situations for which the present model based on E_r/c^2 fails. Probably, this yields a base to widen the range of wave conditions MONIMORPH can be applied to. Another different solution would imply the adoption of the probabilistic approach, described in Section 5.2.2. This however, requires a lot of further research and will be a considerable task to be carried out in future.

In case of the present model, a constant bathymetry has been assumed during a whole tidal cycle. The validity of this assumption has to be investigated, in particular in case of rough wave conditions. Probably, the morphological time scale can be related to observed pixel intensities, or the offshore wave conditions. Notice that this time scale may even vary in cross-shore direction. Based on the local morphological time scale, the number of images to be used for data assimilation can be determined.

In summary, an inverse technique to derive a fixed bar bathymetry from video observations has been developed, the accuracy of which may be improved by further analysis. It is further recommended to investigate whether the present model is already capable of monitoring dynamic bar behaviour on a timescale of several months, since this may require less severe accuracies. This would allow for assimilation techniques for morphodynamic cross-shore process modelling. Sofar the focus has been on clearly linear bar geometries, but it is expected that further study would allow to derive more rhythmic geometries in longshore direction. This, finally, would allow for assimilation techniques for two-dimensional horizontal morphological process modelling.

Acknowledgements

The research in this thesis has been performed as a Master's study at the Faculty of Civil Engineering, Hydraulic and Geotechnical Engineering Division, of Delft University of Technology.

This report is partly based on work in the PACE-project and in the SAFE-project, in the framework of the EU-sponsored Marine Science and Technology Programme (MAST-III), under contract no. MAS3-CT95-0002 and PL-950057 respectively.

I would like to thank my committee of supervision - Prof. Marcel Stive, Prof. J.A. Battjes and Dr. Dano Roelvink - for their guidance up to the conclusion of my Master's study and for their many valuable recommendations.

I also cooperated with Nathaniel Plant and Michiel Knaapen intensively, during their stays at DELFT HYDRAULICS. Nathaniel and Michiel, I look back with satisfaction and pleasure to the time we worked together and I hope both of you will recognize a lot of your ideas in this report.

A word of thanks should be expressed to the people I met at the Noordwijk beach: Dr. Aart Kroon, Prof. Rob Holman, Reimer de Graaff, Sanne van Bruijnsvoort, Ineke Touwen and Judith Spelberg. Thank you for allowing this Delft student to be involved in the Utrecht field campaign. Furthermore, Aart has been very helpful in providing the Noordwijk wave-, tide- and bathymetry data, while Prof. Holman guided me through my first careful steps in the field of video imaging.

Finally, I would like to thank my colleagues at DELFT HYDRAULICS, in particular Ad Reniers, Maarten Dingemans, Irv Elshoff and Martje Looman, for offering the pleasant atmosphere to do my Master's work and showing so much interest in my project.

As I will be continuing this work in a PhD study, I am looking forward to further cooperation with all participants mentioned above.

References

Battjes, J.A. and Janssen, J.P.F.M. (1978). Energy loss and set-up due to breaking in random waves. *Proc. of 16th Int. Conf. on Coastal Eng.*, Hamburg. ASCE, pp. 569-587.

Battjes, J.A. and Stive, M.J.F. (1985). Calibration and verification of a dissipation model for random breaking waves. *J. Geophys. Res.*, 90(C5):9159-9167.

Beyer, D., 1994. Energy dissipation in random breaking waves: the probability of breaking, *Master thesis*, Delft University of Technology.

Dally, W.R., Dean, R.G. and Dalrymple, R.A. (1984). A model for breakwater decay on beaches, *Proc. 19th Int. Conf. Coastal Eng.*, Houston. ASCE, pp. 82-98.

Dally, W.R. and Dean, R.G. (1984). Transformation of random breaking waves on surf beat. *Proc. 19th Int. Conf. Coastal Eng.*, Houston. ASCE, pp. 109-123.

DELFT HYDRAULICS (1995). Yearly averaged sediment transport along the Dutch coast. *DELFT HYDRAULICS*, report H 2129.

Dingemans, M.W. (1996). Water wave propagation over uneven bottoms, *World Scientific* (to be published), appr. 900 pp.

Hesselmans, G.H.F.M. (1990). Measurements of Three-dimensional Waves. Operational and technical feasibility of the Stilwell method. *DELFT HYDRAULICS*, report H 465.

Hofmann-Wellenhof, B., Lichteneger, H. and Collins, J. (1992). GPS, Theory and Practice. *Springer-Verlag*, Wien New York.

Holman, R.A, Sallenger Jr, A.H., Lippmann, T.C and Haines, J.W. (1993). The application of video image processing to the study of nearshore processes. *Oceanograppy*, Vol. 6, No 3.

Knaapen, M.A.F. Filtering of bathymetry estimations gained by video imaging of breaking waves. *In preparation.*

Le Méhauté, B. (1962). On non-saturated breakers and the wave run-up. *Proc. 8th Int. Conf. Coastal Eng.*, Mexico City. ASCE, pp. 1178-1191.

Lippmann, T.C. and Thornton, E.B. The spatial distribution of wave rollers on a barred beach. *Submitted to J. Geophys. Res.*

Lippmann, T.C. and Holman, R.A. (1989). Quantification of sand bar morphology: A video technique based on wave dissipation. *J. Geophys. Res.*, 94(C1):995-1011.

Longuet-Higgins, M.S. and Turner, J.S. (1974). An 'entraining plume' model of a spilling breaker. *J. Fluid. Mech.*, 63(1):1-20

Longuet-Higgins, M.S. (1983). On the joint distribution of wave periods and amplitudes in a random wave field. *Proc. Roy. Soc Lond.*, A389, pp. 241-258.

Mase, H. and Iwagaki, Y. (1982). Wave height distributions and wave grouping in surf zone. *Proc. 18th Int. Conf. Coastal Eng.*, Capetown. ASCE, pp. 58-76.

Mase, H., Sakamoto, M. and Sakai, T. (1995). Neural network for stability analysis of rubble-mound breakwaters. *J. of Waterway, Port, Coastal and Ocean Engineering*, 121(C6):294-299.

Mizuguchi, M. (1982). Individual wave analysis of irregular wave deformation in hte nearshore zone, *Proc 18th Int. Conf. Coastal Eng.*, Capetown. ASCE, pp. 485-504.

Nairn, R.B., Roelvink, J.A. and Southgate, H.N. (1990). Transition Zone width and implications for modeling surf zone hydrodynamics. *Proc. 22nd Int. Conf. Coastal Eng.*, Delft. ASCE, pp. 68-81.

Rijn, L.C. van (1994). Principles of fluid flow and surface waves in rivers, estuaries, seas and oceans. *Aqua Publications*, 335 pp.

Roelvink, J.A. (1993). Dissipation in random wave groups incident on a beach. *Coastal Eng.*, 19:127-150.

Roelvink, J.A., Meijer, Th.J.G.P., Houwman, K., Bakker, R. and Spanhoff, R. (1995). Field validation and application of a coastal profile model. *Proc. Conf. Coastal Dynamics*, Gdansk. In press.

Shuto, N. (1974). Nonlinear long waves in a channel of variable section. *Coastal Eng. in Japan*, Vol. 17, pp. 1-12.

Snyder R.L., Smith L., and Kennedy R.M. (1983). On the formation of whitecaps by a treshold mechanism. Part III: Field experiment and comparison with theory. *J. Phys. Oceanography*, 13(8):1505-1518

Stive, M.J.F. and Dingemans, M.W. (1984). Calibration and verification of a one-dimensional wave energy decay model. *DELFT HYDRAULICS*, report on investigation M 1882.

Stive, M.J.F. and De Vriend, H.J. (1994). Shear stresses and mean flow in shoaling and breaking waves. *Proc. Int. Conf. Coastal Eng.*, Kobe. ASCE, pp. 594-608.

References (continued)

Svendsen, I.A. (1984). Wave heights and set-up in a surf zone. *Coastal Eng.*, 8:303-329.

Thornton, E.B. and Guza, R.T. (1983). Transformation of wave height distribution. *J. Geophys. Res.*, 88:5925-5938.

Wijnberg, K.M. (1995). Morphologic Behaviour of a Barred Coast over a Period of Decades. PhD thesis. *Utrecht University*, Utrecht.

Williams, J.M. (1985). 'Tables of progressive gravity waves', *Pitman*.

Appendix A

Map of Central Dutch Coast

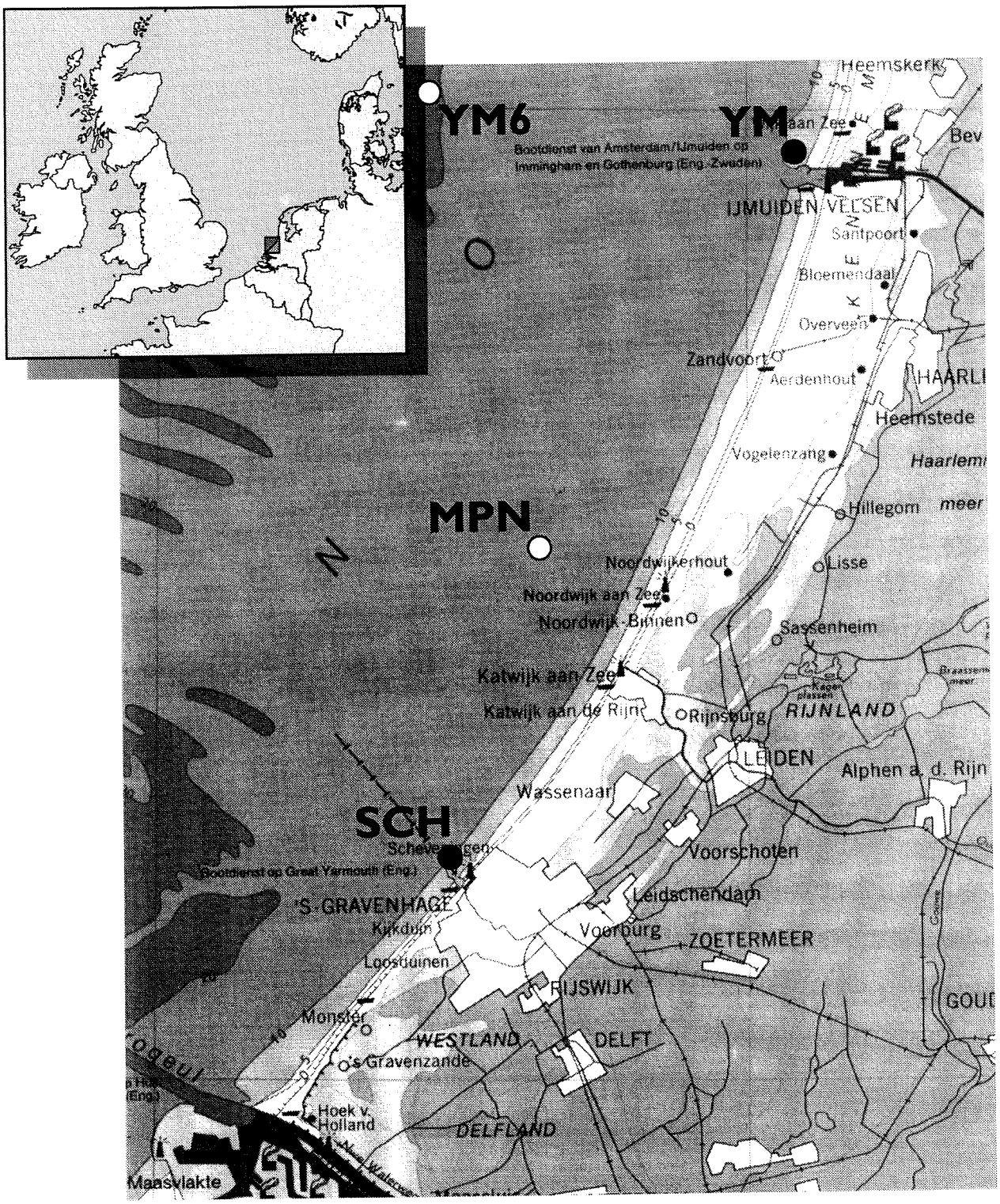

- Coastal station
- Offshore station

Figure A.1 Map of Central Dutch Coast

Appendix B

Measurement techniques of Noordwijk'95 field experiments

B Measurement techniques of Noordwijk'95 field experiments

One of the subgoals of this project has been formulated as 'experience the dynamic behaviour of a coastal system by executing field experiments during a limited period of time'. The results of two periods of field experiments along the beach are described in Chapter 3. In this appendix a short note will be dedicated to the equipment used at the Noordwijk site and if possible, the order of accuracy that could be expected. Successively GPS, the echosound, the waterlevel and the frame are treated.

B.1 Global Positioning System (GPS)

In addition to conventional methods (see below) nowadays, GPS may be used when surveying the beach profile. During the Noordwijk field experiments of May 1995 this has been done using equipment of the Oregon State University, Oregon, USA. Some notes with regard to the application of this technique will be mentioned here.

A short note on history and the characteristics of GPS

The immediate predecessor of today's modern positioning system is the Navy Navigational Satellite System (NNSS), also called TRANSIT system. This system composed seven satellites orbiting at altitudes of about 1100 km with nearly circular polar orbits. Positioning was based on the registration of Doppler shifts of radio signals, transmitted by one TRANSIT satellite. The system suffered from three major shortcomings, viz. the moderate availability of satellites (only 20 times per day), the length of one survey (approximately 15 minutes) and the relatively low navigation accuracy (100 - 200 m).

It is because of these shortcomings that the US Department of Defense initiated in 1973 to develop a new spaceborne positioning system, eventually leading to the Global Positioning System (GPS). The main goal was to develop a system that enables a user to determine one's position 24 hours per day, anywhere on earth, with an improved accuracy with regard to the TRANSIT system. Since the Department of Defence was the initiator of GPS the primary goals were military ones. Only afterwards civil applications have been developed, though their best accuracy is restricted by the owner of the system.

The essential difference between GPS and TRANSIT is that GPS determines distances to several different satellites at a certain moment, instead of 'following' one satellite during a certain period of time. In order to do so 21 satellites are present at 20 km altitude, evenly spaced in circular 12-hour orbits inclined 55° to the equatorial plane. Application of such a technique puts some severe demands to the specifications of the equipment used, for instance with respect to the time registration. As the position of the satellites in question has to be determined at exactly the same moment, all satellites are equipped with extremely high accuracy clocks (though the receiver disposes an inexpensive crystal clock).

Surveying the coordinates of a location on earth - in fact - means the determination of four unknown: (x,y,z,t). Solving for four unknown requires four equations, i.e. four measured distances in case of GPS. Measuring also a fifth distance allows a least squares solution of the problem. The best accuracy depends on the accuracy with which each satellite position is known, the accuracy of the distance measurement and the geometry of the satellites

involved. The latter can be characterized by the Position Dilution Of Precision (PDOP) parameter, which is a (theoretically computed) factor describing the 'quality' of the geometry of the visible satellites: for PDOP > 6 survey is possible. In this way GPS-based positioning is possible 24 hours per day with an accuracy of 100 - 150 m in case of non military applications, which is mainly limited by owner's restrictions, though.

Of course, for beach survey (and a lot of other applications within the field of hydraulic engineering like dredging) the 'allowed' accuracy is not good enough. The solution has been found in a system called 'Differential GPS'. This technique has also been used in Noordwijk. A second (stationary) GPS receiver is placed on a location with exactly known coordinates. At the moment the mobile receiver determines its position relative to the satellites the stationary receiver does the same, which yields values that are slightly different from its known coordinates. These differences are transmitted as a correction signal to the mobile receiver, where the same correction is applied. In this way accuracies up to centimetres can be reached, in case of short distances (several kilometres) between the two receivers.

Finally distinction should be made between static survey and kinematic survey. Static survey is used to locate one point, using two fixed receivers. On the other hand, in case of kinematic survey one receiver is fixed and one is moving. Coordinates of the moving receiver are determined once every meter. In this way whole areas can be mapped quite easily with a high resolution of survey points, which explains the application of GPS in case of beach survey.

Mapping the Noordwijk beach using GPS

During the Noordwijk Field Campaign the stationary receiver was placed up on the roof of Grand Hotel 'Huis ter Duin', next to the ARGUS cameras. Because of the probability of damage during storms it had to set up again every day. The coordinates of this position were exactly known, relative to the ARGUS axis system (see Chapter 3). Each time, before starting a new survey, the system had to be initialized. Doing so the mother station (=fixed receiver) picked one satellite and collected 3 others around it. The first satellite continues to be the central satellite, unless a new initialization is performed. Furthermore the (known) position of beach pole 82 was verified (tolerance: 2 cm) at the beginning of every day, in order to be sure the system works well.

A survey had to be planned carefully, because of the restrictions associated with the system. First of all, 2 (predictable) conditions have to be fulfilled: a survey has to be performed at low water (yielding a tidal window) and the configuration of the satellites should meet the accuracy demands, i.e. PDOP > 6 (yielding a PDOP window). Figure B.1 gives an example of such a PDOP window:

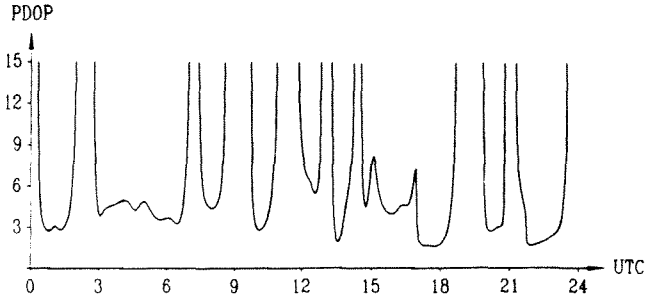

Figure B.1 Example of PDOP window

By matching these two windows the period of survey can be planned. Apart from this the availability of at least 5 satellites is required. The latter condition sometimes caused some problems when satellites disappeared behind the dunes, a hotel or other objects. Every time this happened the system had to be re-initialized, after which survey could restart.

The coordinates of all Ground Control Points (see Chapter 2) have been obtained from static surveying, kinematic surveying along 50 m spaced transects has been applied in order to gain bathymetries, comprising the dry beach, the runnel and the (dry) swash bar. The roving receiver was placed on a small cart at known height relative to the ground. All data were stored on the hard disk of a lap top computer situated in a back pack. Data comprised up to a maximum of 3600 surveyed points and comment lines, explaining the meaning of pairs of surveyed coordinates. Finally all survey commands could be entered from the keyboard of a small box linked with the lap top, which also disposed a lcd screen for communication and visualization of satellite positions. Afterwards the collected data had to be processed and elaborated by means of a spread sheet program or numerical mathematical program, in order to get two- or three-dimensional impressions of the surveyed bathymetry.

B.2 The echosound

A commonly used piece of equipment to determine water depths is the echosound. The method is based on the transmission of a sound wave, generated by a so called transducer, which is reflected by the bottom. The time between transmission and reception of the signal is measured, from which the water depth is computed (knowing the propagation speed of the signal and taking into account a factor 2 as the distance transducer-bottom has been travelled twice). The penetration depth in the bottom or a mud layer strongly depends on the frequency of the transmitted signal, the lower frequencies penetrating deeper. So even a sub bottom profile can be surveyed. Results are plotted immediately on a roll of paper, on which also marks can be plotted as a 'reminder' of a certain position.

Several method related problems arise when executing an echosounding. First of all a certain kind of positioning system has to be available. Ideally a GPS system would be present. If not, the position of the vessel can be determined by synchronously measuring the 2 base angles of the triangle enclosed by the vessel and 2 water levels on the beach, with accurately known coordinates. This method requires a good communication system between 'beachcrew' and 'vesselcrew'. In case of the Noordwijk Campaign the distance offshore has been determined with a so called 'topoliet'. This instrument consists of a counter and a very thin rope, which has to be fixed at the beach. While sailing in seaward direction the distance relative to this beach location can be determined from the counter. By putting reference marks on the paper roll every 50 m an indication of bathymetry (x,z) is obtained. It should be mentioned that this technique may be affected by currents and winds, as well as the capability of the steersman to sail a transect perpendicular to the coast.

During the Noordwijk echo sounding in the morning hours of October 6, 1995, additional positioning difficulties arose when crossing the nearshore surfzone at low water turned out to be impossible, given the offshore wind (force SEE 3) and hence relatively steep breakers. For this reason, an alternative approach has been applied, which will be explained with the help of Figure B.2:

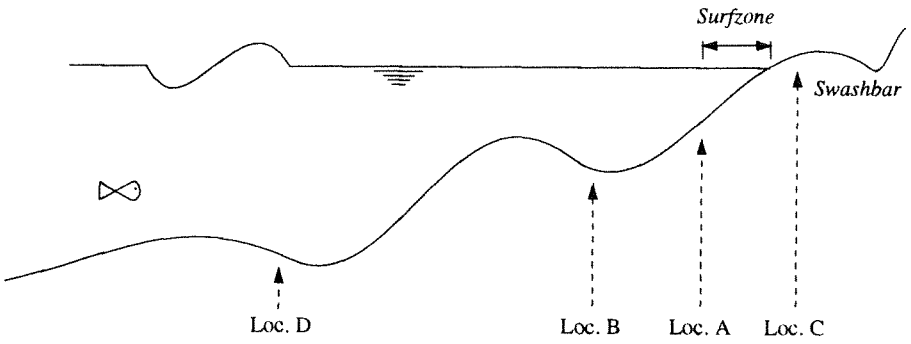

Figure B.2 Overview of site of echosounding, Noordwijk, 95/10/06, transect 8115

The echosounding started immediately seaward of the nearshore surfzone at location A, by passing the topoliet rope to a person X standing in the water, while sailing by. By the time that the vessel was at location B person X started to walk to a predetermined location C at the swashbar (which will serve as reference point), a movement that could clearly be identified from the smaller time gap between equal-distant marks on the paper roll (assuming a constant vessel speed). At the moment person X reaches the reference point C the vessel is at location D. At roughly the same time as this echosounding a water levelled profile is determined starting at the beach, crossing the swashbar and overlapping part of the echosounded profile. By comparing the depths at the seaward face of the swash bar for each of these two profiles location A can be determined. Knowing furthermore the location C of the reference at the swash bar up to which the distance to the vessel is determined, as well as position D at the end of 'double movement', then a position-correction for survey data obtained during the period of time that the rope 'moved' into two directions can be executed. In practice, this has been done by means of a linear stretching of the surveyed profile. Furthermore it is reasonable to assume that the third bar, which has also been surveyed in June 1995 by regular Rijkswaterstaat echosoundings, did not change. In order to fit the October survey to the preceding a shift ($\Delta x, \Delta z$) is necessary such that it still fits to the waterleveled bathymetry. It can be explained from the existence of a time gap between the reception of the rope by person X and the start of survey (while still sailing), combined to a possible error due to the vessel sailing along a line slightly oblique to the shoreline. Indeed, the method applied in case of Noordwijk 1995 is quite cumbersome and sensible to the introduction of errors, however, given the wave and tidal conditions and the time pressure (October 6 being the last day of the field experiments) alternatives could not be found.

During the same Noordwijk field experiments the echosound has been calibrated by measuring the water depth in the (shallow) trough: an echosound registration of 0.7 m matched a water depth of 0.45 +/- 0.05 m. More generally, an echosound can be calibrated by means of a so called 'barcheck'. A plate is suspended from the vessel at a known depth below the transducer. The transducer depth is set by positioning the plate at small depth below the vessel, say 0.5 - 1 m. At this small depth the influence of the propagation speed v of the signal does not play any roll, thus the transducer depth can be adjusted until the plotted depth matches the actual depth. Next the plate is positioned at a large depth relative to the vessel. If the registration is incorrect the propagation speed v can be tuned in order to get a right measurement. By stepwise lifting the plate and simultaneously checking the corresponding measurements the functioning is validated. However, due to inhomegenities of the seawater (temperature, salt content) and hence varying propagation speeds, the measurements will never be exactly right. Furthermore the bathymetry is determined with

regard to the tidal level and hence, errors made while predicting the astronomical tidal level or while measuring it with a tidal gauge, will appear in the final result.

Apart from these inaccuracies some factors related to the movements of the vessel exist, that negatively affect the measurement:

- Rolling of the vessel causes the echosound to record a bottom segment which is not immediately under the vessel but some distance further away. In this way the depth will be overestimated.
- Short waves will cause a alternating, vertical movement of a small vessel. Due to the mass of such a vessel, it will tend to fall a little bit too deep into the trough following after a wave crest. These wave initiated movements of the vessel can be seen on the paper roll. So, by simply averaging out these movements, the water depth will be underestimated.
- The skills of the person sailing the ship will strongly affect the resulting ship movements.

Under ideal conditions (wave conditions, equipment and crew) the error δ can be determined from a rule of thumb, which is valid for depths d up to 30 m:

$$\delta = 0.2 + 0.006 \cdot d \quad (m) \tag{B.1}$$

This is the best accuracy possible. Given the situation at Noordwijk (small vessel, unskilled crew, moderate wave conditions, a relatively inaccurate calibration and serious positioning difficulties) an accuracy of 0.5 - 0.7 m may be expected.

B.3 The waterlevel

The position (x,y,z) of a certain object can be determined by using a waterlevel. For doing so one needs 2 persons, a rod (length 3-4 m) with a centimetre scaling printed on it and a waterlevel. The waterlevel has to be placed at a location with well known coordinates. Next the rod is placed on the object or location, which coordinates are wanted to be known. For this specific position, the distance and height relative to the waterlevel and the angle relative to a certain fixed line can be determined. By making use of some simple geometrical relationships (eg. sine and cosine rule) the position (x,y,z) of the rod can be determined.

The waterlevels used at Noordwijk were of the conventional type. Looking through the waterlevel at the rod one could identify three threads projected at the centimetre scaling of the rod. The middle thread determined the height of the base point of the rod relative to the horizontal plane through the waterlevel, while the difference between the upper and the lower thread, multiplied by a factor 100, determines the distance between rod and camera. Theoretically in this way distances up to 300 m can be measured when using a 3 m rod, however, in practice, it often happens that either the upper or the lower thread falls outside the reach of the rod. In those cases it is still possible to determine the distance, although one should be very carefully as the possibility to check your observations - the distance between upper and middle thread being equal to that between middle and lower thread - has been lost.

Within the region of the larger distances, estimating the position of the threads on the rod with an accuracy of 1 cm is possible. This yields an accuracy of 1 cm in vertical sense and 2 m in horizontal sense, as distance measurements require two determinations. Furthermore the plane through the waterlevel may have some small deviation relative to an exactly horizontal plane. This affects just the height measurement. For a deviation of 0.1° the additional error is about 0.17% of the distance between waterlevel and rod, or 0.17 cm per 100 m. When determining the rod's position by making use of the waterlevel's graduated arc, angles can be determined with an accuracy of approximately 0.5 german degree = 0.45°. Generally one needs two angle measurements, thus yielding an horizontal error of 1.6% of the distance between rod and waterlevel. Summarizing, vertical measurements are possible with an accuracy of the order of a centimetre, while distance and horizontal measurements include errors of the order of meters.

The 'theoretical' considerations of the preceding paragraph assume a rod that can easily be held up in the same position. However, standing in the surfzone this assumption is strongly violated. Besides this, inaccuracy is introduced by the fact that the sea bottom is not as smooth (think of small ripples, as well as large ones) as we would like it to be when using a sample distance of about 10 m. Finally the breaking wave action and the oscillating water movement, especially in shallow water of several decimeters, cause a scour hole around the foot of the rod and hence, the rod sinks away. The combined effect of these three phenomena cause inaccuracies of the order of 20 to 30 cm in vertical sense, for which the measurements partly can be corrected by levelling a wet profile twice (there and back) instead of one time.

B.4 The frame measuring wave heights and water velocities

During the second Noordwijk period two frames were available for the determination of wave height and current velocities in relatively shallow water. They could be placed into the trough or at the inner bar at low tide and in general they were pulled out during the next low tide, as their batteries had to be charged. Both frames were equipped with an EMF, suitable for the measurement of current velocities in two (perpendicular) directions, and a pressure meter, for the measurement of wave heights. Every hour measurements continued for 40 minutes with a frequency of 2 Hz, i.e. 2 measurements per second. In this way one so called 'burst' was generated every hour. Both instruments were calibrated in the laboratory of Physical Geography, yielding linear relationships between millivolts (recorded by the instruments) and millibars c.q. meters per second, see figure B.3. In the following only the wave height measurements will be taken into account.

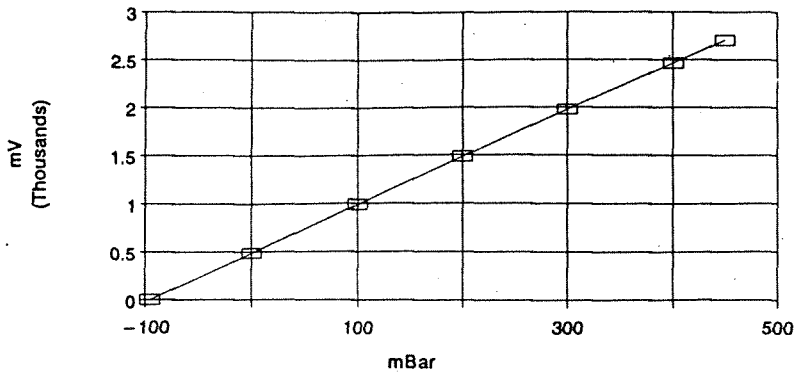

Figure B.3 Calibration line of wave height meter

The data collected by the pressure meter while standing in the sea were stored in the data logger in the so called Final Storage Format, a compact format where one value occupies only two bytes. These data were read out of the data logger and stored on the hard disk of a pc in a binary format, where one value comprises four bytes and which allow calculations. With the help of some software called 'framesplit' it was possible to split up the data per burst and have a look at the collected data for every individual burst. In order to deduce 'practical information' from these time sequences, software called 'AUKE PC' has been used. This program derived parameters like H_{sig} and T_{sig} from the time series thus characterizing the wave climate during the 40 minutes burst, while making use of the (lab determined) linear relation between millivolts and millibars. When calibrated relative to the air pressure, even the local water depth could be determined from the time series.

When the position of the frame within a certain transect is known, as well as the bathymetry of this specific transect, the obtained wave height data can be used in order to validate the reliability of the simulation of the hydrodynamic processes with the wave decay model UNIBEST-TC.

Appendix C

Correlations between image intensities and breaking related parameters

Correlations between image intensities and breaking related parameters

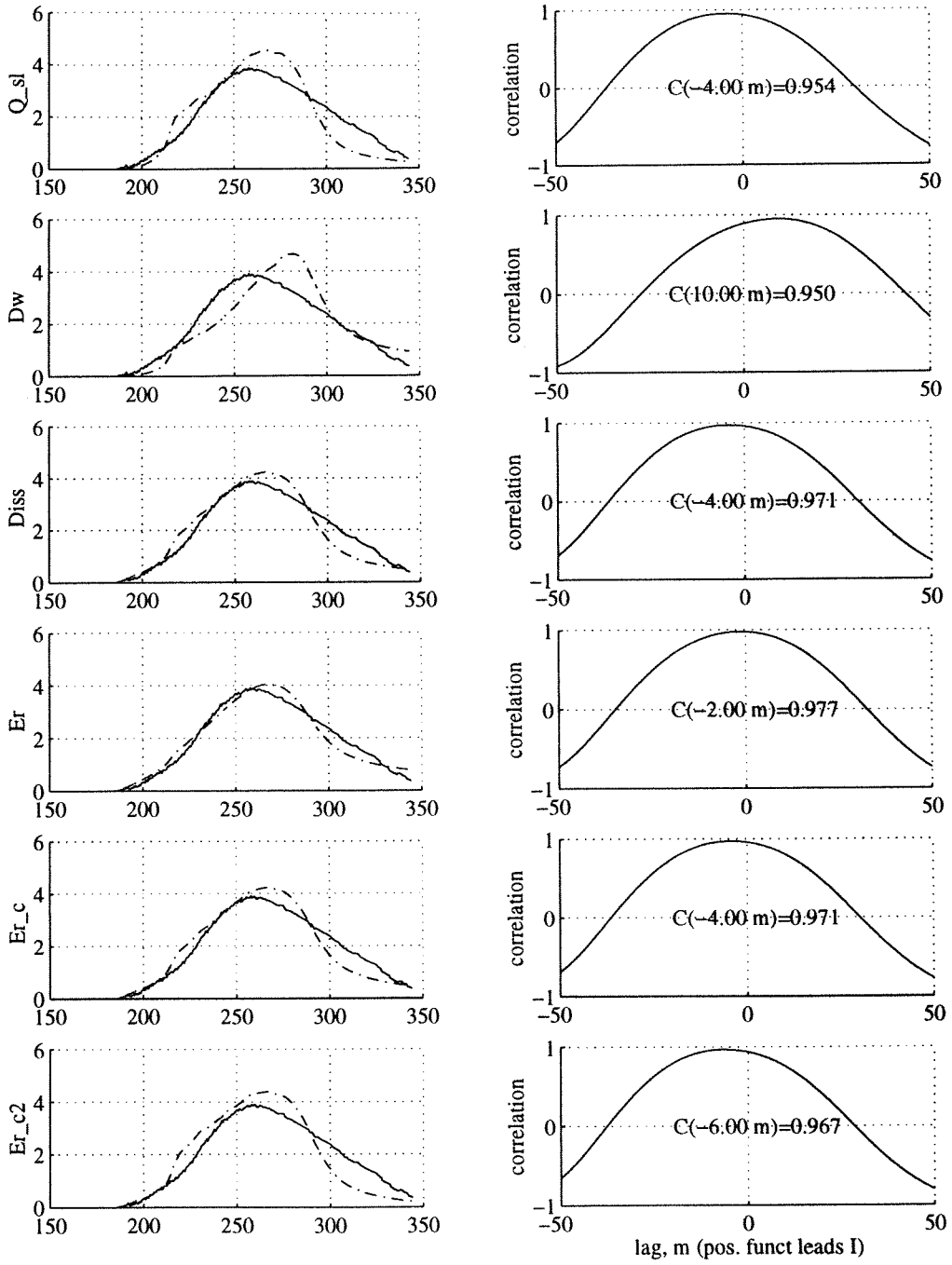

Figure C.1 Correlations between image intensities and breaking related parameters

Appendix D

Table H_{max}/h vs h/gT^2

Maximum wave height, based on stream function theory

The table below, obtained from *Williams* [1985], gives the maximum wave height H_{max} at a depth h, as a function of the ratio $h/(g \cdot T^2)$. It has been used in order to generate a reference wave height H_{max} for the actual boundary wave height H_{sig}, while determining the value of the scale factor SF.

$T\sqrt{(g/h)}$	$h/(g \cdot T^2)$	H_{max}/h
∞	0	0.833
25.6	0.00152	0.786
20.8	0.00231	0.775
17.6	0.00323	0.765
15.3	0.00428	0.756
13.5	0.00545	0.747
12.2	0.00671	0.737
11.1	0.00806	0.728
9.53	0.01100	0.709
8.39	0.01419	0.689
7.55	0.01756	0.668
6.89	0.02107	0.646
6.37	0.02466	0.623
5.59	0.03197	0.576
5.05	0.03926	0.530
4.64	0.04642	0.487
4.33	0.05339	0.447
4.08	0.06018	0.412
3.62	0.07648	0.340

Table D.1 H_{max}/h as a function of $h/(g\Pi T^2)$

All values of $h/(g \cdot T^2)$ met into MONIMORPH are found in the upper half of the table.

Appendix E

Alternative scaling techniques

E.1 Alternative ways to determine the scaling parameters (I_{base}, r, SF)
E.2 More than three tuning parameters
E.3 Transform image intensities based on optical considerations
E.4 Application of a neural network

Alternative techniques to scale image intensities

The MONIMORPH scaling technique, based on three scaling parameters (r, I_{base}, SF), works reasonably well as a first approach. Nevertheless, situations occur where a mismatch between scaled intensity profile and E_r/c^2 curve has been observed visually. Moreover, the determination of the correct value of SF produces some difficulties, in particular in case of mild wave conditions. Because of this, some alternative approaches will be mentioned in this appendix.

E.1 Alternative ways to determine the scaling parameters (I_{base}, r, SF)

In cases of known bathymetry, the intensity profile of a single image can be related to an optimal combination (SF,r), both determined by minimizing the least squares error between a scaled intensity profile and a 'correct', UNIBEST generated E_r/c^2 curve. The result of this two dimensional optimization is a set of (SF,r) pairs, that equals the number of images of one calibration day. Again the optimized scalefactors are related to the dimensionless wave parameter H_{sig}/H_{max}, while the optimal gradient term r might be related to time varying parameters like the angle of incidence of sunlight and other atmospherical phenomena. Although this approach yields a good fit of field intensity data to UNIBEST data it cannot be applied in MONIMORPH as the latter relation between r and physics has not been found yet.

Another solution would be the derivation of an expression for $\psi_I(x)$ from theoretical, optical considerations. This expression may depend on the way the ARGUS site is illuminated (atmospherical conditions), reflection patterns varying with the position of the sun, disturbing influences in the neighbourhood of the screen boundaries etc. For the time being however, these aspects have not been studied yet.

E.2 More than three tuning parameters

Two discrepancies are clearly present in a number of cases when applying the three parameter (I_{base}, r, SF) scaling method, viz. a) a spatial lag between the two profiles (one profile shifted seaward or shoreward relative to the other) and b) a different shape, one being more peaked or flattened than the other. A lag parameter δ and a shape parameter α could be defined in these cases as the tuning parameters. In that case the transferfunction F would read

$$F[I_{raw}(x)] = SF\cdot([I_{raw}(x-\delta) - \psi_I(x)] - I_b)^{\alpha} \qquad \text{(B.1)}$$

Using a complicated expression like (B.1) raises the question whether the application of five tuning parameters does not reduce the reliability too much, given the fact that it may be awkward to relate all these different parameters to a physical property.

E.3 Transform image intensities based on optical considerations

Observed image intensities can also be treated from an optical point of view, which is an approach completely different from the preceding. One can think of a whole range of problems that may have to be solved, like

- Is reflection the primary mechanism that makes light reach the camera lens, and what is the effect of upwelling radiation;
- In what way are observed radiation signals transformed into image intensities;
- How should camera related properties (auto iris, fixed focal length) be taken into account?;
- What is the effect of varying locations of intensity sampling within the field of view of the camera;
- How can disturbing influences be taken into account, atmospherical (clouds, fog, sun glitter), as well as at the water surface (residual foam).

Within some other fields of hydraulic engineering optical techniques have been applied, eg. in case of indirect measurement of wave heights, the so called Stilwell method. This method assumes that variations in measured light intensity at a certain place are caused by changes in wave slope. The amount of light measured by the camera depends on the angle to the water surface. Deviations from this angle-dependent relation are a measure for illumination inhomogeneties, caused by changing reflected radiation as a consequence of changing wave slopes (*Hesselmans* [1990]). Location dependent reflection relations may be derived from studies like this. A second example is the observation of the phenomenon whitecapping. Whitecapping, i.e. the breaking of waves at deep water due the exceeding of a certain maximum ratio waveheight/wavelength, has been studied from optical field observations (eg. *Snyder et all.* [1983]). Phenomena analogical to what can be seen on ARGUS images (high intensities denoting breaking, disturbance from sun glitter, etc) will be met. Based on experiences gained during these types of experiments (and associated literature) the scaling problem regarding ARGUS intensity data may be approached.

E.4 Application of a neural network

If the methods described above do not produce valuable results, simply because of the complications involved in describing exactly the path from light signal to pixel intensity and to include all disturbing effects into the scaling model, a neural network might be a promising alternative. A neural network is an information-processing system modeled on the structure of the human brain. Its biggest merit is its ability to deal with fuzzy information whose interrelation is ambiguous or whose functional relation is not clear (*Mase et all.* [1995]). The type of network applied most frequently are the so called Multi Layer Perceptrons. These consist of one input layer, one output layer and a variable number of interlayers, the so called 'hidden layers'. Every layer contains a variable number of elements called 'units', which are the basic constituents of the neural network - see figure B.1. Dataflow through the model takes place in one direction, without any recursive steps between layers.

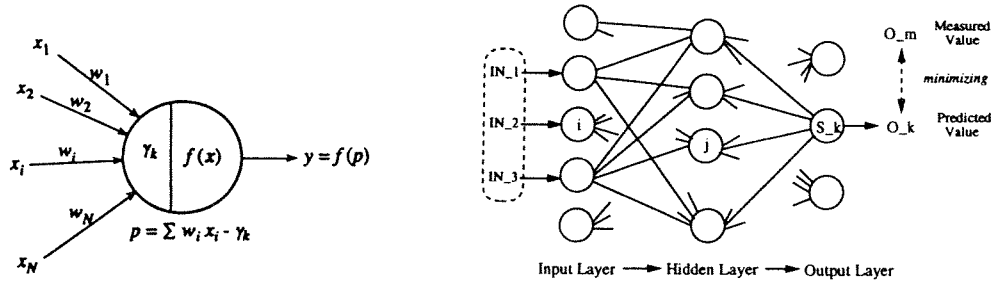

Figure E.1 Neural Network and basic constituent, a unit

Units are linked to each other by means of user defined relations. A model unit usually has many input signals and only one output signal. Input signals x_i from the incoming connections are summed up by being multiplied with the weights w_i of the connections and then the threshold value γ_k is subtracted from the summed signal. The modified signal S_k is fed into the unit where it is transformed according to a nonlinear transfer function f(x). A common transfer function is the sigmoid function, expressed by

$$f(x) = \frac{1}{1+\exp\left(\frac{-2x}{u_0}\right)} = \tfrac{1}{2}\left[1+\tanh\left(\frac{x}{u_0}\right)\right] \qquad \text{(B.2)}$$

where u_0 is a constant. The sigmoid function has as a characteristic that its differential can be formulated in terms of the sigmoid function itself:

$$f'(x) = \frac{2}{u_0} \cdot f(x)[1-f(x)] \qquad \text{(B.3)}$$

In fact, the process of defining relevant input parameters, number of inter-layers and elements per layer, desired output and relations between cells is the crucial part of the design process of a neural network. Definitions should be as compact as possible, without of course, missing any relevant properties.

Once the network has been designed it has to be trained (or calibrated). This means that an optimal set of weighting factors $w_{1..n}$ and threshold values $\gamma_{1..n}$ is derived by running the model for a dataset of which the desired output is known beforehand. For visualization, imagine a complicated plan of intersecting roads all connecting the input layer and the output layer. At any intersection it has to be decided how to transmit the information. Facilities along the roads, in casu the weighting factors and the threshold values, guide the information into the right direction. Different choices of $w_{1..n}$ and $\gamma_{1..n}$ will yield different output signals for a given training set of input patterns, and hence a different degree of agreement to the desired output signals. Once the weighting factors are fixed every different input pattern will be guided along a different 'path' through the model ('layers') and hence yield different output. The values of $w_{1..n}$ and $\gamma_{1..n}$ are determined by means of a gradient method. Starting with an arbitrary set of weights and thresholds the sum E_p of the squared differences between

output signal and desired signal is computed. Next the weights and thresholds are changed systematically, in proportion to the partial derivatives $\partial E_p/\partial w_i$ and $\partial E_p/\partial S_k$ respectively. The set of equations to do this, in case of the training procedure called 'back propagation', is given by *Mase et al.* [1995].

Minimizing the error parameter E_p by running the model a certain number of learning iterations will yield the final set of weights and thresholds. In general, a larger number of hidden units or a larger number of training iterations will result into a higher correlation between output signal and desired signal. However, if the network is applied to data from outside the training data set, then the correlation turns out to decrease above a certain number of training iterations. This phenomenon is called 'overtraining': the network is so fit to the structure of the input patterns of the training data set that it fits less well to the other input patters, with increasing number of training iterations. From these considerations a decision has to be made regarding the best number of training iterations. The number of hidden units should be chosen in such a way that a certain minimum correlation between output signal and desired signal is 'guaranteed', while too many hidden units will complicate the model unnecessarily. In these considerations, statements like 'too many units' should always be interpreted as 'relative to the complexity of the input pattern'. Furthermore, one should always be careful when applying the network to situations that are beyond the limitations of the training dataset, as the network has just been trained to 'recognize' patterns that would fit within the extremes of this base data set.

In case of the scaling routine for ARGUS intensities, one could think of selecting a number of days with known bathymetry. As UNIBEST-TC can be run, the desired output is known. Furthermore, intensity profiles can be obtained from the corresponding images. Once again it is stressed that this dataset should enclose all different kinds of wave- and atmospherical conditions. Now, relevant parameters, both hydrodynamical, atmospherical and optical, have to be selected, and relations have to be established. It is however outside the scope of this report to produce a first outline of a possible neural network. The opportunities in this respect should be investigated in future.

Appendix F

Subsequent operations when applying the inverse model

Subsequent operations when applying the inverse model

The inverse model MONIMORPH has been set up such, that it can be applied to any ARGUS site in the world, apart from - of course - some changing, site related parameters. In- and output data involved are specified by means of a date and, if necessary, a transect identifier. The following directory structure has been adopted:

/site_data/survey/
/site_data/waves/
/site_data/tides/
/site_data/images/
/site_data/geom/
/site_data/uni_run/
/site_data/uni_res/
/site_data/nameslong/

The directory 'survey' contains surveyed bathymetry data in terms of local ARGUS coordinates, saved as bath_transect_yymmdd, e.g bath_1100_941011. The directory 'waves' contains all necessary wave data, stored in three files called Hsig_yymmdd, Tsig_yymmdd and angle_yymmdd, while files tide_yymmdd can be found in the directory 'tides'. Images of -gif format are collected in the directory 'images' and the adjacent geometries are in the directory 'geom', being .bin files in case of Duck and a Matlab file in case of Noordwijk. Input files necessary to run UNIBEST are gathered in the directory 'uni_run', comprising site###.dat files, ##_transect.bot bathymetry files and ##yymmdd.rvw files giving the boundary conditions. Finally the directory 'nameslong' holds text files 'nameslong_yymmdd', containing the names of all ARGUS images available at one day.

Up to now three separated operations can be distinguished while running the model, viz. the deduction of intensity values from images, the running of UNIBEST in order to provide boundary conditions and the actual inverse computation based on image intensities. The following scheme summarizes the data flow through the model and the required input to any routine.

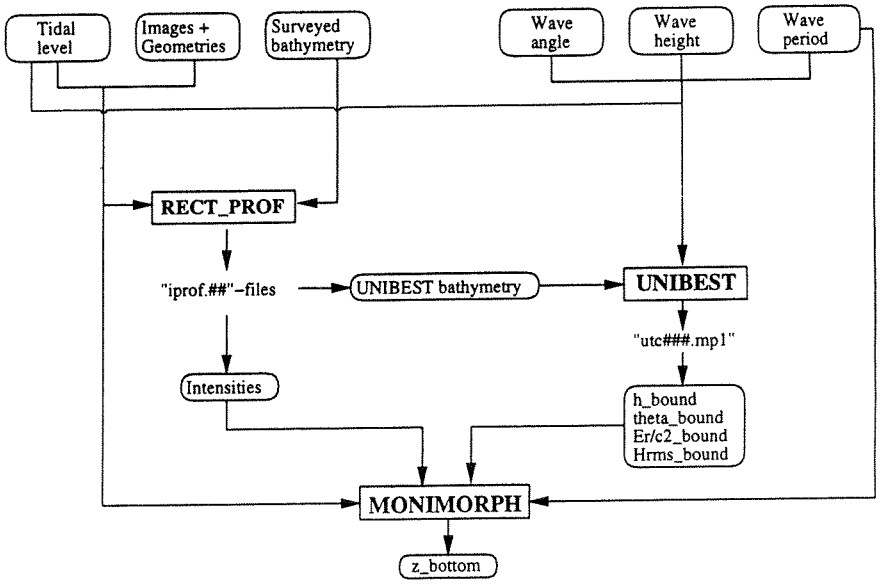

Figure F.1 Data flow through inverse model

A one day run is started by calling a MATLAB routine 'rect_prof.m' which stands for rectify_profile. It needs images (+ adjacent geometry data), tidal levels and a surveyed bathymetry as input. Intensity data are derived from the images, along a rectified profile corresponding to the surveyed (x,y) coordinates and the momentary tidal level. The output consists of an ascii-file called '/site_data/intens/iprof.site.transect.Month.day.hr', containing 5 columns [x y z Int tide].

Thus generated iprof-files act as input to the MONIMORPH model, but are also used in order to generate an UNIBEST bathymetry (for which an awk routine has been written by Nathaniel Plant). Having composed furthermore a site###.dat definition file and a ##yymmdd.rvw file containing wave and tidal data, UNIBEST can be run generating a utc###.mp1 file comprising the cross-shore variation of some user defined output parameters. Applying again an awk-script, the utc###.mp1 file is split up into files utc###.mp1.parameter (where 'parameter' can be Er, Hrms, c or z), who can be read into MONIMORPH.

Finally, the MATLAB routine monimorph.m is run, which generates its boundary conditions from the files 'uni_res/utc###.mp1.parameter' and 'intens/iprof.site.transect.Month.day.hr', finally yielding a weighted estimate of bathymetry in the way described in Section 6.4.

The computations described above have been performed for the Duck bathymetry of October 11, transect 1100. In order to illustrate the different steps mentioned above, some subresults are reported in the following figures:

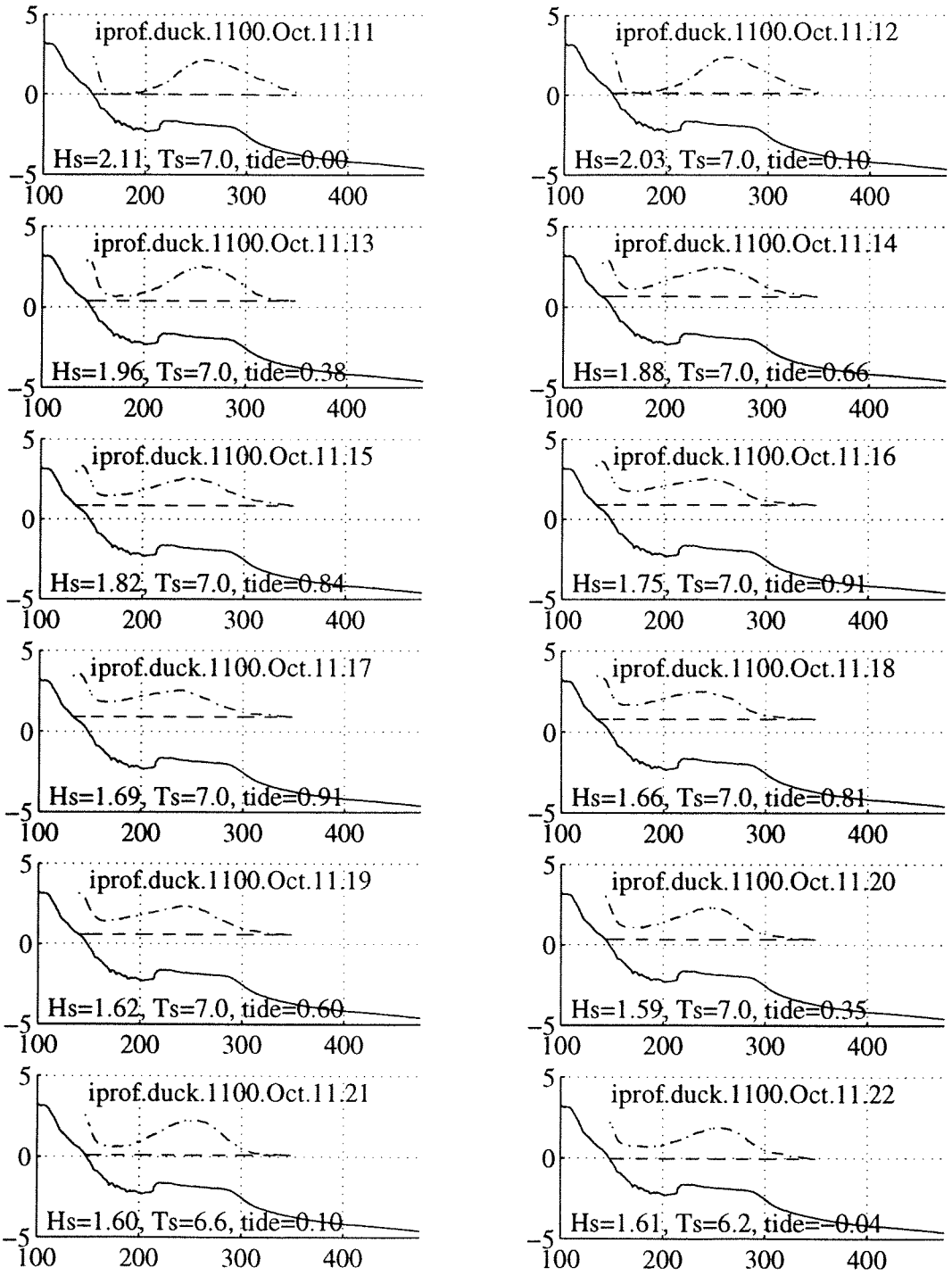

Figure F.2 Intensity profiles as obtained from time exposure images

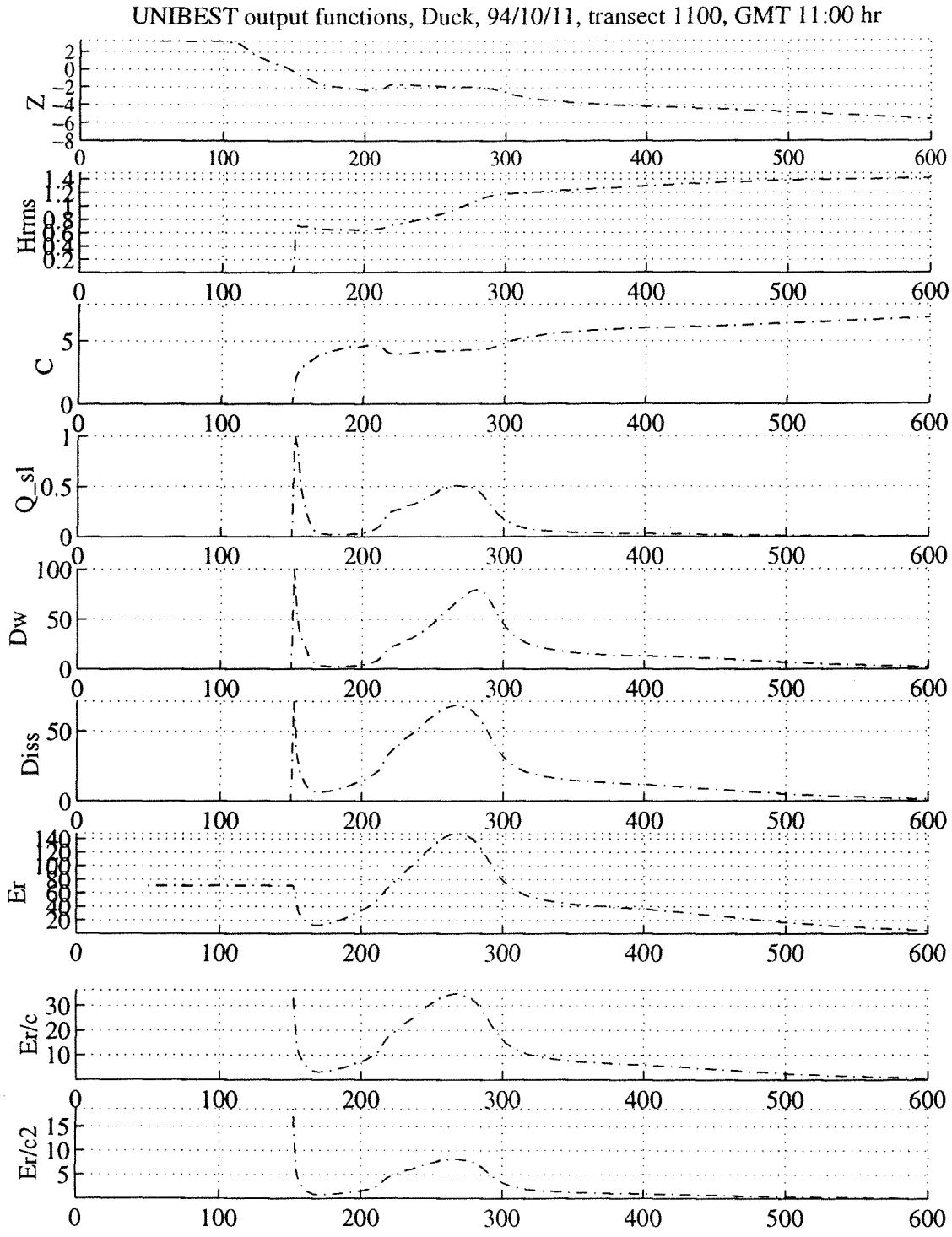

Figure F.3 Results of wave decay modelling according to UNIBEST-TC

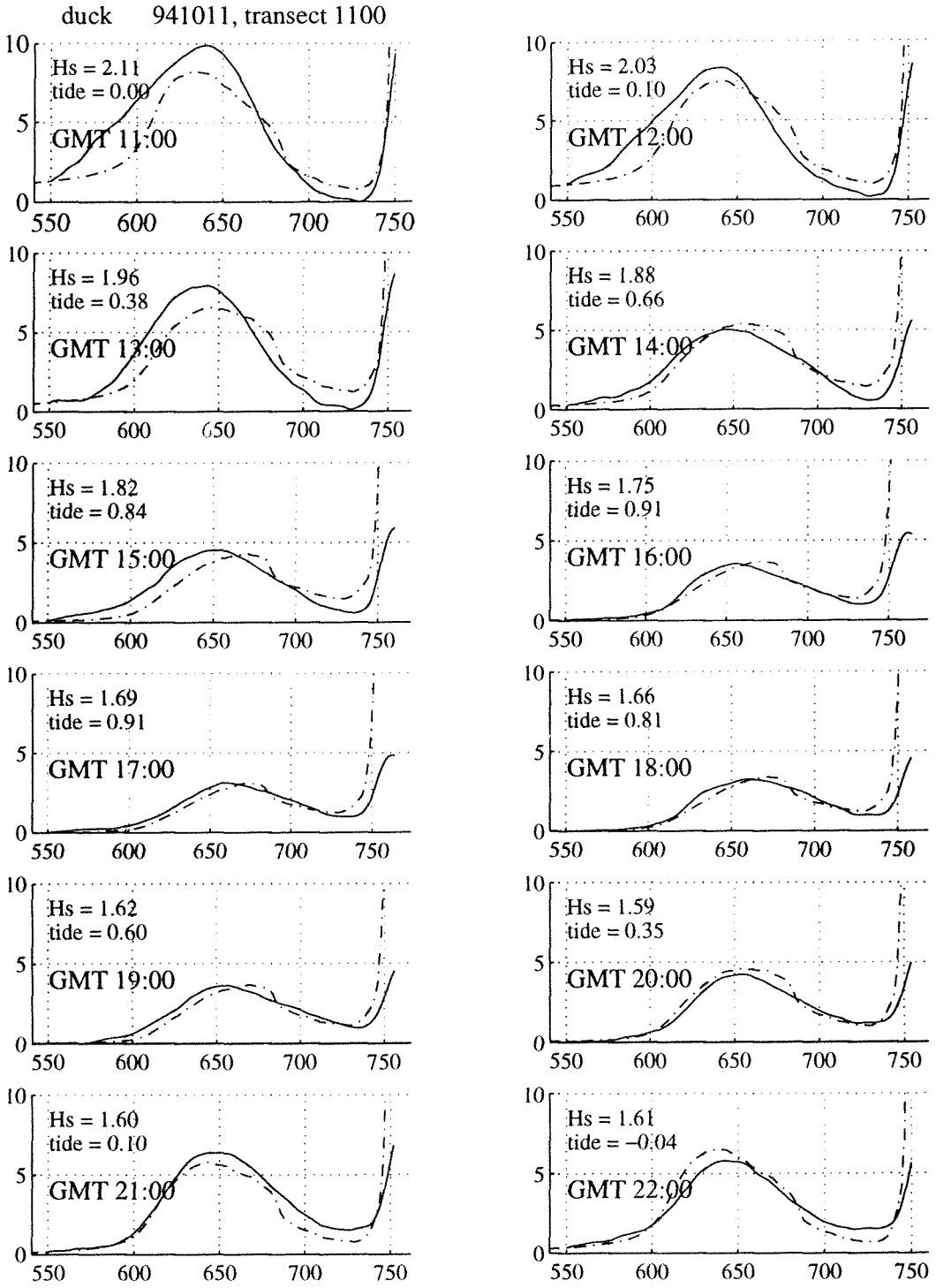

Figure F.4 Comparison of scaled intensities (solid line) to E_r/c^2 profiles (dashed line)

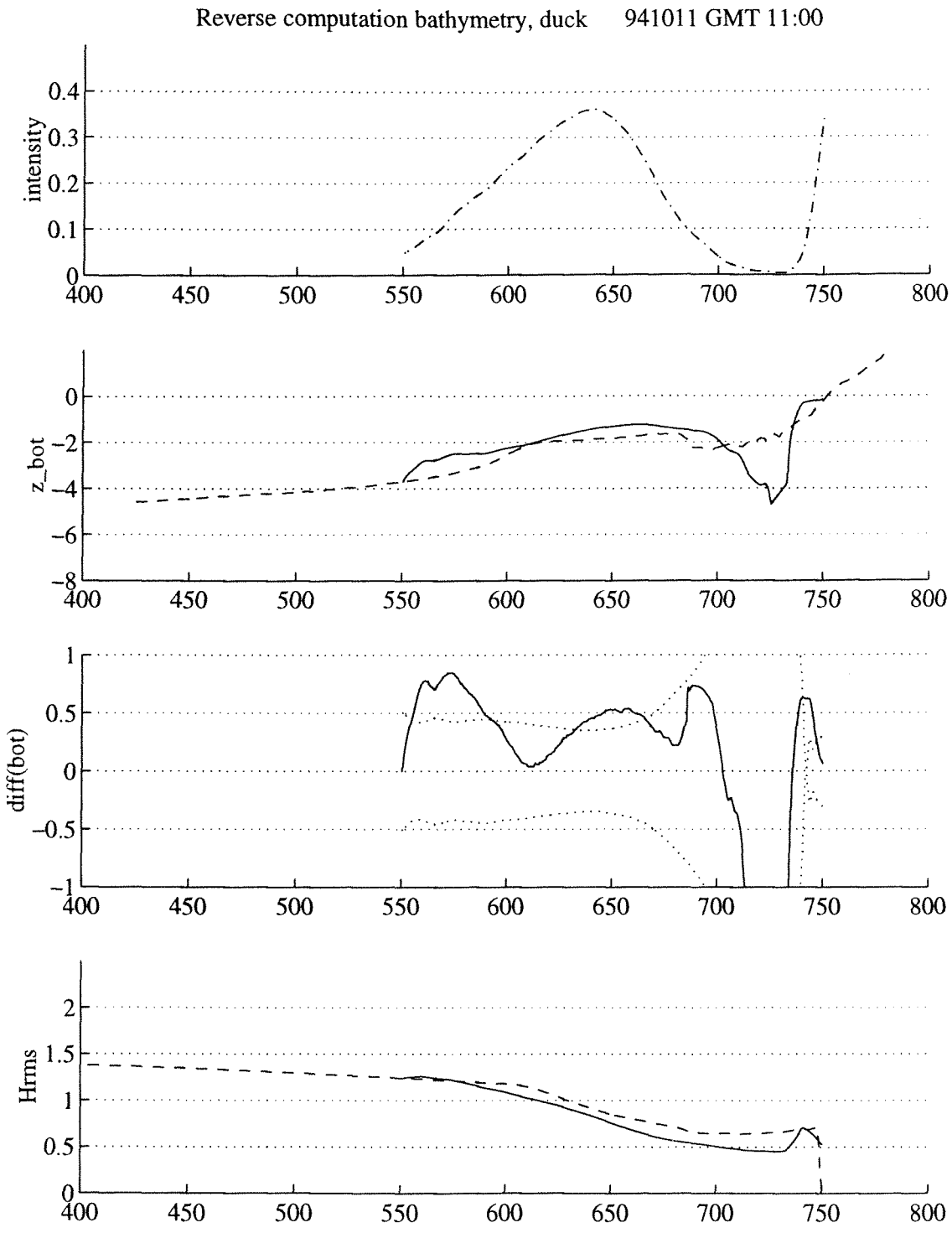

Figure F.5 Estimate of bathymetry based on one single image (GMT 11:00 hr)

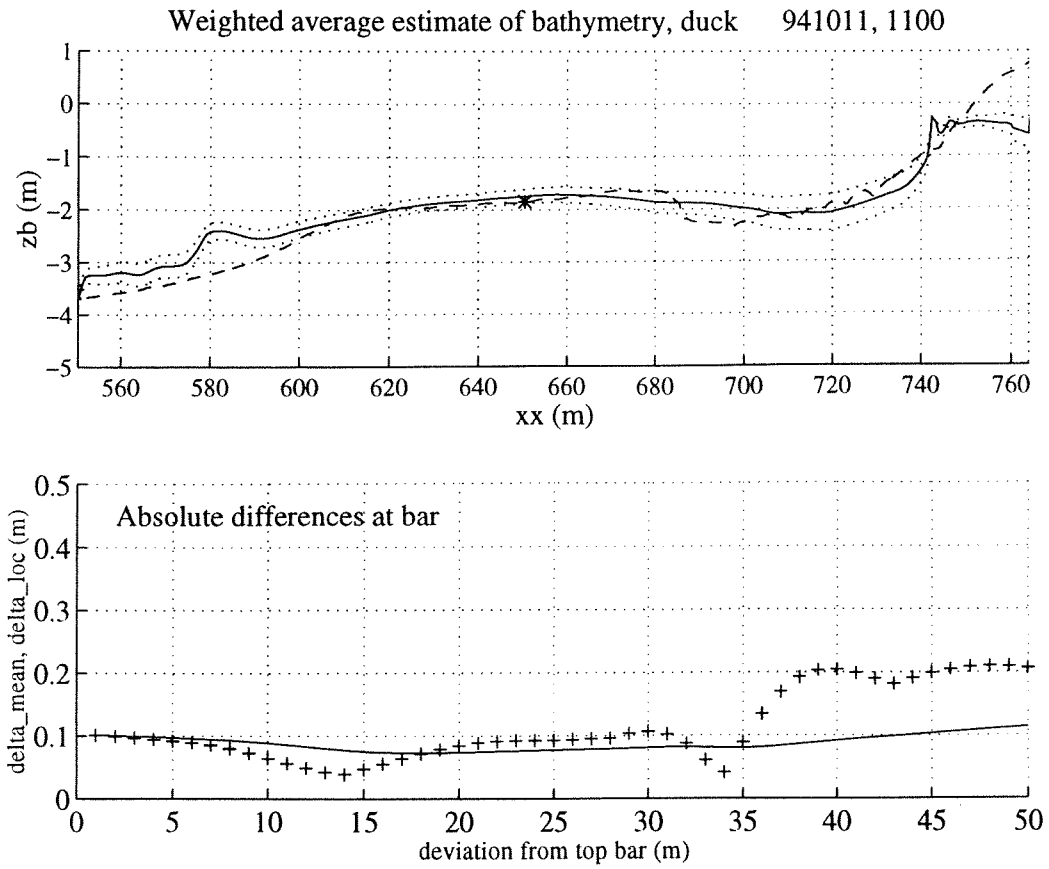

Figure F.6 Weighted estimate of bathymetry (for the meaning of second plot, see Appendix I)

Appendix G

Results stability & sensitivity analysis MONIMORPH

Results stability & sensitivity analysis MONIMORPH

This appendix graphically reports some results regarding the stability and sensitivity analysis as performed for the Duck bathymetry. The upper plot of each figure shows the surveyed bathymetry (dashed line and the computed bathymetry (solid line). All plots below show the absolute differences between both profiles (solid line), together with the band width of 95% confidence (dotted line). All results concern transect 1100 dd. 94/10/12, GMT 11:00.

The following cases are reported:

- Figure G.1 *Test on numerical stability*
  Deviations in case of a spatial step size Δxx of 0.06 m, 0.5 m and 8.0 m respectively
- Figure G.2 *Offset in rms wave height*
  Deviations in case of an offset $\Delta H_{rms}/H_{rms}$ of +5% and -5% respectively
- Figure G.3 *Offset in wave angle θ*
  Deviations in case of an offset $(\Delta\theta)/\theta_{bound}$ of +5% and -5% respectively
- Figure G.4 *Offset in wave period T_{sig}*
  Deviations in case of an offset $(\Delta T_{sig})/T_{sig}$ of +5% and -5% respectively
- Figure G.5 *Offset in water depth h*
  Deviations in case of an offset $(\Delta h)/h_{bound}$ of +5% and -5% respectively
- Figure G.6 *Effect of noise in the intensity signal*
  Deviations in case of a noise $2.81\Delta\cdot(E_r/c^2)/(E_r/c^2)$ of 10% and 15% respectively
- Figure G.7 *Effect of changing width of the camera field of view*
  Deviations in case of xx_{bound} at 500 m, 575 m and 625 m respectively

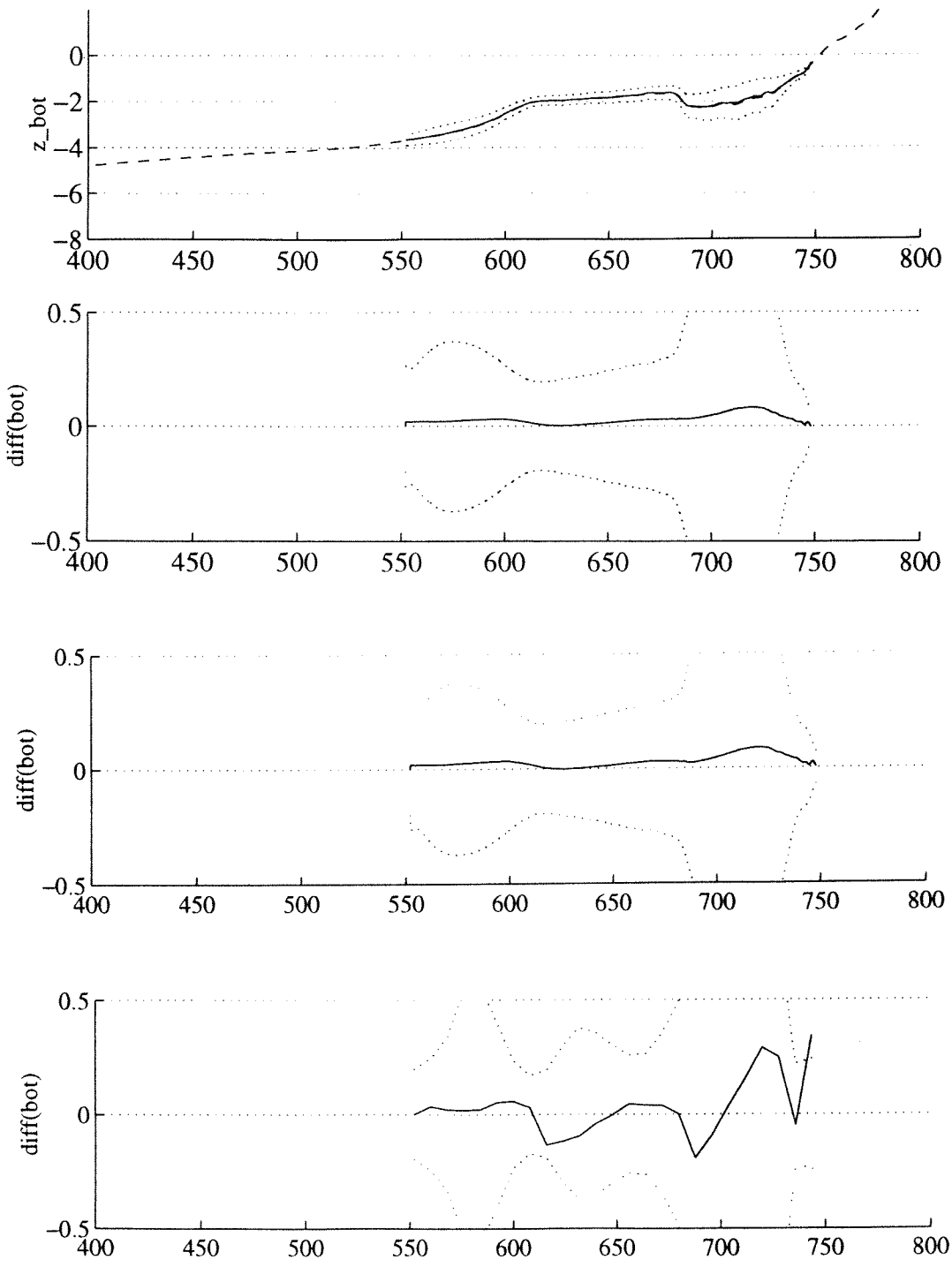

Figure G.1 Test on numerical stability

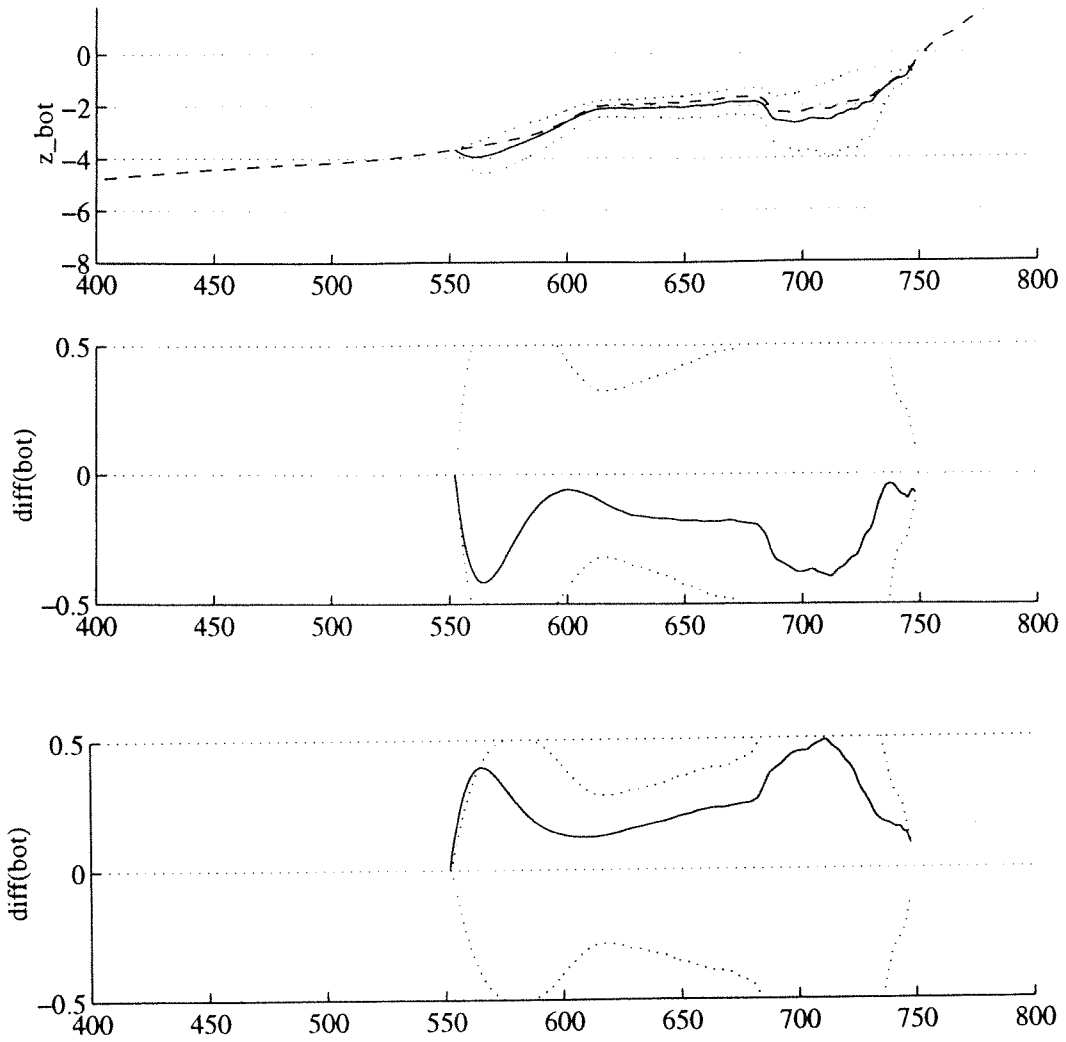

Figure G.2 Offset in rms wave height

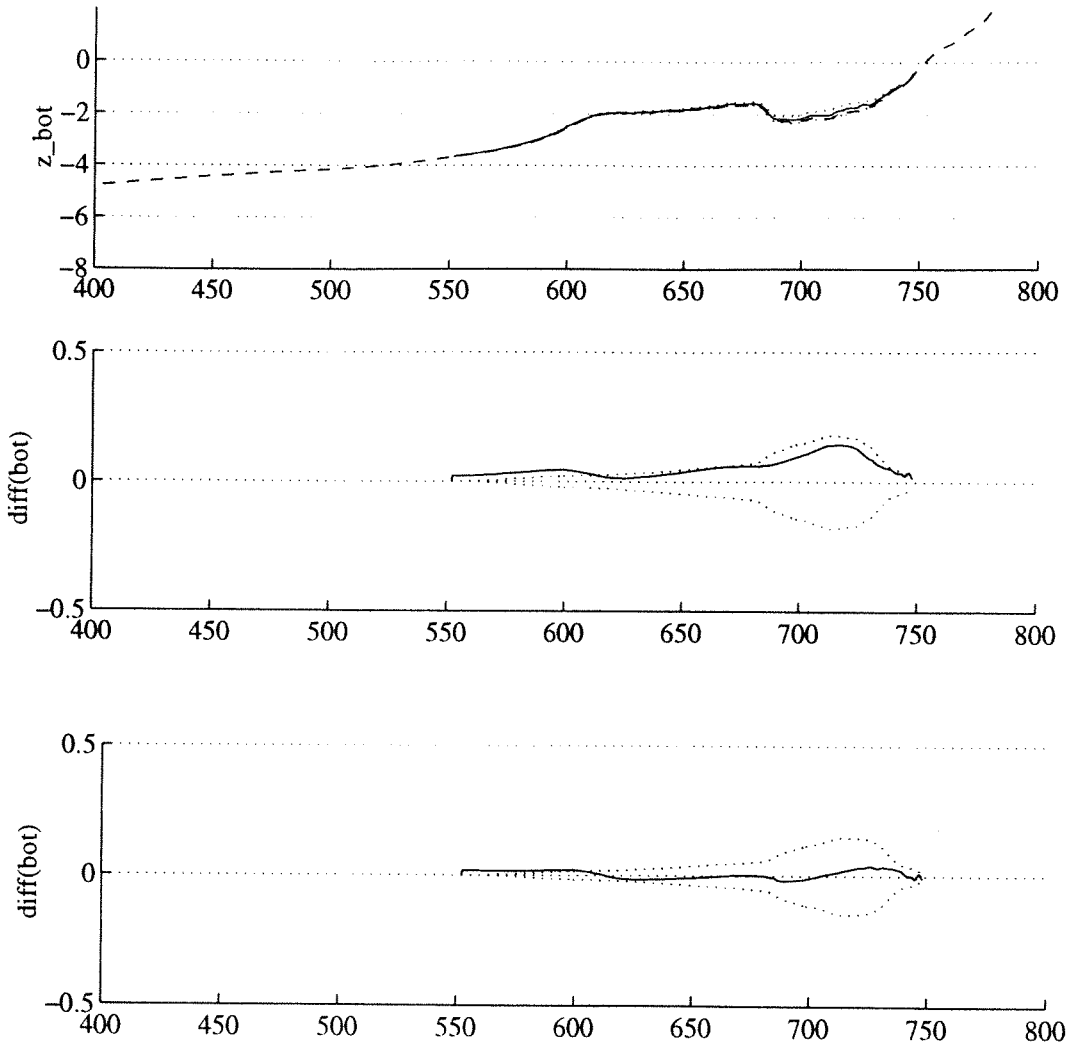

Figure G.3 Offset in wave angle θ

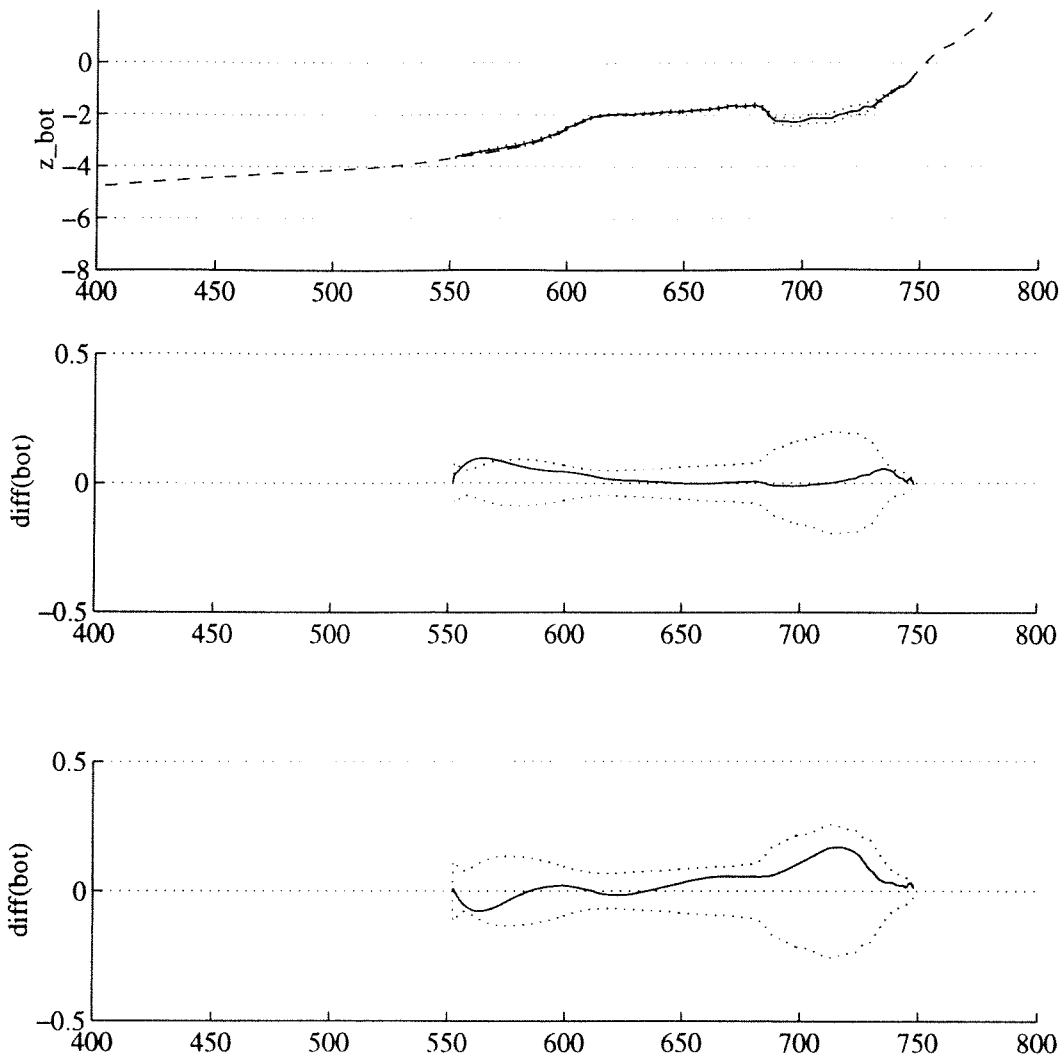

Figure G.4 Offset in wave period T_{sig}

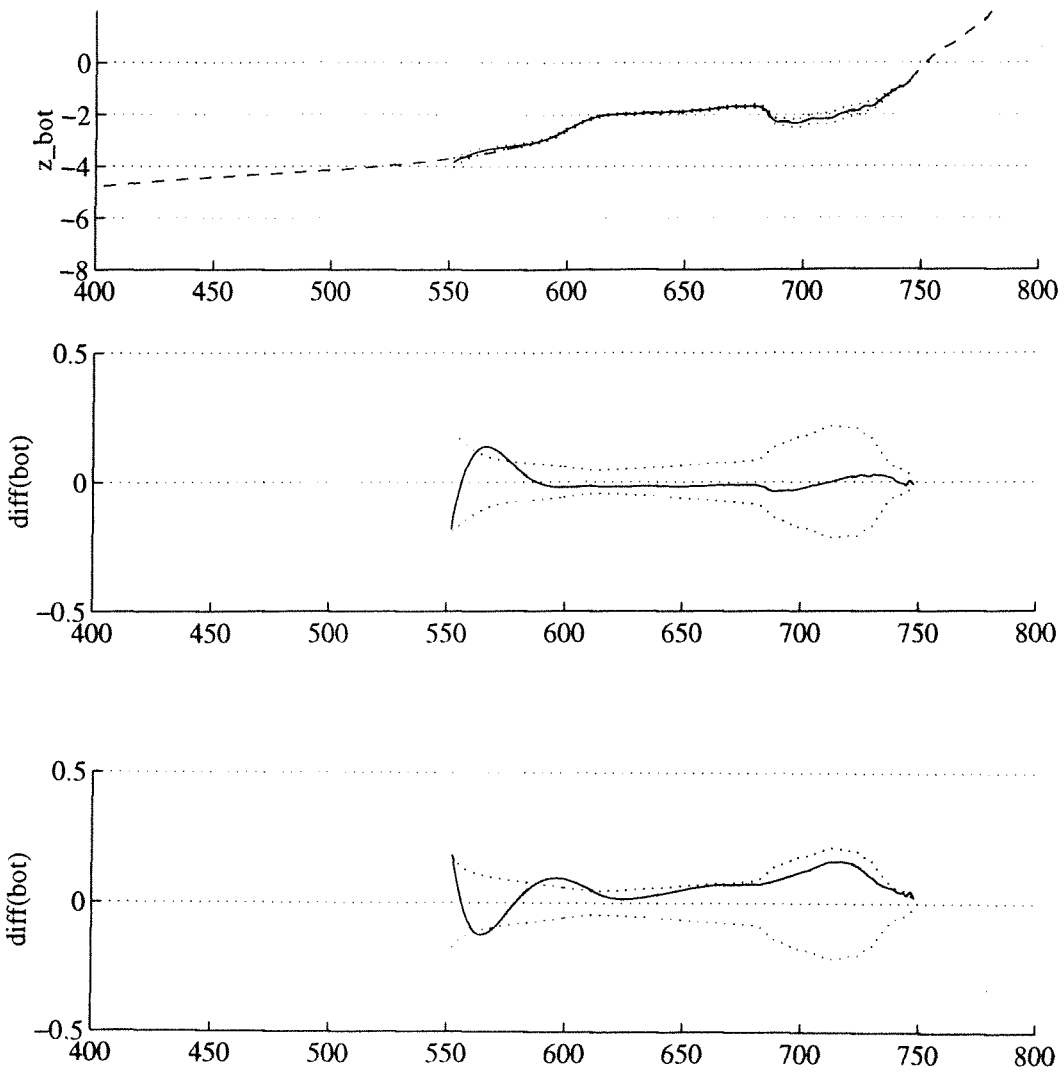

Figure G.5 Offset in water depth h

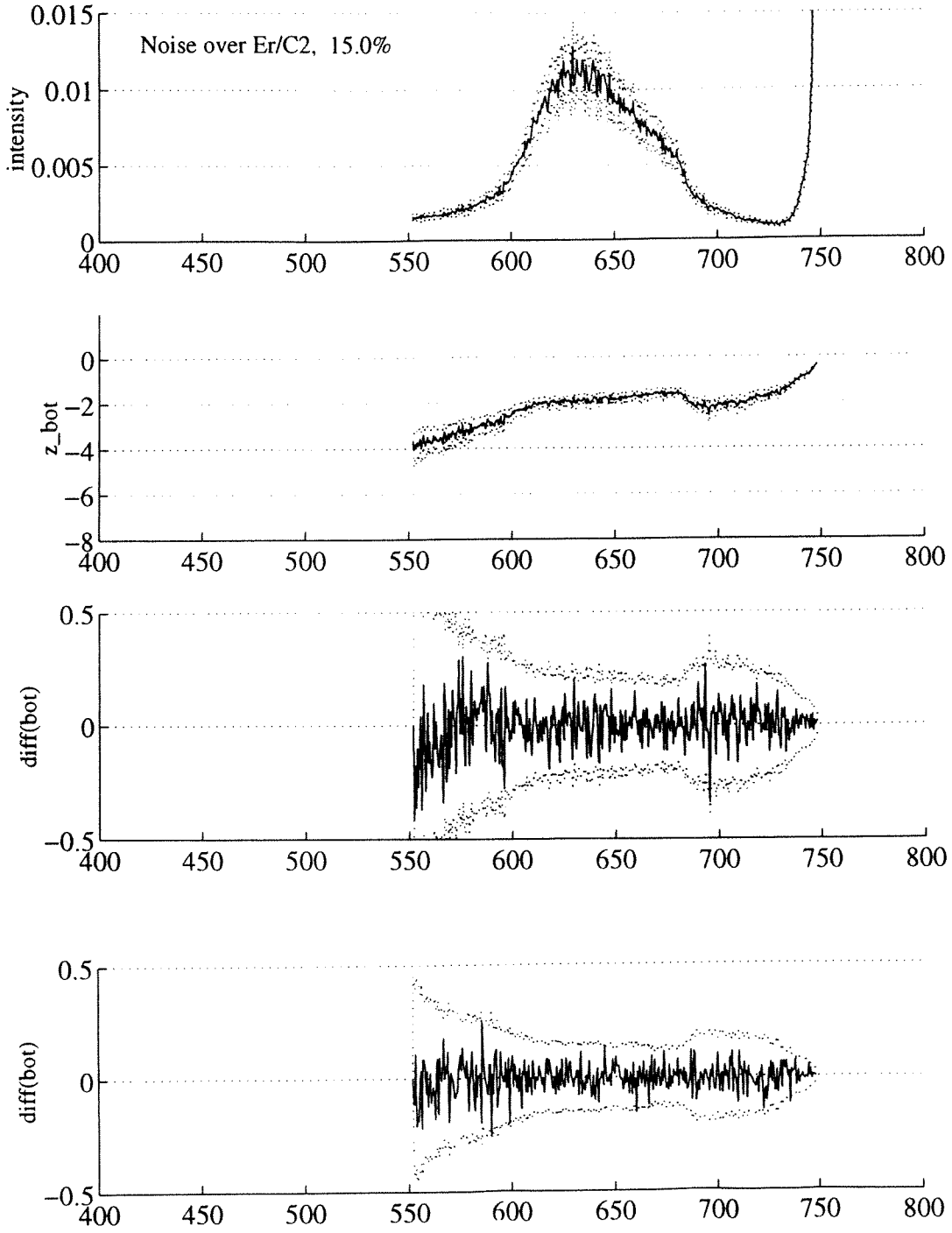

Figure G.6 Effect of noise in the intensity signal

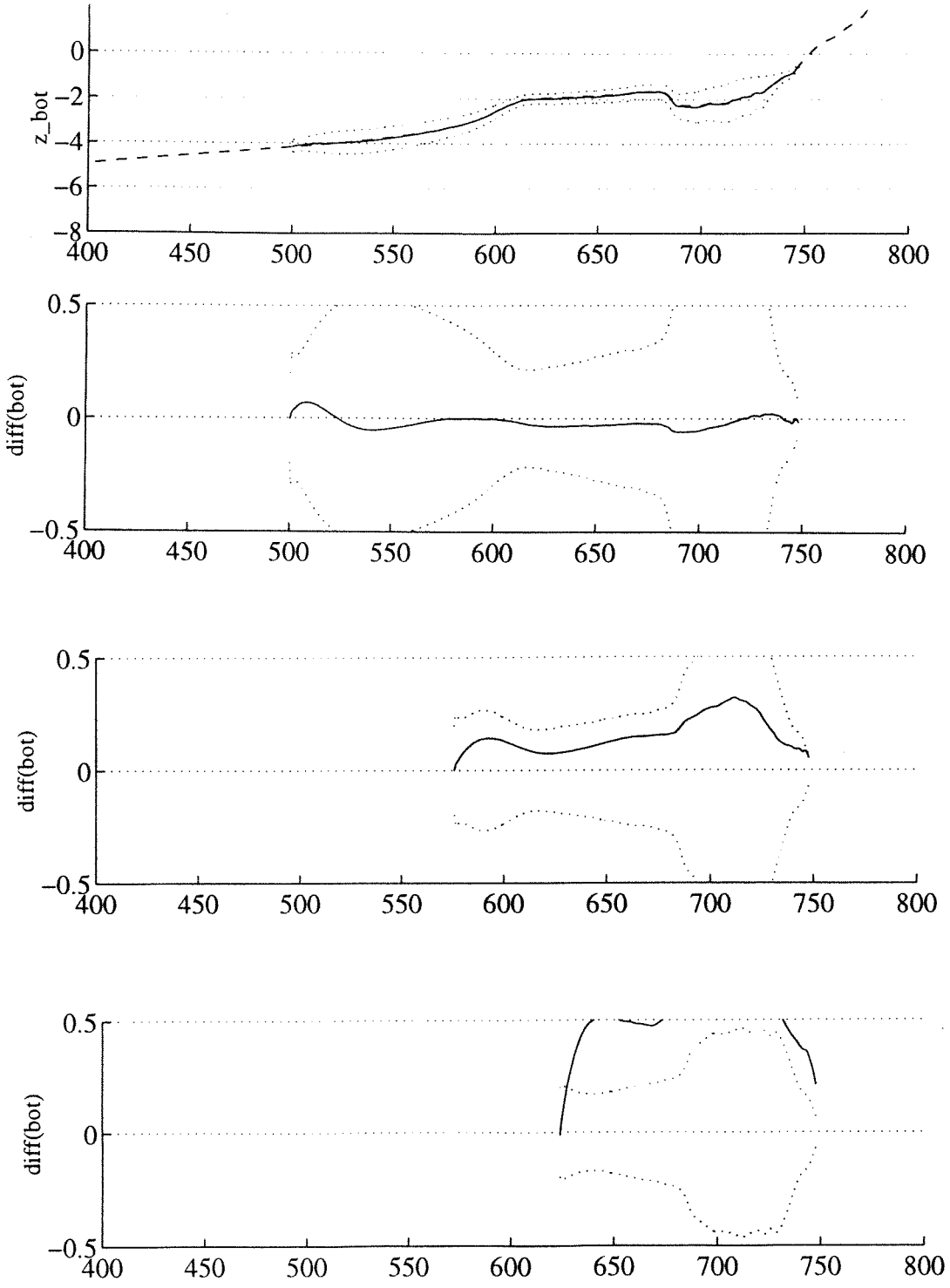

Figure G.7 Effect of changing width of the camera field of view

Appendix H

Figures related to the MONIMORPH scaling operation

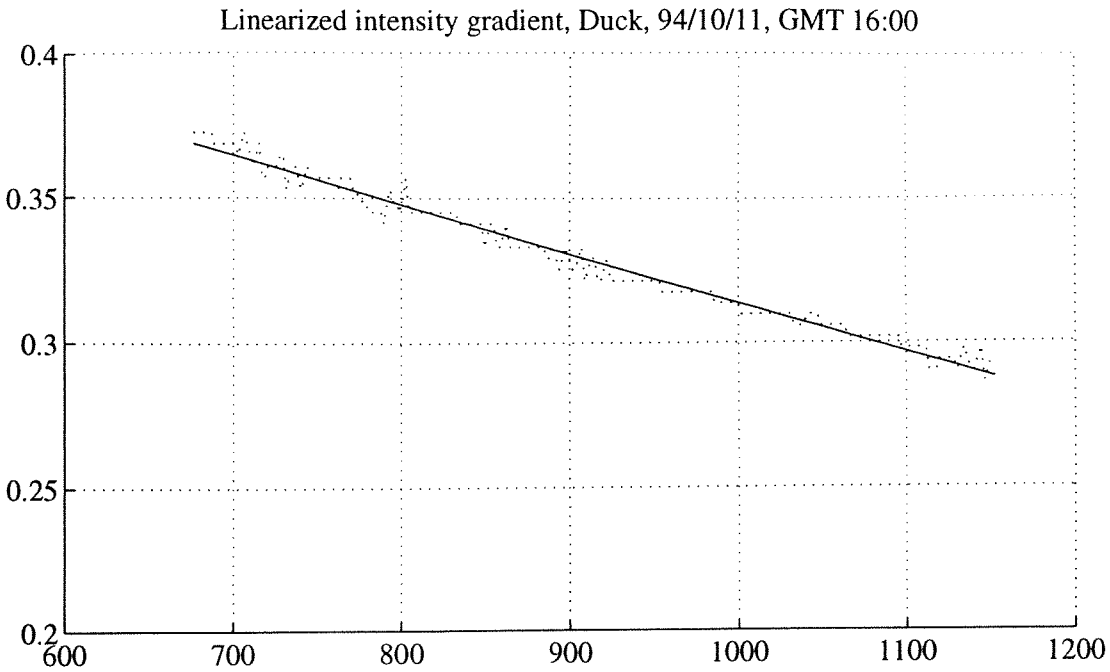

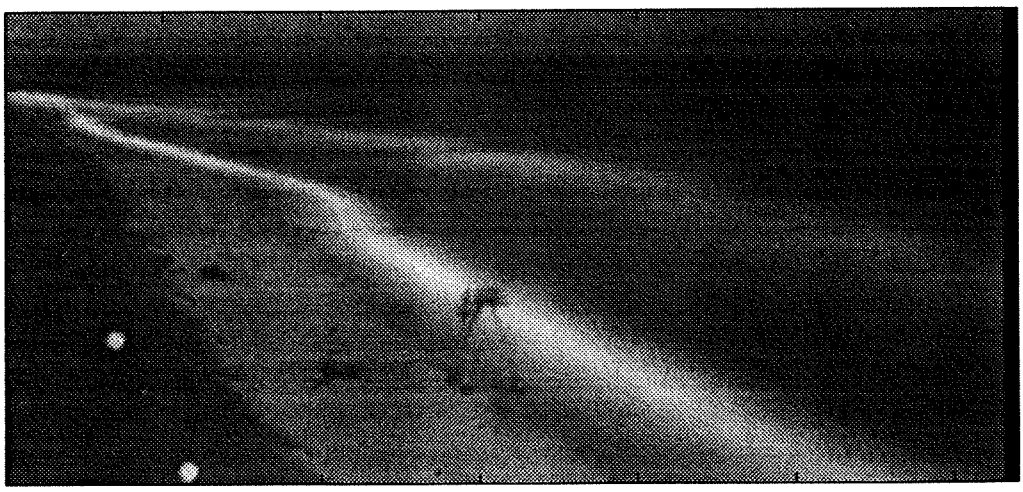

Figure H.1 Linear deep water intensity gradient, Duck

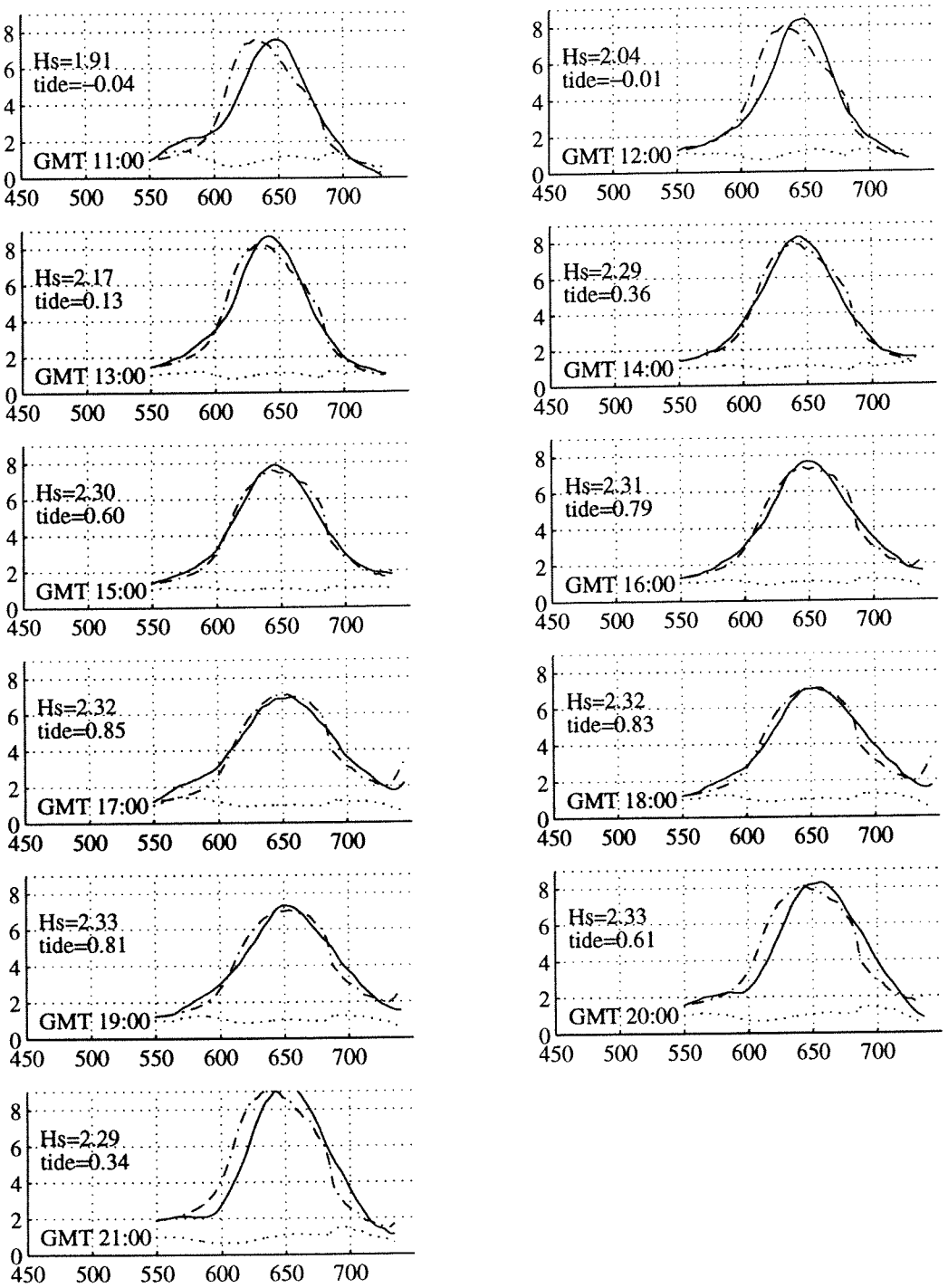

Figure H.2 Scaled intensities vs. E_f/c^2 profile, optimal scalefactors

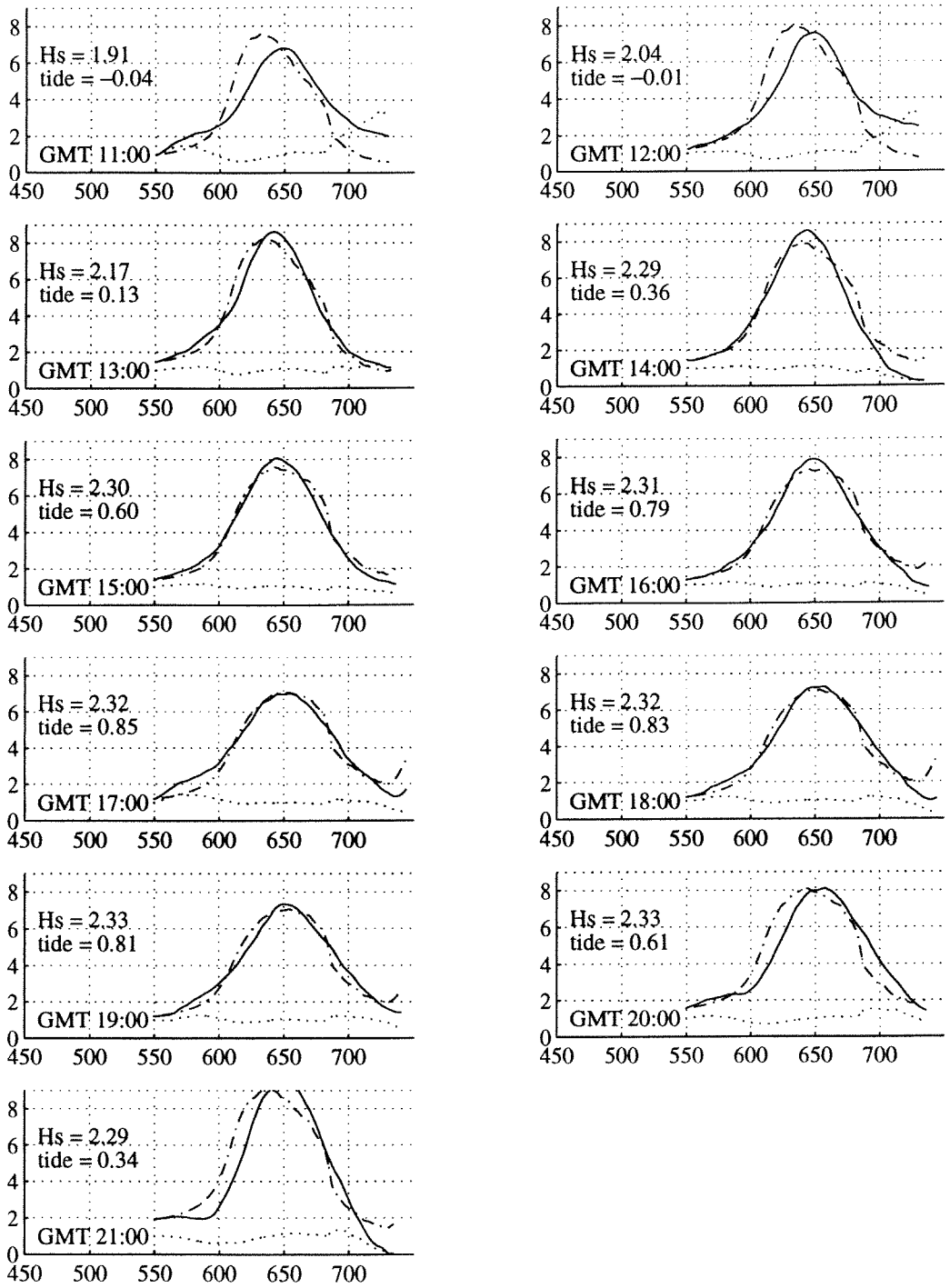

Figure H.3 Scaled intensities vs. E_t/c^2 profile, SF according to scaling relation (7.2)

Appendix I

Inverse estimates of the Duck bar bathymetry

Inverse estimates of the Duck bar bathymetry

This appendix gives some results, obtained from running MONIMORPH in case of Duck. The inversely computed bathymetry is represented by means of two plots. The upper one contains the calculated bottom (solid line) compared to the surveyed bathymetry. The asterisk indicates the surveyed top of the bar, except for a 'wavy' bar shape like transect 1100 where it points out the estimated middle of the bar, found by selecting the deepest point of the trough and point of equal height at the seaward face of the bar. The x-position in the middle of these two locations has been defined as the middle of such a waved bar.

The lower plot gives the absolute difference between computation and measurement, as a function of the offset from the top (or middle respectively) of the bar. The solid line represents the mean difference, while the crosses indicate the difference added by the two most outside points. For instance, the given values at a deviation of 30 m should be interpreted as the mean difference over the middle 60 m of the bar, as well as the absolute, mean value of the two local errors at distances of 30 m at each side of the top.

In the following, ten results are reported graphically, for different reasons. The specific characteristic of each of these is shortly indicated here.

- Figure I.1 *Transect 1100, 94/10/11*
  Reliable result; wave conditions match the calibration conditions
- Figure I.2 *Transect 1140, 94/10/11*
  Reliable result; wave conditions match the calibration conditions
- Figure I.3 *Transect 1100, 94/10/10*
  Incapability of MONIMORPH to follow sudden drop in trough
- Figure I.4 *Transect 1190, 94/10/12*
  Incapability of MONIMORPH to reproduce sharply peaked bar
- Figure I.5 *Transect 1230, 94/10/20*
  Significant underestimate of scalefactor
- Figure I.6 *Transect 1030, 94/10/11*
  Significant overestimate of scalefactor
- Figure I.7 *Transect 1100, 94/10/04*
  Without minimum wave height filter $H_{sig}/H_{max,bar} > 0.6$
- Figure I.8 *Transect 1100, 94/10/04*
  Including minimum wave height filter $H_{sig}/H_{max,bar} > 0.6$
- Figure I.9 *Transect 1230, 94/10/10*
  Without maximum wave height filter $H_{sig}/H_{max,bar} < 1.2$
- Figure I.10 *Transect 1230, 94/10/10*
  Including maximum wave height filter $H_{sig}/H_{max,bar} < 1.2$

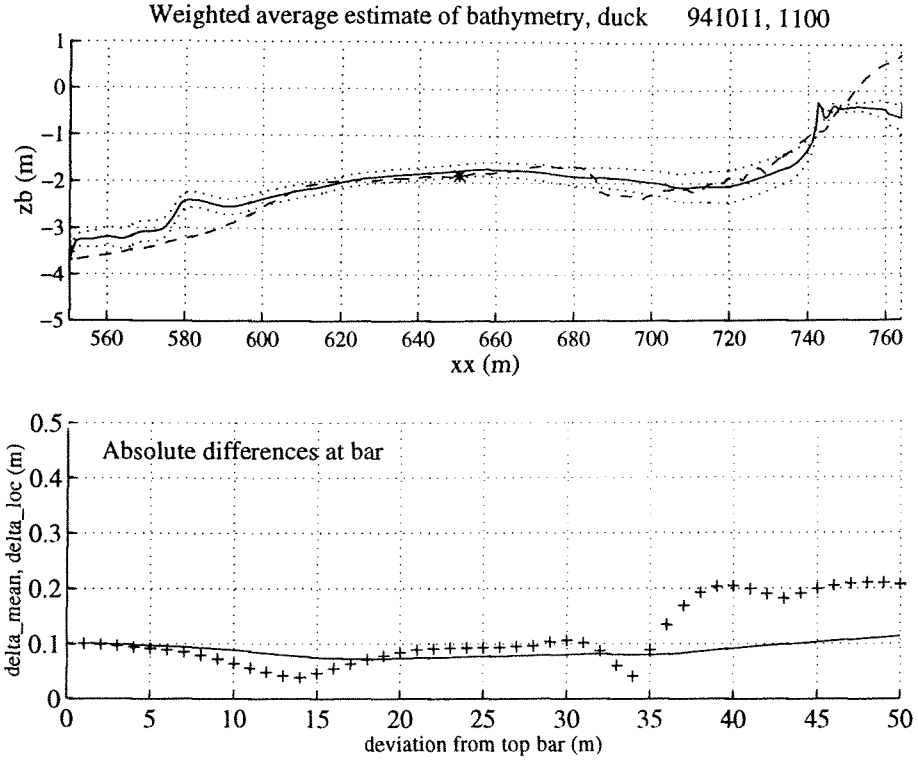

Figure I.1 Transcect 1100, 94/10/11

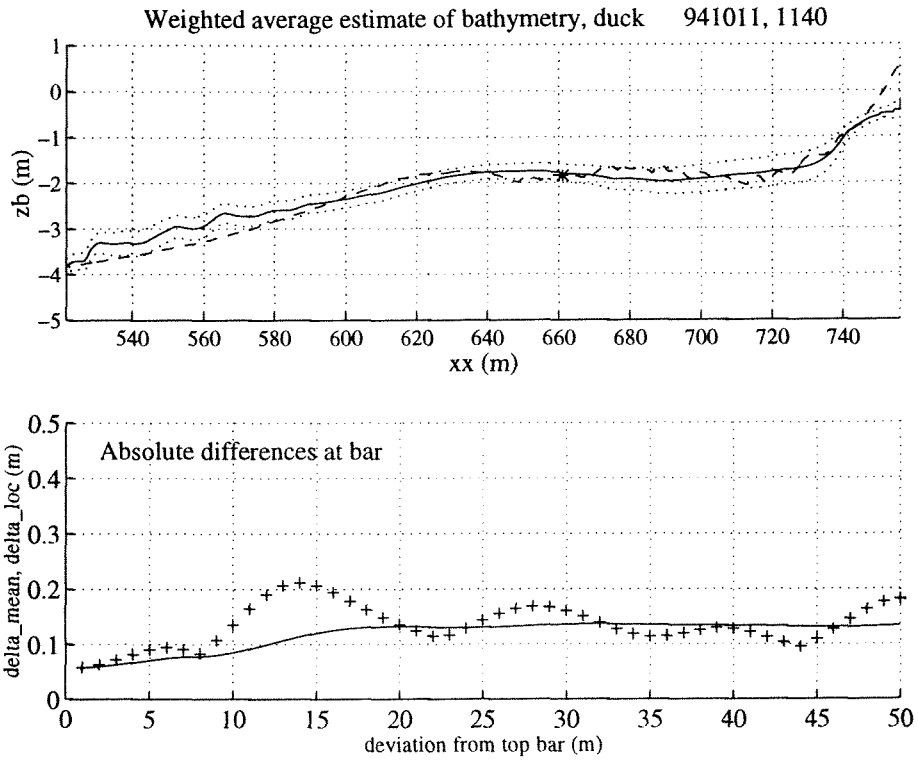

Figure I.2 Transcect 1140, 94/10/11

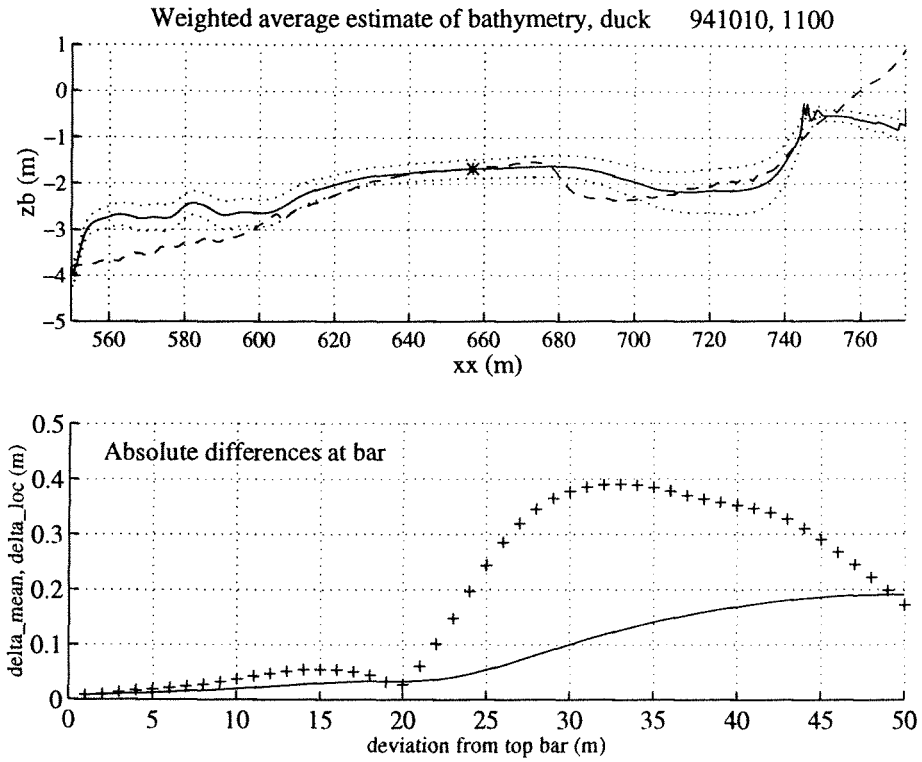

Figure I.3 Transcect 1100, 94/10/10

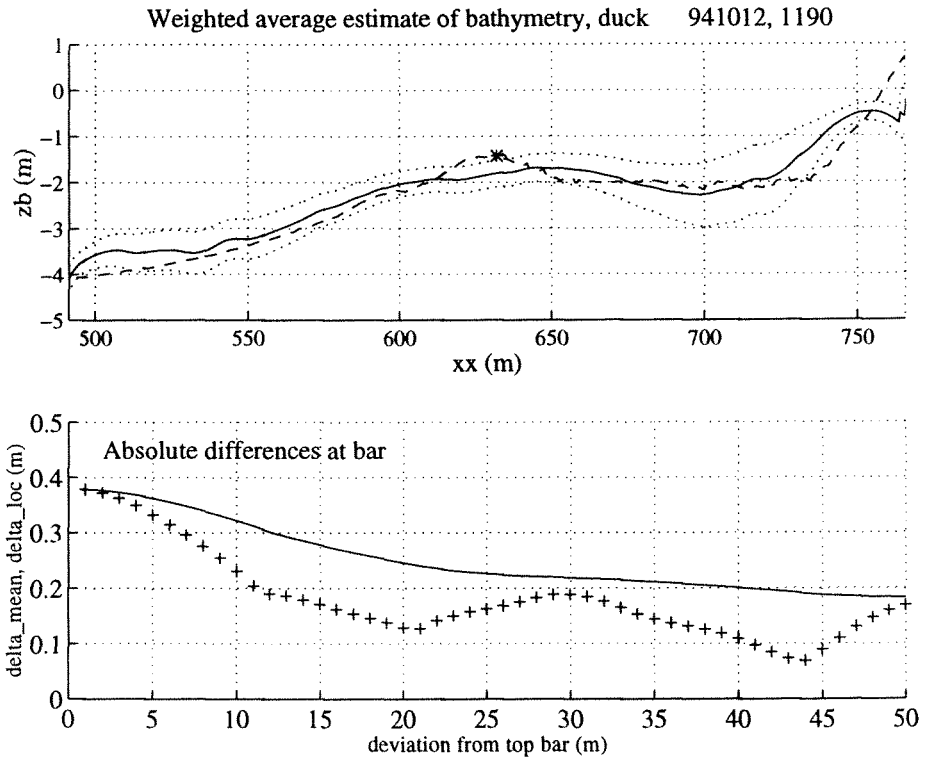

Figure I.4 Transcect 1190, 94/10/12

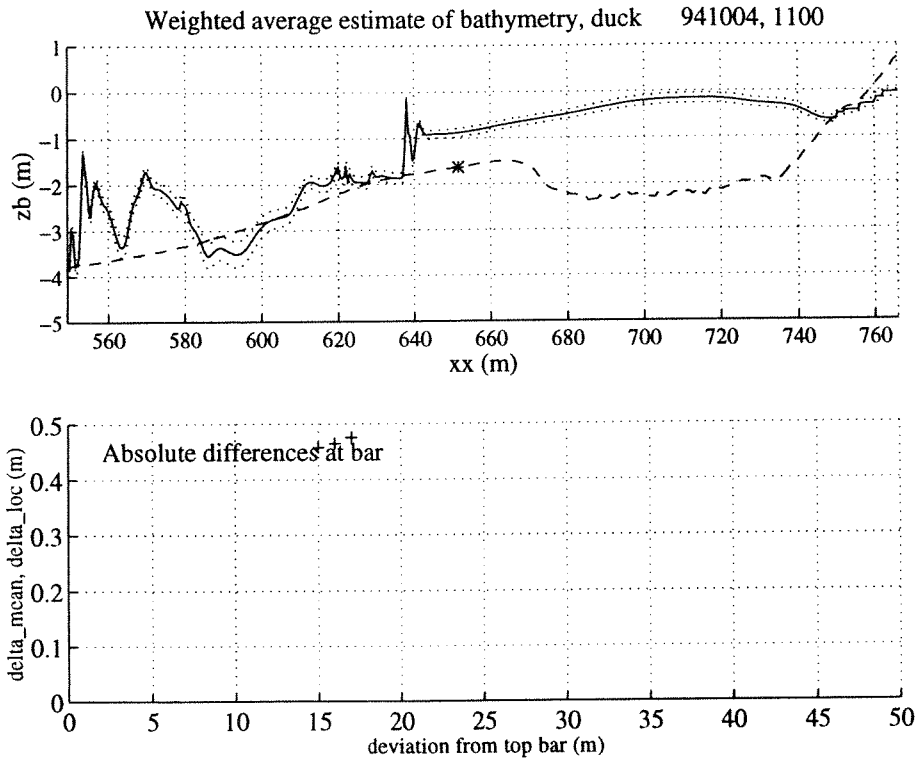

Figure I.7 Transcect 1100, 94/10/04

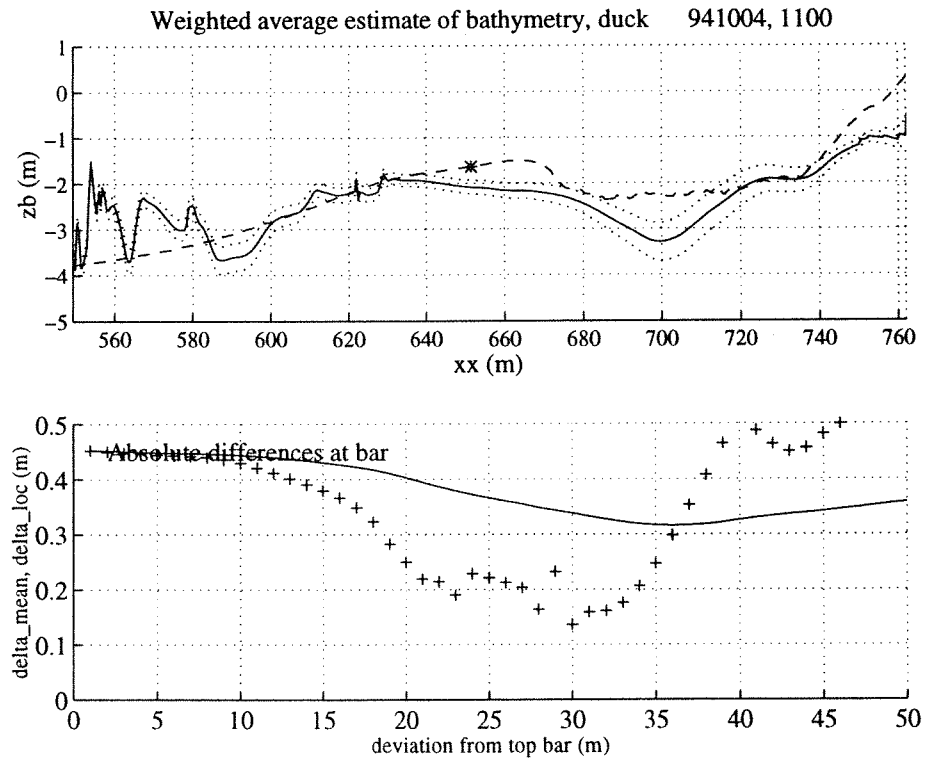

Figure I.8 Transcect 1100, 94/10/04

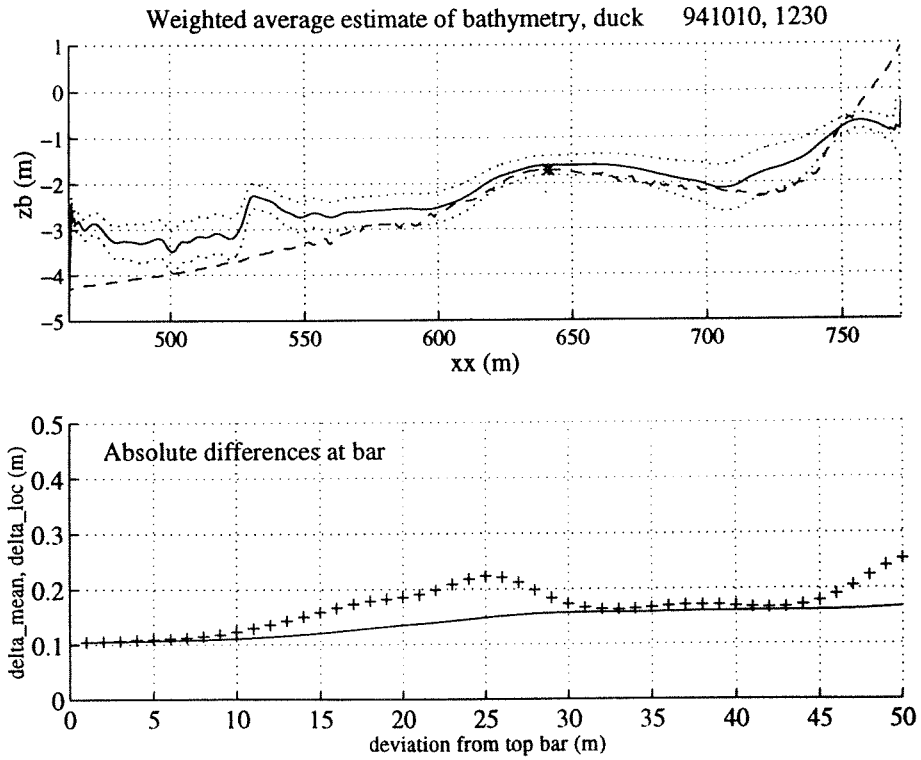

Figure I.9 Transcect 1230, 94/10/10

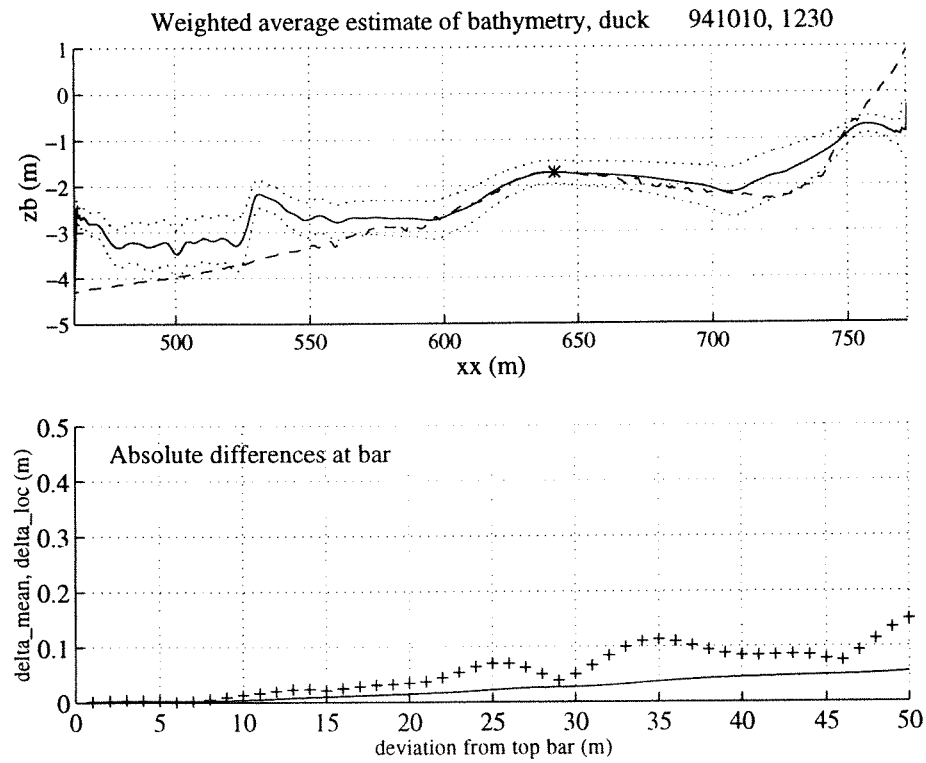

Figure I.10 Transcect 1230, 94/10/10

Appendix J

Inverse estimates of the Noordwijk bar bathymetry

Inverse estimates of the Noordwijk bar bathymetry

The figures below show the Noordwijk bathymetries as inversely computed dd. 95/09/28 (solid line). They are compared to waterleveled beach profiles dd. 95/09/30 (dashed line).

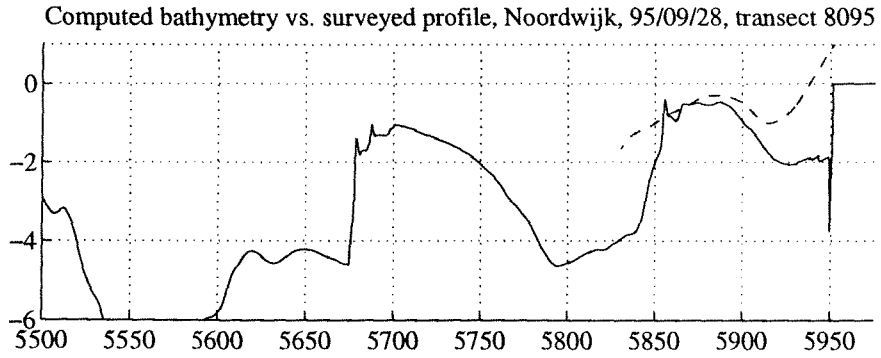

Figure J.1 Weighted estimate of bathymetry Noordwijk, 28/09/95, transect 8095

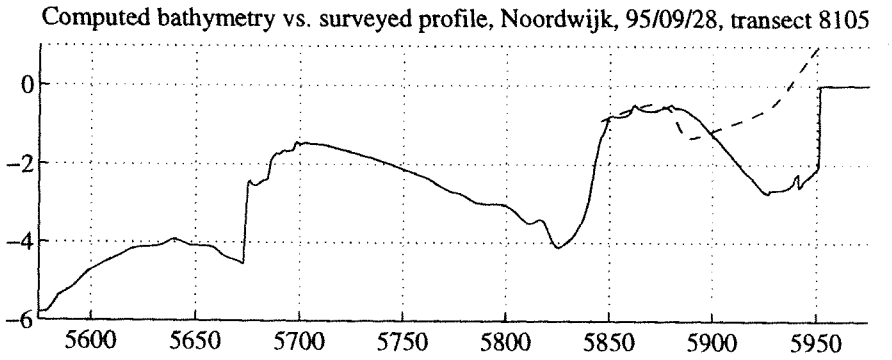

Figure J.2 Weighted estimate of bathymetry Noordwijk, 28/09/95, transect 8105

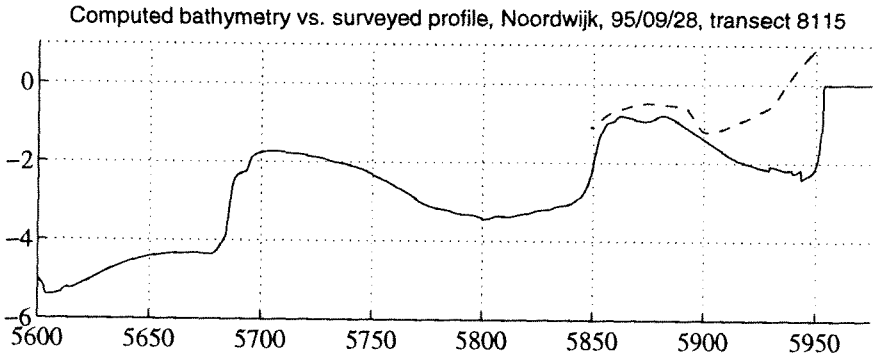

Figure J.3 Weighted estimate of bathymetry Noordwijk, 28/09/95, transect 8115